

Delft University of Technology

A Physics-Based Approach to Fatigue Life Prediction of Matrix-Dominated Fibre-Reinforced Composites

Rashmi Siriwardane Arachchilage

TU Delft

A Physics-Based Approach to Fatigue Life Prediction of Matrix-Dominated Fibre-Reinforced Composites

by

Rashmi Siriwardane Arachchilage

in partial fulfillment of the requirements for the degree of

Master of Science in Aerospace Engineering,

to be defended publicly on Monday September 28th, 2026 at 10:00 AM.

Student number:	5572959	
Project duration:	November 1, 2025 – September 28, 2026	
Thesis committee:	Prof. dr. ir. R.C. Alderliesten,	TU Delft, Responsible Supervisor
	Dr. ir. J.A. (John-Alan) Pascoe,	TU Delft, Chair
	Prof. dr. ir. R. Benedictus,	TU Delft, External Examiner

Cover:	Side View of a Failed ±45° GFRP/Epoxy Composite Gauge Section (Enhanced with AI)
Style:	TU Delft Report Style, with modifications by Rashmi Siriwardane

An electronic version of this thesis is available at http://repository.tudelft.nl/.

Preface

This thesis was completed as part of my MSc Degree in Aerospace Engineering within the department of Aerospace Structures and Materials. It marks the end of a five-year journey in Delft, from the beginning of my Bachelor's degree to the completion of my Master's degree. These five years have been among the most defining and memorable years of my life, both academically and socially, and I am deeply grateful to everyone who supported me and shared this journey with me.

First and foremost, I would like to express my sincere gratitude to my supervisor, Professor René Alderliesten. From the DSE days onward, his guidance, big-picture perspective and ability to look beyond the immediate problem have had a lasting influence on me. I have always appreciated not only his technical insight, but also his sense of humour with which he often conveyed a deeper message. He has been a significant role model throughout my studies, particularly within the field of fatigue, and having had the opportunity to complete this thesis under his supervision has been a great honor for me.

I would also like to thank Sofia, Julia, Ioana and the DASML laboratory staff for their patience, support and willingness to help throughout the experimental work. Their assistance during both specimen manufacturing and testing was invaluable, particularly when my own laboratory skills were still very much a work in progress. I am very grateful for the time, practical knowledge and encouragement they provided throughout the project.

I would also like to express my deep gratitude to Professor Calvin Rans. Having had the opportunity to work with him as a teaching assistant across several courses gave me the chance to learn from someone I greatly respect, both professionally and personally. His approach to teaching, mentorship and academic work strongly influenced my own interest in education and made a lasting impression on me. He has also been an important role model during my time at TU Delft.

To my friends, you have been the best part of my five years. Thank you for the countless late nights in the library, and for making five demanding years somehow pass far too quickly.

Finally, I would like to thank my brother and my parents for their constant support, patience, and encouragement throughout my studies. Their belief in me has been a continuous source of motivation that I will always need by my side.

Thank you!

Rashmi Siriwardane Arachchilage
Delft, September 2026

Abstract

Fatigue-life characterization of fibre-reinforced polymer composites traditionally relies on extensive constant-amplitude testing to establish empirical S-N curves, with separate test campaigns often required for different stress ratios and loading conditions. Physics-based approaches offer the possibility of reducing this experimental burden; however, frameworks developed for fibre-dominated laminates rely on assumptions that become questionable for matrix-dominated configurations where concepts such as creep, ratcheting, fibre re-orientation and nonlinear viscoelastic behaviour are non-negligible. In light of this, the thesis sought to answer the following main research question:

To what extent do $\pm 45^\circ$ *composite laminates conform to Krieg's modified linear viscoelastic fatigue prediction framework, and how can previously overlooked matrix-dominated behaviors be used to justify the framework's deviation, and be leveraged to extend it?*

An experimental campaign comprising monotonic tensile, constant-amplitude fatigue, stress-sweep, creep-recovery and dynamic mechanical analysis (DMA) was conducted with fatigue tests covering stress ratios of R = 0.1, 0.3, 0.5 and 0.7. The resulting data were used as input and validation data for the proposed framework developed to extend Krieg's model.

Analyzing cyclic stress-strain behaviour showed a pronounced initial transient associated with fibre re-orientation, followed by a comparatively stable response in stiffness, mean strain and energy damping ratio metrics. A nonlinear viscoelastic augmentation parameter, Ψ, derived from Schapery-based creep-recovery characterization, was incorporated into Krieg's fatigue-life prediction formulation. The original framework produced root-mean-square prediction errors of 0.656, 0.710 and 0.845 decades for stress ratios R = 0.3, 0.5, and 0.7, respectively, while the inclusion of the new augmentation parameter reduced these errors to 0.316, 0.134 and 0.269 decades.

Additionally, stress-sweep test results combined with Miner's rule showed potential for estimating the S-N curve slope without a conventional reference fatigue dataset, yielding prediction errors of 0.629 and 0.494 decades for R = 0.1 and 0.3, respectively. The DMA loss-factor intersection yielded an estimated fatigue limit of 71.5 MPa, while stress-sweep testing yielded estimates of 69.2 MPa and 77.0 MPa at $R = 0.1$ and $R = 0.3$, respectively. Fatigue-equivalent monotonic tensile testing resulted in a 4.4–18.8% increase in ultimate tensile strength compared with quasi-static loading, supporting its use as a physically representative estimate of the $R = 0$ upper anchor of the S–N curve.

Overall, the results provide a proof of concept that the fundamental energy-based principles of Krieg's framework can be extended to matrix-dominated composites, while indicating that further characterization of viscoplasticity and damage is required for a more complete physics-based formulation.

Contents

Preface i

Abstract ii

List of Symbols v

List of Abbreviations vii

List of Figures viii

List of Tables xi

1 Introduction 1

2 Literature Review 2
- 2.1 Theoretical Background . . . 2
- 2.2 The Modified Linear Viscoelastic Framework . . . 4
  - 2.2.1 Framework . . . 4
  - 2.2.2 Main Findings . . . 6
- 2.3 The challenge of Matrix-Dominated Composites . . . 12
  - 2.3.1 Nature of ±45° Laminates . . . 12
  - 2.3.2 Breakdown of Assumptions . . . 29
- 2.4 Fatigue Life Prediction . . . 31
  - 2.4.1 Overview . . . 31
  - 2.4.2 Research Gaps and Questions . . . 31

3 The Proposed Framework 36
- 3.1 Nonlinear Viscoelastic Extension of Krieg's Fatigue-Life framework . . . 36
- 3.2 Identification of Model Parameters . . . 39
  - 3.2.1 Model Parameters for the Slope Constituent (Implementation of Ψ Augmentation) . . . 39
  - 3.2.2 Model Parameters for the Slope Constituent (Implementation of SST Miner's Rule) . . . 42
  - 3.2.3 Model Parameters for the Upper and Bottom Anchor . . . 43
- 3.3 Schematic Overview of the Proposed Framework . . . 43

4 Experimental Methodology 45
- 4.1 Experimental Design . . . 45
  - 4.1.1 Chosen Material and Lay-up . . . 45
  - 4.1.2 Specimen Design . . . 45
  - 4.1.3 Loading Strategy . . . 49
- 4.2 Specimen Manufacturing and Preparation . . . 53
  - 4.2.1 Manufacturing Process . . . 53
  - 4.2.2 Specimen Quality . . . 55
  - 4.2.3 Overview of Final Specimens . . . 56
- 4.3 Experimental Procedures and Equipment . . . 57
  - 4.3.1 Monotonic Tensile Testing . . . 57
  - 4.3.2 Stress-Sweep Testing . . . 58
  - 4.3.3 Constant Amplitude Fatigue Testing . . . 58
  - 4.3.4 Creep and Recovery Testing . . . 60
  - 4.3.5 Dynamic Mechanical Analysis . . . 62

5 Results, Discussion and Limitations 63
- 5.1 General Observed Behavior . . . 63
  - 5.1.1 Monotonic Tensile Test Results . . . 63
  - 5.1.2 Overview of General Fatigue Performance . . . 64
  - 5.1.3 Stiffness Evolution . . . 66
  - 5.1.4 Strain Progression . . . 68
  - 5.1.5 Hysteresis Dissipated Energy . . . 69
  - 5.1.6 Applied Energy . . . 70
  - 5.1.7 Loss Factor . . . 70
  - 5.1.8 Answers to Research Question-01 . . . 72

5.2 Fatigue Life Prediction and Validation . . . 72
5.2.1 Creep-Recovery Analysis, and the Augmentation Parameter Ψ . . . 72
5.2.2 Answers to Research Question-02 . . . 73
5.2.3 Stress-Sweep TDE-TW Ratio, and Implementation of Miner's Rule . . . 75
5.2.4 Answers to Research Question-03 . . . 75
5.3 Fatigue Limit Determination using DMA and SST . . . 77
5.3.1 DMA Test Results, and HCFS Determination . . . 77
5.3.2 Bilinear Regression on Stress-Sweep TDE-TW Ratio . . . 78
5.3.3 Answers to Research Question-04/05 . . . 78
5.4 Rate-Dependent UTS and S-N curve Applicability . . . 79
5.4.1 Answers to Research Question-06 . . . 79
5.5 Towards a Unified Fatigue-Life Prediction Approach . . . 80
5.6 Limitations . . . 80

6 Conclusion 83
6.1 Summary . . . 83
6.2 Concluding Remarks . . . 83
6.3 Recommendations . . . 84

References 88

A MTS MPT Programming Sequences 89
A.1 Programming Sequences for $R = 0.1$ . . . 89
A.1.1 50% UTS, $R = 0.1$ . . . 89
A.1.2 60% UTS, $R = 0.1$ . . . 89
A.1.3 62% UTS, $R = 0.1$ . . . 89
A.1.4 65% UTS, $R = 0.1$ . . . 90
A.2 Programming Sequences for $R = 0.3$ . . . 90
A.2.1 60% UTS, $R = 0.3$ . . . 90
A.2.2 65% UTS, $R = 0.3$ . . . 90
A.2.3 70% UTS, $R = 0.3$ . . . 91

B Recommended Procedure for Applying and Extending the Proposed Framework 92

List of Symbols

$A(0)$	Initial linear elastic compliance	$[\mathrm{Pa}^{-1}]$	$\Delta A(\psi)$	Transient linear viscoelastic compliance	$[\mathrm{Pa}^{-1}]$
a_σ	Stress-dependent time-scale factor	$[-]$	C	Transient creep-compliance power-law coefficient	$[\mathrm{Pa}^{-1}\,\mathrm{s}^{-\mathrm{n}}]$
D	Cumulative fatigue-damage parameter in Miner's rule	$[-]$	E	Elastic or dynamic modulus	[Pa]
E_0	Initial or reference stiffness	[Pa]	$\frac{E}{E_0}$	Normalized stiffness	$[-]$
E_{avg}	Average stiffness or modulus	[Pa]	E'	Storage modulus	[Pa]
E''	Loss modulus	[Pa]	E^*	Complex dynamic modulus	[Pa]
$\lvert E^*\rvert$	Magnitude of the complex dynamic modulus	[Pa]	f	Loading frequency	[Hz]
$f_{\max}$	Maximum allowable loading frequency	[Hz]	g_0	Nonlinear stress-dependent instantaneous-compliance parameter	$[-]$
g_1	Nonlinear stress-dependent Schapery parameter	$[-]$	g_2	Nonlinear stress-dependent Schapery parameter	$[-]$
i	Cycle or stress-block index	$[-]$	K	Creep-curve power-law fitting coefficient	$[-]$
K'	Creep-curve power-law fitting coefficient	$[-]$	L	Effective clamp-to-clamp specimen length	[m]
n	Creep-compliance power-law exponent	$[-]$	n_i	Number of cycles applied at stress level i	$[-]$
N_i	Number of cycles to failure at stress level i	$[-]$	N_f	Number of cycles to fatigue failure	$[-]$
$\frac{N}{N_f}$	Normalized fatigue life	$[-]$	R	Stress ratio	$[-]$
R_1	Reference stress ratio	$[-]$	R_2	Target or predicted stress ratio	$[-]$
S_{11}	Normal stress in the local fibre direction	[Pa]	S_{12}	In-plane shear stress in the local material coordinate system	[Pa]
T	Temperature	[°C]	T_g	Glass-transition temperature	[°C]
t	Time	[s]	t_1	Duration of the preceding creep hold	[s]
$v_{\max}$	Maximum actuator or crosshead velocity	[m/s]	W_a	Applied work per cycle	$[\mathrm{J/m^3}]$
W_{cycle}	Energy enclosed by a stress–strain hysteresis cycle	$[\mathrm{J/m^3}]$	W_{cyclic}	Cyclic contribution to total dissipated energy	$[\mathrm{J/m^3}]$
W_{creep}	Creep contribution to total dissipated energy	$[\mathrm{J/m^3}]$	W_{diss}	Experimentally determined dissipated energy per cycle	$[\mathrm{J/m^3}]$
W_h	Cyclic hysteresis dissipated energy per cycle	$[\mathrm{J/m^3}]$	W_{total}	Total dissipated energy	$[\mathrm{J/m^3}]$
w_{gauge}	Gauge-section width	[m]	w_{tab}	Tab or specimen width	[m]
ΔW	Energy dissipated during one loading cycle	$[\mathrm{J/m^3}]$	ΔW_{in}	Applied or input strain-energy increment	$[\mathrm{J/m^3}]$

$\Delta W_{\text{elastic}}$	Elastic component of input energy	[J/m^3]	$\Delta W_{\text{inelastic}}$	Inelastic component of input energy	[J/m^3]
δ	Phase angle in dynamic mechanical analysis	[deg]	$\dot{\delta}$	Crosshead displacement rate	[m/s]
$\varepsilon(t)$	Time-dependent strain	[−]	ε_a	Strain amplitude	[−]
ε_m	Mean cyclic strain	[−]	$\varepsilon_{\max}$	Maximum strain in a loading cycle	[−]
$\varepsilon_{\min}$	Minimum strain in a loading cycle	[−]	$\varepsilon_{\text{fail}}$	Strain at failure	[−]
ε_c	Creep strain	[−]	ε_r	Recovery strain	[−]
$\dot{\varepsilon}$	Strain rate	[s^{-1}]	$\dot{\varepsilon}_{\max}$	Maximum strain rate	[s^{-1}]
$\dot{\varepsilon}_{\text{target}}$	Prescribed target strain rate	[s^{-1}]	ε_{xx}	Normal strain in the x-direction	[−]
ε_{yy}	Normal strain in the y-direction	[−]	ϕ	Stress–strain phase angle	[deg]
$\sin(\phi)$	Viscoelastic loss factor	[−]	$\sin(\phi_{\text{eff}})$	Effective fatigue-life loss factor	[−]
λ	Reduced recovery-time coordinate	[s]	$\sigma(t)$	Time-dependent applied stress	[Pa]
σ_a	Stress amplitude	[Pa]	σ_m	Mean cyclic stress	[Pa]
$\sigma_{\max}$	Maximum cyclic stress	[Pa]	$\sigma_{\min}$	Minimum cyclic stress	[Pa]
$\bar{\sigma}$	Effective stress accounting for damage	[Pa]	τ	Integration or past-time variable	[s]
θ_0	Initial fibre orientation angle	[deg]	θ_f	Re-oriented fibre angle	[deg]
ω	Angular loading frequency	[rad/s]	ψ	Reduced time in the Schapery formulation	[s]
ψ'	Reduced time corresponding to the integration variable τ	[s]	Ψ	Nonlinear viscoelastic augmentation parameter	[−]

List of Abbreviations

$3PB$	Three-Point Bending	[–]	CA	Constant Amplitude	[–]
CDE	Critical Dissipated Energy	[–]	$CFRP$	Carbon-Fibre-Reinforced Polymer	[–]
$CLPT$	Classical Laminate Plate Theory	[–]	DMA	Dynamic Mechanical Analysis	[–]
$DMTA$	Dynamic Mechanical Thermal Analysis	[–]	DT	Destructive Testing	[–]
FE	Fatigue-Equivalent	[–]	$GFRP$	Glass-Fibre-Reinforced Polymer	[–]
HCF	High-Cycle Fatigue	[–]	$HCFS$	High-Cycle Fatigue Strength	[–]
MAT	Multiple Amplitude Test	[–]	MPT	Multi-Purpose Testware	[–]
MT	Monotonic Tensile	[–]	NDT	Non-Destructive Testing	[–]
QS	Quasi-Static	[–]	$RMSE$	Root-Mean-Square Error	[–]
$S-N$	Stress-Life Curve	[–]	$S-VECD$	Simplified Viscoelastic Continuum Damage	[–]
SST	Stress-Sweep Testing	[–]	TDE	Total Dissipated Energy	[–]
TTS	Time-Temperature Superposition	[–]	$TTSP$	Time-Temperature Superposition	[–]
TW	Total Work	[–]	UD	Unidirectional	[–]
UTS	Ultimate Tensile Strength	[–]			

List of Figures

2.1 Hysteresis Loop [9] . . . 2
2.2 Normalized strain energy density as a function of fatigue life for different off-axis fibre orientations, illustrating the collapse of the experimental data onto a common master curve [15] . . . 3
2.3 Visual Representation of decoupling hysteresis and creep, illustrating the assumed model (B) compared to reality (A) [1] . . . 4
2.4 Modified Viscoelastic Loss factor vs. Normalized fatigue life for $[0/90]_{4s}$ UD E-glass/BT080-epoxy laminate [1] . . . 6
2.5 Effective Loss factor vs. Maximum gauge stress for $[0/90]_{4s}$ UD E-glass/BT080-epoxy laminate [1] 7
2.6 Modified Viscoelastic Loss factor vs. Normalised fatigue life for ±45° Laminate [1] . . . 7
2.7 Effective Loss factor vs. Maximum stress for ±45° Laminate [1] . . . 8
2.8 Dissipated energy per cycle as a function of normalized fatigue life for the $[0/90]_{4s}$ UD E-glass/BT080-epoxy laminate, illustrating a predominantly stable plateau followed by a rapid increase near the end of life at $N/N_f \approx 1$ [1]. . . . 9
2.9 Critical Dissipated Energy vs. Maximum Gauge stress for $[0/90]_{4s}$ UD E-glass/BT080-epoxy laminate [1] . . . 10
2.10 Dissipated energy per cycle versus normalized fatigue life for the ±45° laminate, illustrating a predominantly monotonic increase throughout the fatigue life and no clearly defined final failure transition.[1] . . . 10
2.11 Average Complex Modulus over fatigue life vs. maximum stress level for $[0/90]_{4s}$ UD E-glass/BT080-epoxy laminate [1] . . . 11
2.12 S–N curves for the $[0/90]_{4s}$ UD E-glass/BT080-epoxy laminate, illustrating the good agreement between the predicted and experimental response at $R = 0.3$, achieved through the application of only the R-ratio scaling terms.[1] . . . 12
2.13 Generalized stress-strain curves for (a) linear elastic, (b) linear viscoelastic, (c) material nonlinearity, (d) interactional nonlinearity [23] . . . 13
2.14 Three-stage creep phenomena [24] . . . 14
2.15 Schematic diagram of a creep-recovery test [27] . . . 15
2.16 Generalized material responses for ideal elastic, viscoelastic and ideal viscous materials [30] . . . 15
2.17 Determination of T_g on a E' vs. T graph for ±45° glass/epoxy [29] . . . 16
2.18 Storage Modulus vs. Temperature [31] . . . 16
2.19 Loss Modulus vs. Temperature [31] . . . 17
2.20 Loss Factor vs. Temperature [31] . . . 17
2.21 Quasi-static stress-strain curves for GFRP ±45° laminates [34] [29] . . . 18
2.22 Influence of strain rate on the stress-strain curves of GFRP ±45°, illustrating the increase in the tangent stiffness with increasing strain rate. [25] . . . 18
2.23 Creep curves at different stress levels for GFRP ±45° [29] . . . 19
2.24 The corresponding light transmittance at different stages of creep for 70MPa stress level [29] . . . 19
2.25 Interrupted (A) and creep-fatigue (B) loading patterns . . . 20
2.26 S–N curves for the different loading patterns, illustrating the influence of creep and interrupted loading on fatigue life. Conf denotes constant-amplitude fatigue loading, Cref (2 h) and Cref (48 h) denote creep–fatigue loading with 2 h and 48 h creep periods inserted between fatigue loading blocks, respectively, and Intf denotes the interrupted-fatigue loading pattern. [29] . . . 21
2.27 S–N curves for loading frequencies of 3.6 Hz and 0.417 Hz, illustrating the frequency-dependent fatigue response and the cross-over in fatigue life between the two loading frequencies [25]. . . . 22
2.28 Hysteresis loop evolution for (A) 68 MPa and (B) 47 MPa [29] . . . 22
2.29 Hysteresis loop evolution for (A) 64 MPa and (B) 49 MPa [29] . . . 23
2.30 Hysteresis loop evolution for (A) 70 MPa and (B) 47 MPa [29] . . . 23
2.31 Back shift of hysteresis loops [29] . . . 24
2.32 Normalized fatigue stiffness vs. cycles to failure for continuous fatigue loading pattern [29] . . . 24
2.33 Normalized fatigue stiffness, E_N/E_1, versus normalized fatigue life, N/N_f, for the interrupted-fatigue (Intf) loading pattern. In the legend, "Intf" denotes interrupted-fatigue loading, 0.1 denotes the stress ratio $R = 0.1$, the values 49, 53, 58, and 64 indicate the applied maximum stress in MPa, and the final letters identify the individual specimens [29] . . . 25

2.34 Normalized fatigue stiffness, E_N/E_1, versus number of cycles, N, for constant-amplitude fatigue (Conf) and creep–fatigue (Cref) loading. In the legend, "Conf" denotes constant-amplitude fatigue loading and "Cref" denotes creep–fatigue loading; 0.1 denotes the stress ratio $R = 0.1$, 68 and 47 indicate the applied maximum stress in MPa, and the final letters identify individual specimens. (A) Results at 68 MPa; (B) results at 47 MPa [29] . . . 25
2.35 Normalized Stiffness vs. Normalised Life [25] . . . 26
2.36 Cyclic creep rate vs. Normalized life [25] . . . 26
2.37 Normalized maximum stress vs. (a) cycles to failure, (b) steady rate of cyclic creep [25] . . . 27
2.38 Thermal and optical damage evolution under different fatigue loading conditions [29]. . . . 28
2.39 Thermal and optical damage evolution under different creep-fatigue loading patterns [29]. . . . 28
2.40 Failed Specimens Images . . . 29
2.41 "Closed" Loop Assumption as depicted in Krieg's thesis [1] . . . 30

3.1 Example plot of the recovery curves from Schapery et al. [26] . . . 39
3.2 Example Plot of the master curve from Schapery et al. [26] . . . 40
3.3 Schematic overview of the nonlinear parameter-identification procedure. Numbered circles denote the sequential identification steps, while rectangular boxes indicate the quantities or model parameters obtained as outputs from each step and subsequently used to determine the final augmentation term. . . . 41
3.4 Schematic of TDE/W_{tot} per stress-level allowing determination of the *damaged* stress levels, and the fatigue limit. . . . 42

4.1 Comparison of specimen geometries: rectangular, single-radius, double-radius, linear-taper, and double-Euler profiles. The gauge width was held constant across all five geometries to maintain the same nominal gauge stress for direct comparison; this constant gauge width is not accurately represented in the schematic. . . . 46
4.2 S11 normal stress (left) and S12 shear stress (right) against the clamp-to-clamp distance of the specimen, for the five geometry concepts. . . . 47
4.3 S11 normal stress (left) and S12 shear stress (right) against the clamp-to-clamp distance of the specimen, for a narrowing ratio of 0.68, 0.71 and 0.78. . . . 48
4.4 Final Specimen Geometry and Dimensions . . . 48
4.5 Side-by-side view of ABAQUS sketch (left) and real-life specimen (right), showing the Double Euler Geometry. . . . 49
4.6 Evolution of strain rate as a consequence of stiffness degradation in GFRP laminates. . . . 50
4.7 Comparison of Normalized stiffness degradation between $[0/90]_{2s}$ (a) vs. $[+45/0/-45/90]_s$ (b) at the same stress level [48] . . . 50
4.8 Feasible combinations of strain rate and R-ratios, and consequent required frequencies for desired stress levels. The tested point markers indicate the experimental conditions evaluated at selected combinations of maximum stress, R-ratio and corresponding loading frequency. . . . 53
4.9 Comparison of the practical cutting process and the corresponding cutting pattern. . . . 54
4.10 Vacuum Bag Set-Up Prior to Autoclave curing cycle. . . . 54
4.11 The clamping of the tabs bonded onto the specimens, prior to oven. . . . 55
4.12 Surface texture imprinted on the specimen during processing, showing (a) the textured specimen surface and (b) the release-foil texture responsible for the transferred imprint. . . . 56
4.13 MTS 100kN Servo-Hydraulic machine used for tensile, SST, CA Fatigue and Creep tests. . . . 57
4.14 Stiffness degradation at 65% UTS and $R = 0.3$, and the corresponding target loading frequency required to maintain the prescribed strain rate. . . . 60
4.15 Program for Mechanically Conditioning . . . 60
4.16 Zwick 200 kN mechanical testing setup equipped with a thermal chamber and specimen arrangement for creep/recovery testing. . . . 61
4.17 3PB configuration on TA Instruments RSA-G2 solids analyser for DMA Testing. . . . 62

5.1 Monotonic Tensile test results at quasi-static (QS) 2 mm/min and fatigue-equivalent (FE) 7.8 mm/s . . . 63
5.2 Re-orientation Angle vs. Strain for monotonic tensile tests. . . . 64
5.3 Cyclic Stress-Strain Data resulting in Hysteresis Loops (50% UTS R=0.1). . . . 65

5.4 Stiffness Degradation E/E_0 over the Normalized fatigue lives. For the exact stress levels and corresponding test conditions, refer to the test matrix in Table 4.7. . . . 66
5.5 Re-orientation Angle vs. Strain for 80% UTS R=0.1 Fatigue Test. . . . 66
5.6 Strain-Rate Evolution over the normalized fatigue lives. For the exact stress levels and corresponding test conditions, refer to the test matrix in Table 4.7. . . . 67
5.7 Average Stabilized Stiffness Values across stress-levels and R-ratios. . . . 67
5.8 Mean Strain Progression over the normalized fatigue lives. For the exact stress levels and corresponding test conditions, refer to the test matrix in Table 4.7. . . . 68
5.9 Fatigue Failure Strain vs. Stress Level . . . 68
5.10 Dissipated Energy over the normalized fatigue lives. For the exact stress levels and corresponding test conditions, refer to the test matrix in Table 4.7. . . . 69
5.11 Applied Energy over the normalized fatigue lives. For the exact stress levels and corresponding test conditions, refer to the test matrix in Table 4.7. . . . 70
5.12 Loss factor W_{diss}/W_a over the normalized fatigue lives. For the exact stress levels and corresponding test conditions, refer to the test matrix in Table 4.7. . . . 71
5.13 Viscoelastic Loss factor $\sin(\phi)$ over the normalized fatigue lives. For the exact stress levels and corresponding test conditions, refer to the test matrix in Table 4.7. . . . 71
5.14 Recovery Strain Curves against reduced time, before (left) and after (right) shifts . . . 72
5.15 Fitted creep strain vs. time curves for 20%, 25%, 30% and 35% UTS . . . 73
5.16 Required Augmentation Parameters, in relation to yielded Parameters from Creep-Recovery tests. 74
5.17 Comparison of the fatigue-life predictions obtained using the original Krieg formulation and the augmented model. . . . 74
5.18 Bilinear fits used to identify the fatigue-limit transition for stress ratios of $R = 0.1$ and $R = 0.3$. . . 75
5.19 Fatigue Life Predictions for R=0.1 and R=0.3 using Miner's rule on Stress-sweep tests. . . . 75
5.20 Fatigue Life Predictions for R=0.3, 0.5 and 0.7 using input R=0.1 from SST Miner's rule. . . . 76
5.21 Fatigue Life Predictions for R=0.1, 0.5 and 0.7 using input R=0.3 from SST Miner's Rule. . . . 76
5.22 Storage Modulus and Loss Factor vs. Temperature (DMA) . . . 77
5.23 Effective Loss Factors vs, Stress level for the different R-ratios, and HCFS determination using pristine DMA loss factor of 0.022. . . . 78
5.24 Fatigue Life Predictions for R=0, 0.3, 0.5 and 0.7 using input R=0.1 with Krieg-Schapery augmentation, incorporating UTS values obtained from the monotonic tensile (MT) results . . . 79

A.1 Dynamic modulus evolution and corresponding continuous and MPT-programmed target frequency for 50% UTS at $R = 0.1$. . . . 89
A.2 Predicted dynamic modulus evolution and corresponding continuous and MPT-programmed target frequency for 60% UTS at $R = 0.1$. . . . 89
A.3 Predicted dynamic modulus evolution and corresponding continuous and MPT-programmed target frequency for 62% UTS at $R = 0.1$. . . . 89
A.4 Dynamic modulus evolution and corresponding continuous and MPT-programmed target frequency for 65% UTS at $R = 0.1$. . . . 90
A.5 Predicted dynamic modulus evolution and corresponding continuous and MPT-programmed target frequency for 60% UTS at $R = 0.3$. . . . 90
A.6 Dynamic modulus evolution and corresponding continuous and MPT-programmed target frequency for 65% UTS at $R = 0.3$. . . . 90
A.7 Predicted dynamic modulus evolution and corresponding continuous and MPT-programmed target frequency for 70% UTS at $R = 0.3$. . . . 91

B.1 Proposed workflow for applying, validating and adapting the fatigue-life prediction framework to new material systems, fibre orientations, stress ratios and loading conditions. . . . 97

List of Tables

4.1 Material properties of the glass-fibre UD prepreg system [1]. . . . 45
4.2 Summary of tab-design parameters. . . . 46
4.3 Summary of selected fatigue loading parameters. . . . 53
4.4 Curing cycle steps and specifications. . . . 55
4.5 Measured Coupon Dimensions for the Different Mechanical Tests. . . . 56
4.6 Stress-sweep loading programmes for $R = 0.1$ and $R = 0.3$. . . . 58
4.7 Fatigue test conditions for the different stress levels and stress ratios. . . . 59
4.8 MTS MPT programming sequence for 65% UTS at $R = 0.3$. . . . 59
4.9 Creep testing conditions for specimens 7.1 and 7.2. . . . 61
4.10 DMA test parameters. . . . 62

5.1 Fatigue test results for different stress ratios. . . . 65
5.2 Identified Lou–Schapery model parameters at the investigated stress levels. . . . 73

A.1 MTS MPT programming sequence for 50% UTS at $R = 0.1$. . . . 89
A.2 MTS MPT programming sequence for 60% UTS at $R = 0.1$. . . . 89
A.3 MTS MPT programming sequence for 62% UTS at $R = 0.1$. . . . 89
A.4 MTS MPT programming sequence for 65% UTS at $R = 0.1$. . . . 90
A.5 MTS MPT programming sequence for 60% UTS at $R = 0.3$. . . . 90
A.6 MTS MPT programming sequence for 65% UTS at $R = 0.3$. . . . 90
A.7 MTS MPT programming sequence for 70% UTS at $R = 0.3$. . . . 91

B.1 Suggested minimum number of specimens for the proposed experimental programme. . . . 93

1 Introduction

Fibre-reinforced composite materials are an increasingly popular choice for structural applications where the priority lies in low density yet high strength, stiffness and resistance to environmental degradation. However, their behaviour under cyclic loading remains considerably more difficult to predict than conventional metallic structures. Fatigue damage in composites develops through matrix cracking, fibre-matrix interface degradation, delamination, and fibre breakage. Their contributions to failure depend not only on the applied load, but also on the laminate structure, the stress ratio, the loading rate, temperature and time-dependent nature of the matrix. Therefore, characterization of these materials under fatigue remains strongly dependent on extensive experimental campaigns.

The conventional S-N curve plots various stress ranges and their corresponding number of cycles to failure. Constructing these curves requires extensive experimental tests for multiple specimens to obtain an accurate range of orders of magnitude in fatigue life. This empirical effort increases further when separate curves are required for any variable difference e.g. stress-ratio, loading rate, temperature and/or laminate configuration. Particularly towards the lower stress levels, required testing may take days or weeks of continuous cyclic loading. More efficient physics-based approaches capable of estimating fatigue behavior from shorter material-characterization tests could offer considerable scientific and practical value.

This thesis aims to contribute to the ongoing work within the department of Aerospace Structures and Materials to reduce the reliance on extensive fatigue-testing campaigns for fibre-reinforced polymer composites across a wide range of loading and environmental conditions. The objective is to contribute to a unified physics-based approach that has the capacity to predict fatigue behaviour with sufficient accuracy while requiring substantially less fatigue testing. Therefore, it warrants a deeper understanding of the underlying macro-scale energy-based fatigue behavior, which could provide a promising path towards making all fatigue testing obsolete.

The ongoing research originated from the hypothesis on whether the ratio between Total Dissipated Energy (TDE) and Total Work (TW) might remain fixed or follow a predictable trend for a given composite, which could potentially be estimated from simpler tests like monotonic tensile tests. Lennart Krieg [1] developed a modified viscoelastic framework that models strain dissipated energy per cycle, and its summation values, thereby effectively predicting fatigue life at different stress-ratios. He validated the framework using a fibre-dominated 0/90 laminate, where applicability to matrix-dominated laminates remains uncertain.

Matrix-dominated laminates generate pronounced shear-dominated deformation with aspects like non-negligible creep, ratcheting and nonlinear viscoelastic effects. These mechanisms introduce time-, rate- and stress-dependent behavior which challenges the linear-viscoelastic assumptions in Krieg's original formulation. Therefore, this thesis investigates a potential extension to the framework, specifically focusing on the $\pm 45^\circ$ configuration.

The central motivation of the thesis lies in answering the following question,

To what extent can a physics-based fatigue prediction framework developed for fibre-dominated composites be retained for a matrix-dominated laminate, and can the additional physical mechanisms responsible for its deviations instead be leveraged to extend the framework?

To address this, the thesis begins with a literature study in Chapter 2, covering Krieg's framework, its main findings and where it breaks down for $\pm 45^\circ$ laminates, highlighting the major research gaps, and the corresponding research questions that guide the current study. Chapter 3 explores a potential extension of Krieg's framework that leverages the inherent nature of $\pm 45^\circ$ laminates, and also presents the approach to identify the model parameters for it. Chapter 4 describes the experimental campaign of the five principal testing types conducted to obtain input and validation data for the thesis, where concepts such as ideal specimen geometry and strain-rate control methods are discussed. The results, discussion and limitations are presented in Chapter 5 where the proposed methods and their applicability in relation to the validation data are discussed. Finally, Chapter 6 draws conclusions from the main findings and its significance to the broader field of research, with further recommendations to advance it.

2 Literature Review

In this chapter, a review of the existing literature on the fatigue behavior of matrix-dominated fibre-reinforced polymer composites is presented. Central to this review is the modified linear viscoelastic framework developed by Lennart Krieg (2025), and its position within the broader context of this field; physics-based fibre-reinforced composite fatigue modeling. Through a critical assessment of the applicability of this framework to matrix-dominated laminates, the gaps in the current state of knowledge are highlighted, establishing the basis for extending this framework to these composite configurations.

Section 2.1 establishes the general theoretical background of fatigue in fibre-reinforced composites and positions Lennart Krieg's framework within the broader field. Section 2.2 then presents the framework itself and its intended application. Thereafter, Section 2.3 explores the challenges associated with extending this framework to matrix-dominated composites. Finally, Section 2.4 narrows the discussion to the central focus of this thesis, consolidating the research gaps identified throughout the review and formulating the corresponding research questions.

2.1. Theoretical Background

Fatigue research on metals has been the subject of extensive research with a well-established history from the 1800s. However, fatigue research on composite materials is relatively new and significantly more complex [2]. A fibre-reinforced composite cannot be compared to an isotropic metallic material as it is a *structural system*, composed of interdependent factors such as fibre type, resin type, fibre volume fraction, stacking sequence, curing cycle, and manufacturing method [3]. In addition, with composites, there is no dominant failure mode. Fatigue of metals follows a localized phenomenon where it follows the nucleation of a crack from persistent slip bands which is then followed by stable crack growth, described by the Paris Law and eventually, leading to failure [4]. In contrast, composites degrade through a synergistic interaction of multiple mechanisms such as matrix cracking, fiber breakage, delamination and debonding [5]. Therefore, fatigue behavior of composite materials cannot be described by a single, universal law and requires complex multi-parameter approaches accounting for interacting factors.

Fatigue damage assessment methods for composites can broadly be distinguished according to whether damage is characterized directly or inferred from changes in the material response [6]. Direct characterization may involve non-destructive testing (NDT), such as computed tomography or ultrasonic inspection, to identify physical damage, or destructive testing to assess properties such as residual strength. A limitation of these approaches is that they may require the fatigue test to be temporarily interrupted or terminated. Interruptions in cyclic loading can influence the subsequent material response due to time-dependent recovery effects [7]. Therefore, uninterrupted fatigue testing is preferred unless the phenomenon of creep is the focus, which can be seen in Movahedi et al. [8]'s paper on interrupted tensile-tensile testing of ±45° glass/epoxy laminates including recovery phases.

Alternatively, damage evolution can be assessed indirectly by monitoring changes in measurable material properties during cyclic loading. These approaches are well suited to continuous fatigue monitoring because they can provide information on damage development without interrupting the test. Commonly used indicators include the dynamic modulus and energy dissipation [2]. The dynamic modulus is the effective stiffness between the two extremes of a hysteresis loop, while the energy dissipation is quantified by the area of the hysteresis loop (Figure 2.1), representing the irreversible work done on the material.

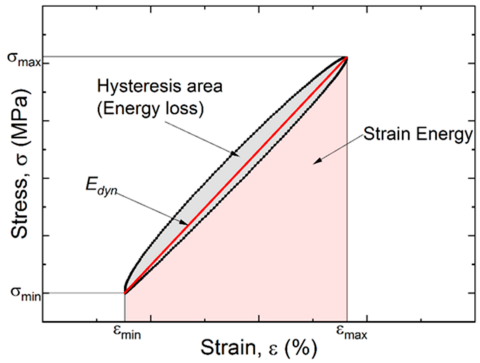


Figure 2.1: *Hysteresis Loop [9]*

The hysteresis loop provides a "snapshot" of the energy metrics during one cycle, while fatigue failure is inherently a cumulative process. To capture the full history of degradation, literature proposes summing up these instantaneous "snapshots" of energy dissipation into cumulative energy parameters. Movahedi-Rad et al. [10] [11] extensively explored the hypothesis of a Total Dissipated Energy (TDE) criterion, as an "energy budget" the material can dissipate before failure.

$$TDE = W_{total} = \sum_{i=1}^{N_f} W_{h,i} \tag{2.1}$$

They suggested that the relationship between the TDE and the maximum cyclic stress follows a power-law, also defining the total energy dissipated as composed of two components: cyclic dissipation and creep dissipation.

$$W_{total} = W_{cyclic} + W_{creep} \tag{2.2}$$

While fibre-dominated composites experience negligible W_{creep}, matrix-dominated systems experience significant creep. Movahedi-Rad et al. proposed shift factors ψ as a function of different stress ratios (R) and temperatures (T) to normalize TDE data, implying that if the rate of the dissipation during one cycle can be modeled (e.g. via viscoelastic theory), the fatigue life can be predicted by determining the time required to accumulate to the critical TDE.

Complementary to the 'output' dissipated energy approach is the 'input' energy theory, pioneered by El-Kadi and Ellyin [12] [13]. They argued that the driving force for fatigue damage is the total applied strain energy during the loading of the material.

$$\Delta W_{in} = \Delta W_{elastic} + \Delta W_{inelastic} \tag{2.3}$$

Due to the difficulty of quantifying heat loss, it was assumed to be negligible by El-Kadi and Ellyin [12] [13]. They created a power law equation where higher input energy implied fewer cycles to failure. This approach is particularly useful for multi-axial stress states (as those in ±45°) [14]. Researchers Mandegarian and Taheri-Behrooz [15] tried to improve this model by normalizing the input energy by the static input energy which allowed them to take data from different off-axis UD fiber angles and collapse them onto a single curve. This can be seen in Figure 2.2. The main flaw with using the input energy is assuming it stays constant as in reality, the material's stiffness degrades and therefore, the amount of energy absorbed per cycle changes. This limits the applicability of the theory to a limited selection of off-axis unidirectional cases.

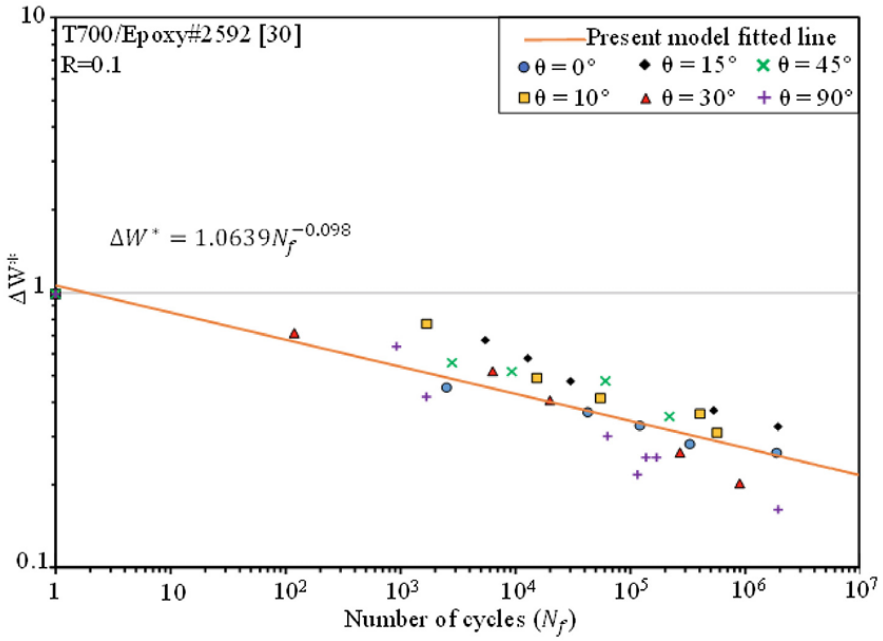


Figure 2.2: *Normalized strain energy density as a function of fatigue life for different off-axis fibre orientations, illustrating the collapse of the experimental data onto a common master curve [15]*

Lennart Krieg's thesis explores a significant step towards operationalizing both these 'input' and 'output' energy concepts. Krieg identified that literature evaluates TDE and TW values as isolated scalar totals. In contrast, Krieg focused on the evolution of the instantaneous dissipation ratio across the fatigue life, the cumulative effect which leads to the TDE/TW ratio. This metric was then linked to the viscoelastic loss factor, and explicitly accounted for R-ratio effects on the energy input - effectively, modifying linear viscoelastic vibration damping theory to create a more consistent, R-ratio-independent fatigue evaluation model [16]. This will be explained further in the following section.

2.2. The Modified Linear Viscoelastic Framework

In this section, the central framework developed by Lennart Krieg is presented, providing the theoretical foundation for subsequent developments. Subsection 2.2.1 introduces the theoretical mechanics of the framework, and Subsection 2.2.2 presents his main findings and their applicability to matrix-dominated composites highlighting the gaps that necessitate the current research extension.

2.2.1. Framework

Lennart Krieg's framework essentially leverages classical linear viscoelastic theory by adapting rheological models such as Maxwell and Kelvin-Voigt but avoiding their direct implementation. Representing the material response explicitly through combinations of springs and dampers in series and/or parallel would require extensive characterization of the relevant elastic moduli and viscosities, which in practice would typically necessitate interrupted fatigue testing. Motivated by the need for a more practical framework suitable for general application, Krieg instead introduced the concept of a complex spring stiffness to model the pure cyclic hysteresis. In this representation, the material response is described using a complex modulus E^*, in which the real component, E', represents the elastic or storage contribution, while the imaginary component, E'', accounts for the viscous or dissipative contribution. This formulation therefore retains the essential viscoelastic behaviour of the material while reducing the experimental characterization required for its application. The following equation shows the corresponding stress-strain relation,

$$\epsilon_h(t) = \left(\frac{1}{E' + iE''}\right)\sigma(t). \tag{2.4}$$

The formulation above describes only the cyclic hysteretic response and does not explicitly account for ratcheting or creep-induced translation of the hysteresis loops. To summarise, Krieg makes two fundamental modeling assumptions,

1. **Decoupling Hysteresis and Creep**

   For fibre-dominated composites, the creep strain accumulation can be considered negligible in comparison to the cyclic hysteresis. The cyclic hysteresis loop is treated as a closed loop, while creep is treated as a separate function that shifts the position of the loop as a function of time, which remains minimal in fibre-dominated composites (see Figure 2.3). In other words, this assumption addresses the exclusion of the viscoplastic factor into the modeling.

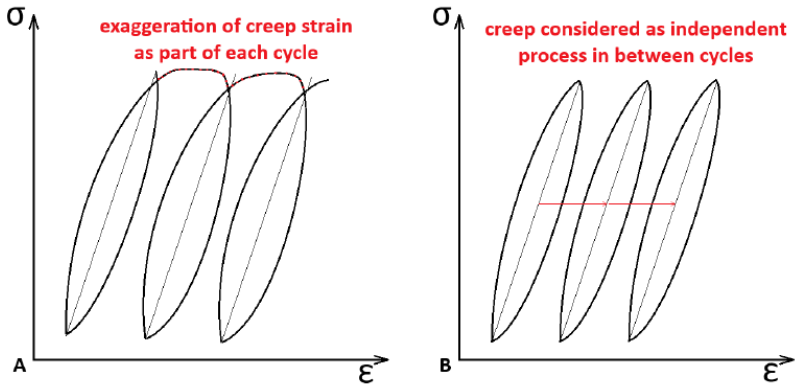


Figure 2.3: *Visual Representation of decoupling hysteresis and creep, illustrating the assumed model (B) compared to reality (A) [1]*

2. **Linear Viscoelasticity**

   The behavior follows classical linear viscoelastic theory, therefore stress-dependent nonlinear viscoelastic effects are unaccounted for. So, this assumption addresses the exclusion of the nonlinear viscoelastic effects.

By expressing the complex stiffness in terms of its magnitude and the corresponding viscous phase angle, the formulation gains a more direct physical interpretation in the context of the hysteresis loop. The magnitude of the complex stiffness governs the overall slope of the loop, while the phase angle describes the viscoelastic lag between the applied stress and resulting strain. These quantities can be written as,

$$E^* = |E^*|e^{i\delta}, \qquad |E^*| = \sqrt{E'^2 + E''^2}, \qquad \delta = \tan^{-1}\left(\frac{E''}{E'}\right). \tag{2.5}$$

Using this representation, Krieg subsequently defined the dissipated energy per cycle as the area enclosed by the closed hysteresis loop. By applying Green's theorem, this enclosed area can be evaluated as a line integral along the loop boundary, yielding an expression for the hysteretic energy dissipation ΔW. An important consequence of this formulation is that the mean stress terms originally present in the stress and strain descriptions vanish when the differentials required by Green's theorem are taken. As a result, the classical linear viscoelastic formulation naturally corresponds to fully reversed loading, for which $\sigma_{\text{mean}} = 0$. Krieg therefore argued that an additional correction is required when extending the formulation to other stress ratios. Although two loading conditions may have the same stress amplitude, the total applied work can differ geometrically as a consequence of their different R-ratios. To account for this, the dissipated energy is scaled by the ratio between the work associated with the considered R-ratio and the work corresponding to the reference condition R = -1. A further correction term is introduced to compensate for energy contributions that are not inherently captured by the conventional viscoelastic loss factor. The resulting corrected dissipated-energy formulation can therefore be written as

$$W_h = \Delta W \cdot \frac{W_a}{W_{ref}} \cdot \left(\frac{\sigma_a}{\sigma_m}\right)^2. \tag{2.6}$$

These cycle-level quantities can then be accumulated over the fatigue life to obtain integral measures of the overall material response. In particular, the dissipated energy and applied work calculated at each cycle can be summed to define the total dissipated energy, TDE, and total work, TW, respectively:

$$TDE = \frac{\pi\sigma_{\max}^2}{2}\frac{(1-R)^3}{1+R}\sum_{i=1}^{N_f}\frac{\sin(\phi_i)}{|E_i^*|}, \qquad TW = \frac{\sigma_{\max}^2(1-R^2)}{2}\sum_{i=1}^{N_f}\frac{1}{|E_i^*|} \quad \text{for } 0 \le R \le 1. \tag{2.7}$$

And its ratio,

$$\frac{TDE}{TW} \approx \pi\left(\frac{1-R}{1+R}\right)^2 \sin(\phi_{eff}). \tag{2.8}$$

The effective loss factor $\sin(\phi_{eff})$ is the energy weighted average of the individual cycle loss factor values of each cycle. These cumulative measures form the basis of Krieg's fatigue-life prediction framework. Of particular relevance to the present thesis is the hypothesis that the relationship between TDE and the maximum applied stress, $\sigma_{\max}$, follows a constant power-law relationship that is effectively independent of the applied stress ratio. Under this assumption, a life-prediction relation can be derived,

$$N_{f_{R_2}} = N_{f_{R_1}} \cdot \frac{\left(\frac{1-R_1}{1+R_1}\right)^2}{\left(\frac{1-R_2}{1+R_2}\right)^2} \cdot \frac{1-R_1^2}{1-R_2^2} \cdot \frac{|E^*|_{avg,R_2}}{|E^*|_{avg,R_1}} \cdot \frac{\sin(\phi_{eff})_{R_1}}{\sin(\phi_{eff})_{R_2}} \tag{2.9}$$

The central implication is that, if the evolution of stiffness degradation or the viscoelastic loss factor can be transferred or estimated between two different stress ratios, then the fatigue life at a target ratio R_2 may be predicted using experimental information obtained at a reference ratio R_1.

The primary objectives of Krieg's thesis were therefore to evaluate the evolution of the effective loss factor under fatigue loading and to assess the validity of the proposed energy-based life prediction framework. Fatigue tests were conducted at different maximum stress levels and at stress ratios of $R = 0.1$ and $R = 0.3$, with

particular attention given to how the loss factor evolved throughout the fatigue life and whether comparable trends could be identified between the two loading conditions. A further objective was to verify whether the proposed relationship between total dissipated energy, TDE, and maximum stress remained effectively independent of stress ratio. The resulting life predictions were then compared directly with experimental fatigue lives to assess the predictive capability of the model. In addition, Krieg investigated whether the pristine loss-factor values obtained from dynamic mechanical analysis (DMA) could be related to the effective loss factors measured during fatigue testing, with the aim of determining whether the high-cycle fatigue strength (HCFS) could be estimated from these pristine DMA viscoelastic properties.

2.2.2. Main Findings

Krieg presents several key findings; however, their applicability to matrix-dominated composites remains uncertain, thereby defining the principal research gaps addressed in the present study.

- **Loss Factor as a Unified Energy Dissipation Metric, and its dependence on stress level and R-ratio.**

  Krieg argues that analysing stiffness degradation or dissipated energy in isolation provides an incomplete description of fatigue damage. Instead, he suggests that the loss factor, $\sin\phi$, is a more descriptive parameter because it captures the combined effects of complex modulus degradation, changes in viscous losses, and friction-driven damping. A key limitation of using the raw energy measures, TDE and TW, is that their absolute values vary with stress ratio. However, through Krieg's R-ratio correction, these offsets are normalized, allowing a more direct and unified comparison between different stress ratios.

  Krieg noted that the loss factor trends were more conclusive than pure energy scalars. For example, the loss factor trend of 0/90 laminates is given in Figure 2.4. The first cycles show high dissipation and a larger loss factor relating to the immediate damage initiation in the 90° plies and at 0-90 interfaces. For the remainder of its life, the loss factor stabilizes for low stresses, while at high stresses, it increases steadily.

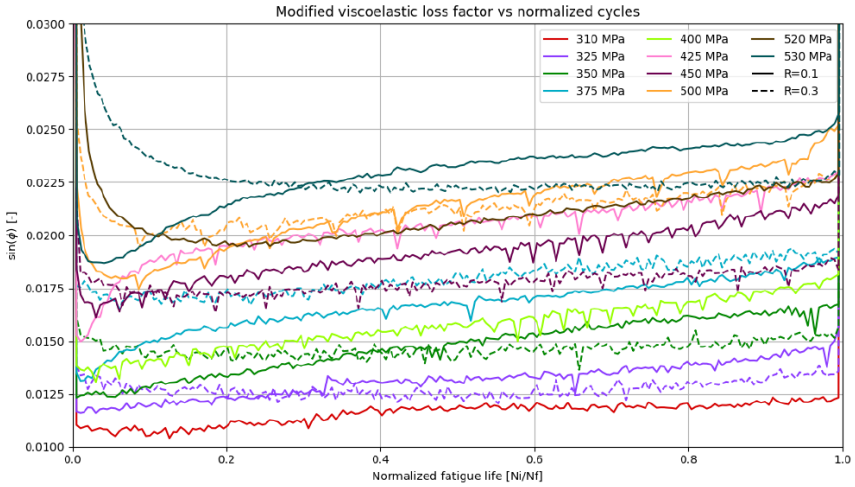


Figure 2.4: *Modified Viscoelastic Loss factor vs. Normalized fatigue life for* $[0/90]_{4s}$ *UD E-glass/BT080-epoxy laminate [1]*

Figure 2.4 shows the loss factor trends for both R=0.1 and R=0.3 and despite the differences in the early stage, the loss factors converge in the second half of the fatigue life, suggesting that R-ratio mainly affects the damage initiation and early propagation, while long-term damage evolution and saturation are governed by the cyclic maximum stress. The relation between the loss factor and stress-level along with loss factor and R-ratio could be conclusively drawn from one trend curve. In addition, Figure 2.5 shows that the effective loss factor increases almost linearly with the maximum cyclic stress and data from the two different stress ratios collapse onto a single linear trend, thereby validating the independence of R-ratio for these laminates.

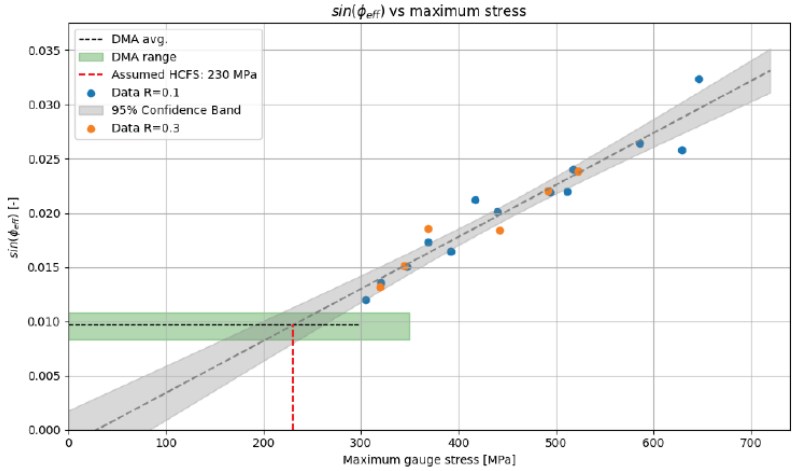


Figure 2.5: *Effective Loss factor vs. Maximum gauge stress for* $[0/90]_{4s}$ *UD E-glass/BT080-epoxy laminate [1]*

Applicability to Matrix-Dominated Composites

Krieg performed a preliminary analysis where he used ±45° fatigue data from Movahedi-Rad et al. [8] to see preliminary applicability of his proposed framework. Figure 2.6 shows the loss factor trend as a function of normalised fatigue life.

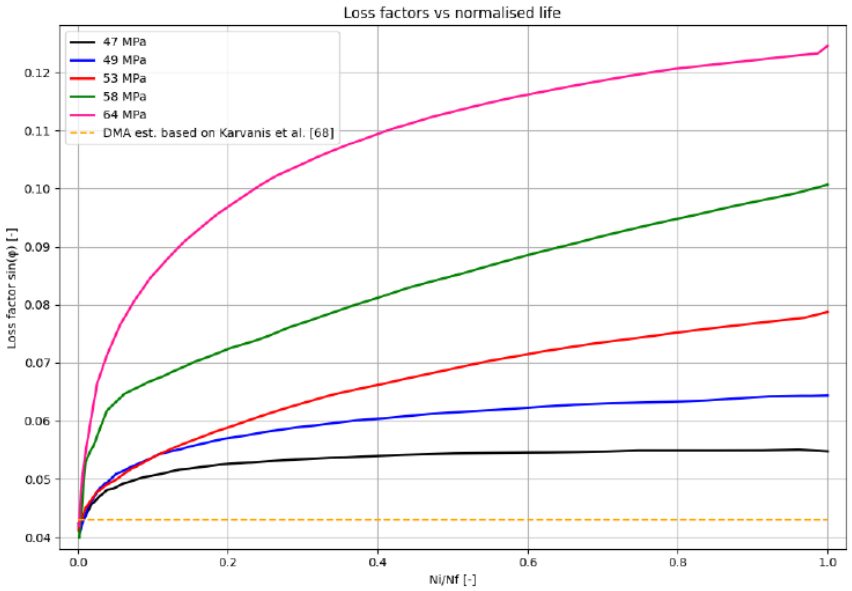


Figure 2.6: *Modified Viscoelastic Loss factor vs. Normalised fatigue life for* ±45° *Laminate [1]*

The early stages show a rapid increase in loss factor. At lower maximum stresses, the factor stabilizes while for higher stresses, there is continuous growth of the loss factor. The difference in trend between the stress levels is similar to that observed for the 0/90 laminates; however, the loss-factor magnitudes are significantly higher for the ±45° laminates. Similarly to the 0/90 laminates shown in Figure 2.5, the ±45° laminates showed a similar linear dependency on the stress level even though the damage mechanisms are different. This is shown in Figure 2.7.

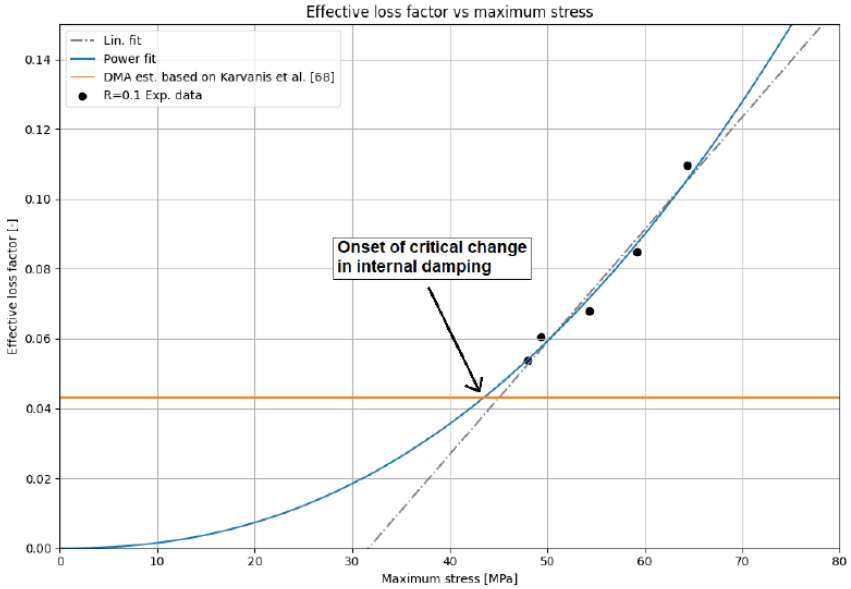


Figure 2.7: *Effective Loss factor vs. Maximum stress for* ±45° *Laminate [1]*

However, the dependence of R-ratio for ±45° remains unexplored. In addition, it is still of question whether the collapse would occur as neatly for higher R-ratios close to 1.0 due to the presence of creep and nonlinearities that are not accounted for here.

For the case of 0/90 laminates, the complex modulus remained relatively constant implying that the linear dependence of the stress level arises from the weighted average loss modulus. However for ±45° laminates, both the complex modulus and the loss modulus were observed to be varying across the tests despite resulting in similar loss factor trends.

Although the loss factor provides a conclusive description of both the R-ratio and maximum stress dependence, its interpretation cannot be decoupled from the underlying evolution of the storage and loss moduli when comparing different laminate architectures. In particular, although similar stress-dependent loss factor trends are observed for both 0/90 and ±45° laminates, these trends arise from fundamentally different mechanisms. In 0/90 laminates, the near-constant complex modulus suggests that the observed behaviour is primarily driven by changes in the loss modulus. In contrast, for the matrix-dominated ±45° laminates, concurrent variations in both the complex and loss moduli contribute to the loss factor evolution. This challenges the notion that the loss factor alone constitutes a universally superior damage metric, as previously suggested by Krieg, and highlights the necessity of analysing the individual moduli to fully interpret fatigue damage mechanisms across different stacking sequences. Consequently, a deeper investigation into the dependence of the loss factor on R-ratio and stress level for ±45° laminates is warranted, particularly to assess whether consistent and predictive trends exist and/or whether the inherent complexity of matrix-dominated composites requires the use of multiple complementary damage metrics.

> **Gap-01:** Limited understanding of R-ratio and stress-level dependence on the loss factor for ±45°, and whether its use as a standalone damage metric adequately captures the underlying fatigue mechanisms.

- **Correlation between DMA-Derived Loss Factors and High-Cycle Fatigue Strength.**

  As mentioned in Krieg's thesis, literature [17] [18] [19] [20] states that there exists a transition point where there is a noticeable sharp increase in the energy dissipation and internal damping, resulting in dual-linear thermography plots, highlighted as the HCFS point. For the 0/90 laminates, the pristine loss factor values from DMA intersected the fatigue loss factor curves at 230 ± 30 MPa, matching the general

10^6–10^7 fatigue limits typically evaluated in literature [18]. This is shown in Figure 2.5. This intersection point matches the fatigue limit experimentally acquired by Broughton et al. [21] of 214 - 285 MPa. This correlation allows the HCFS to be predicted by measurable and physical damping quantities.

Applicability to Matrix-Dominated Composites

Krieg's preliminary analysis on ±45° also showed conclusive validity of this. Figure 2.7 shows the effective loss factor as a function of stress level, where the power-law fit (similarly to the linear fit) provides an intersection at 43 and 45 MPa, which correlates to the endurance limit of 45-50 MPa by Liang et al. [22] and the HCFS estimation of 37 MPa by Colombo et al. [20].

A limitation of this finding is that direct experimental validation of this endurance limit is limited, which is inherently constrained by the prohibitively long testing times required at very high cycle fatigue regimes. So despite the good agreement between this intersection point and literature values, the estimated HCFS ranges such as 214 to 285 MPa and 37 to 50 MPa, for 0/90 and ±45° respectively, cannot be further narrowed. For the 0/90 laminates, the collapse of the stress-dependent loss factor trends for both R-ratios onto a single curve enabled the identification of a unique intersection with the pristine DMA-derived loss factor, supporting a well-defined HCFS estimate. In contrast, the absence of corresponding R-ratio dependence data for the ±45° laminates introduces ambiguity. Without establishing whether the loss factor behaviour of the ±45° laminate is similarly R-ratio independent, it remains unclear whether multiple HCFS intersection points exist and how such intersections should be physically interpreted.

> **Gap-02:** Unverified validity of the loss-factor intersection method for HCFS identification, for ±45°.

- **From Total Dissipated Energy metric to Critical Dissipated Energy metric.**

  Total dissipated energy, as shown in Figure 2.8, increases as a function of fatigue life and sharply inclines at the final failure stages, especially at higher stresses. Due to the large presence of the final-cycle damage, TDE is biased by the failure mode and the stress level which makes it hard to directly compare between R-ratios.

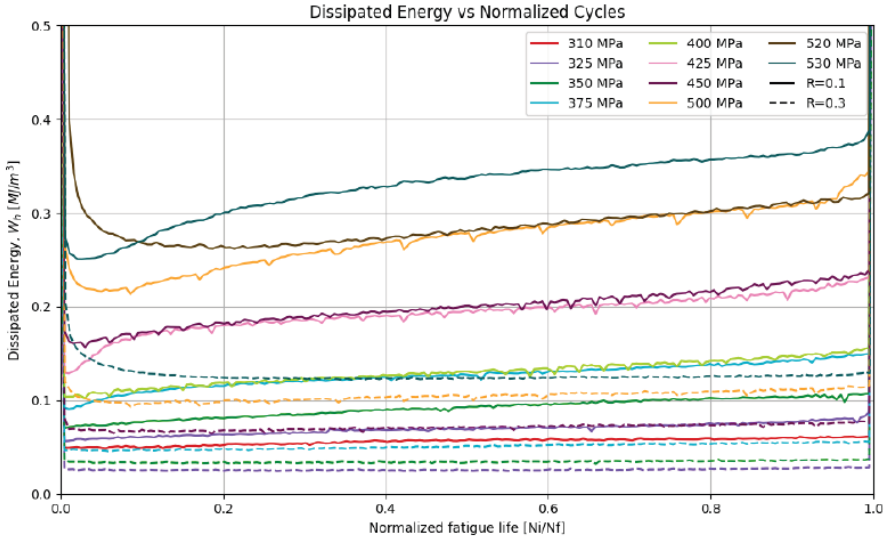


Figure 2.8: *Dissipated energy per cycle as a function of normalized fatigue life for the* $[0/90]_{4s}$ *UD E-glass/BT080-epoxy laminate, illustrating a predominantly stable plateau followed by a rapid increase near the end of life at* $N/N_f \approx 1$ *[1].*

Therefore, Krieg defined "Critical Dissipated Energy" (CDE) which is the accumulated hysteresis energy

rup to the onset of final failure - removing the non-comparability due to different failure modes and stress levels. This metric shows more meaningful and promising conclusions for fibre-dominated 0/90 laminates. The CDE vs. maximum cyclic stress trends, shown in Figure 2.9, collapse onto overlapping confidence intervals for the two stress ratios R=0.1 and R=0.3 - supporting that the CDE vs. stress level is approximately independent of R-ratio (as suggested by Movahedi-Rad et al. [11]).

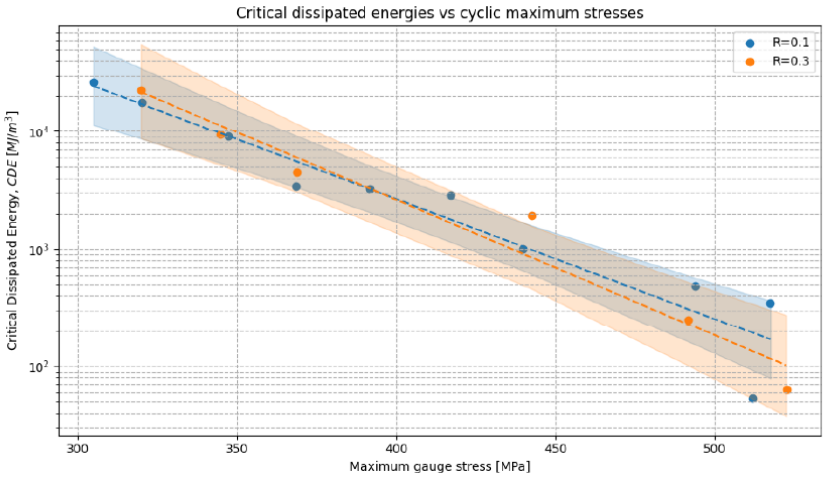


Figure 2.9: *Critical Dissipated Energy vs. Maximum Gauge stress for* $[0/90]_{4s}$ *UD E-glass/BT080-epoxy laminate [1]*

However, greater scatter is observed at the higher stress levels, which is plausible given the more severe evolution of dissipated energy and the increasing difficulty in defining the onset of final failure, particularly when multiple synergistic failure mechanisms interact and their sequence becomes less distinct. This raises the question of whether these very high-stress data points should be excluded from the analysis to better assess the validity of Movahedi-Rad et al.'s proposed relationship. Krieg discusses this directly in his thesis: the initial S–N curve prediction resulted in an RMSE of 0.51 decades, whereas excluding the two highest-stress data points, both with $N_f < 15$ cycles, reduced the prediction error substantially to 0.22 decades.

Applicability to Matrix-Dominated Composites

The dissipated energy per cycle as a function of normalized life for ±45° is shown in Figure 2.10.

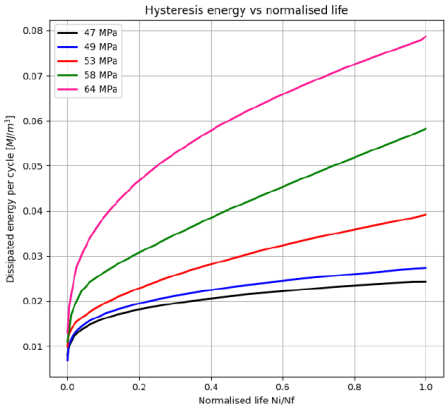


Figure 2.10: *Dissipated energy per cycle versus normalized fatigue life for the* ±45° *laminate, illustrating a predominantly monotonic increase throughout the fatigue life and no clearly defined final failure transition.[1]*

Contrary to 0/90 in Figure 2.8, the dissipated energy per cycle seems to monotonically increase along

the normalized life without a stabilization phase - especially for higher stresses. For the 0/90 laminates, the onset of failure point could be relatively easily deduced from TDE to result in CDE, however this seems to be more challenging for ±45° due to the onset of the final failure stage being considerably less distinct. This raises the question of how the onset of critical damage should be defined for ±45° laminates and, more importantly, whether the assumed R-ratio independence of dissipated energy trends with respect to stress level remains valid for matrix-dominated laminates.

Gap-03: Ambiguity in defining final-damage onset for CDE for ±45°.

- **Predictive Capability and R-ratio scaling.**

  The fatigue life prediction equation derived by Krieg was under the assumption that TDE vs. stress-level is independent of R-Ratio.

$$N_{f,R_2} = N_{f,R_1} \frac{\left(\frac{1-R_1}{1+R_1}\right)^2}{\left(\frac{1-R_2}{1+R_2}\right)^2} \frac{\left(1-R_1^2\right)|E^*|_{\text{avg},R_2} \sin\left(\phi_{\text{eff},R_1}\right)}{\left(1-R_2^2\right)|E^*|_{\text{avg},R_1} \sin\left(\phi_{\text{eff},R_1 2}\right)} \tag{2.10}$$

So, the predictive capability of the framework relies on this dependency. Utilizing the new CDE metric, the independence from R-ratio can be agreed upon.

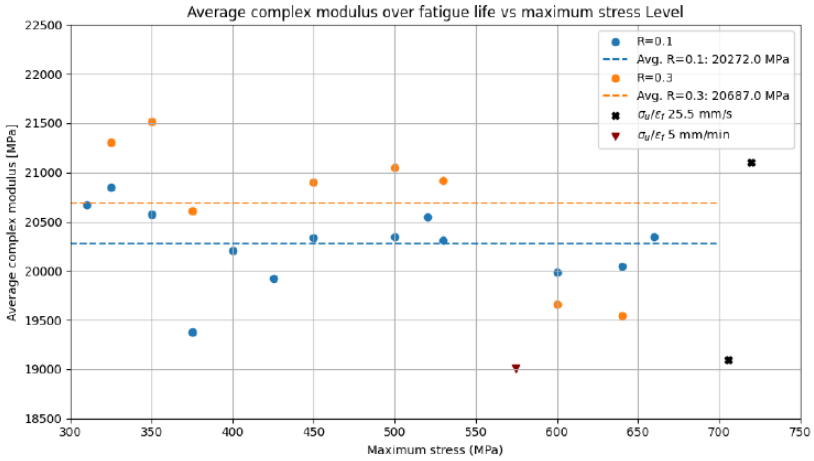


Figure 2.11: *Average Complex Modulus over fatigue life vs. maximum stress level for* $[0/90]_{4s}$ *UD E-glass/BT080-epoxy laminate [1]*

Given this, Figure 2.11 shows that the average complex moduli for both R=0.1 and R=0.3 differed merely by 1.4% in relation to the pristine high-rate tensile modulus suggesting that

$$\frac{|E^*|_{\text{avg},R_2}}{|E^*|_{\text{avg},R_1}} \approx 1. \tag{2.11}$$

In addition, Figure 2.5 shows independence of the effective loss factor for R=0.1 and R=0.3, resulting in

$$\frac{\sin(\phi_{\text{eff}})_{R_1}}{\sin(\phi_{\text{eff}})_{R_2}} \approx 1. \tag{2.12}$$

This results in Equation 2.13 being a fatigue life prediction equation that is purely an R-ratio scaling problem, allowing for predictions at untested R-ratios.

$$N_{f,R_2} = N_{f,R_1} \frac{\left(\frac{1-R_1}{1+R_1}\right)^2}{\left(\frac{1-R_2}{1+R_2}\right)^2} \left(\frac{1-R_1^2}{1-R_2^2}\right) \tag{2.13}$$

Using the S-N curve R=0.1 data as the input, the equation successfully predicted the S-N curve for R=0.3 within a root-mean-square error of around 0.22 decades, as can be seen in Figure 2.12.

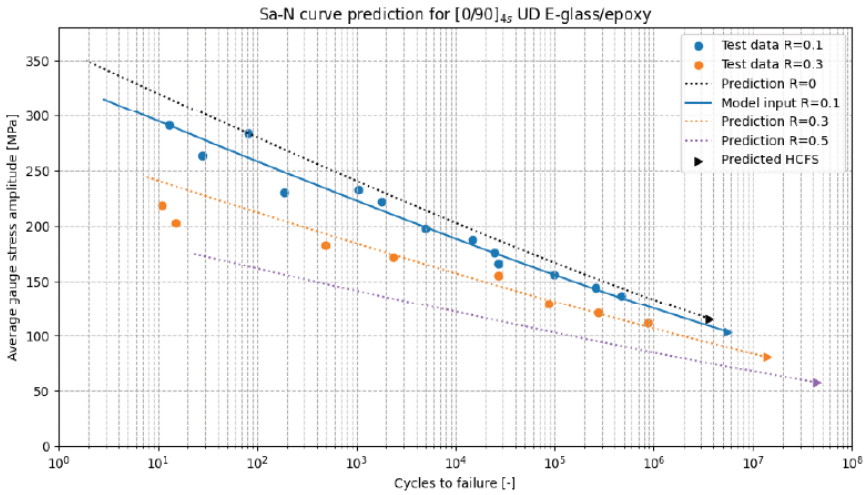


Figure 2.12: *S–N curves for the* $[0/90]_{4s}$ *UD E-glass/BT080-epoxy laminate, illustrating the good agreement between the predicted and experimental response at* $R = 0.3$*, achieved through the application of only the R-ratio scaling terms.[1]*

Applicability to Matrix-Dominated Composites

In order to apply the fatigue life prediction equation given in Equation 2.13, the relationship between total dissipated energy (TDE) and stress level must be either independent or only weakly dependent on the R-ratio. Currently, this assumption remains insufficiently verified. Further investigation into the nature of this dependence is therefore required, including whether an appropriate augmentation parameter could be introduced to account for any R-ratio effects and thereby extend the applicability of Equation 2.13.

Similarly, the assumption that the average complex modulus and effective loss factor remain approximately constant between different stress ratios necessitates further investigation. While this behaviour was observed for the tested fibre-dominated 0/90 laminates, it is unclear whether it would persist at higher R-ratios approaching 1.0, where the governing failure mechanisms may differ, and this uncertainty is expected to be even more pronounced for matrix-dominated laminates.

Gap-04: Uncertainty in the R-ratio dependence of fatigue-life model parameters, for ±45°.

2.3. The challenge of Matrix-Dominated Composites

Krieg's modified linear viscoelastic framework was developed and validated primarily for fibre-dominated behaviour. Its extension to ±45° warrants examining whether the underlying modeling assumptions remain valid when the response becomes strongly matrix-dominated. This section therefore establishes the material-specific mechanisms that may limit the direct applicability of Krieg's framework.

Subsection 2.3.1 discusses the mechanical behavior of the material, and concepts unique to it such as creep phenomena, ratcheting and the vulnerability to temperature. With this context established, Subsection 2.3.2 lists the main assumptions taken in Krieg's framework that may not cleanly comply for ±45°, and the reasons behind it.

2.3.1. Nature of ±45° Laminates

Fibre-reinforced composite materials subjected to cyclic loading undergo severe degradation, and even enhancement, of the material properties throughout their fatigue life. This is a result of the internal damage mechanisms such as fiber breakage, matrix cracking, debonding, transverse-ply cracking, and delamination which act separately and synergistically. Due to the different constituents in the composite, unlike metals, it

is difficult to accurately predict the damage progression. However a generalized failure process for unidirectional, cross-ply and angle-ply laminates has been identified, which follows a three-stage process.

- **Stage I:** Initiation of micro-cracks within the matrix.
- **Stage II:** Crack propagation, eventually reaching the matrix-fibre interface, and leading to debondings and delaminations.
- **Stage III:** Once fully reaching the fibre, it leads to fibre-breakage and thereafter, declared as failed.

Due to the presence of the matrix, a viscoelastic constituent, fatigue is not a pure cyclic-dependent phenomena but is also time-dependent, where concepts of creep, relaxation and recovery are non-negligible. The relationship between stress and strain for viscoelastic materials is time-dependent, and additionally load-dependent under nonlinear behavior [23]. Krieg [1] modifies a linear viscoelastic theory; however, it remains a question whether a nonlinear formulation would offer improved predictive capability for matrix-dominated composites. There are three ways nonlinearities exist: material, geometry and interaction [23]. Figure 2.13 shows the generalized stress-strain curves for different conditions.

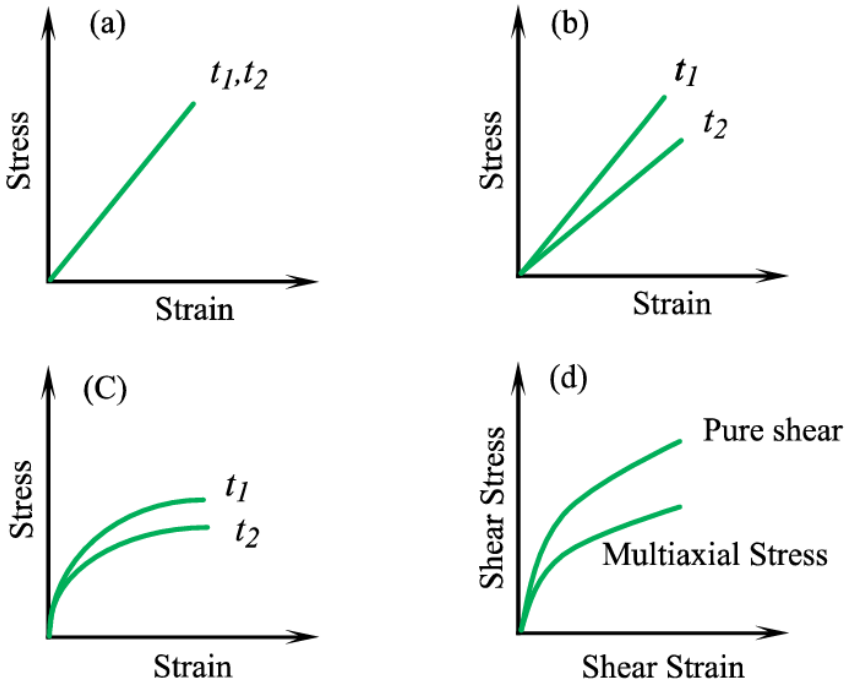


Figure 2.13: *Generalized stress-strain curves for (a) linear elastic, (b) linear viscoelastic, (c) material nonlinearity, (d) interactional nonlinearity [23]*

The definitions and relevance of creep, relaxation and recovery are discussed below.

- **Creep**

  Creep is defined as the time-dependent increase in strain as the material is subjected to a constant stress over time. In pure creep studies, the key design parameter is the time of rupture as a function of applied stress and temperature. Under cyclic loading, however, this distinction becomes less clear, giving rise to the debate over whether fatigue life should be characterized in terms of elapsed time or number of cycles. Physically when a material is subjected to creep, as time elapses, the molecular chains inside the polymer matrix start to gradually untangle and slide past each other. There are three stages of creep; 1) sudden deformation that slows down (strain-hardening), 2) a steady stage of deformation and 3) rapid acceleration of deformation leading to rupture. This is shown in Figure 2.14.

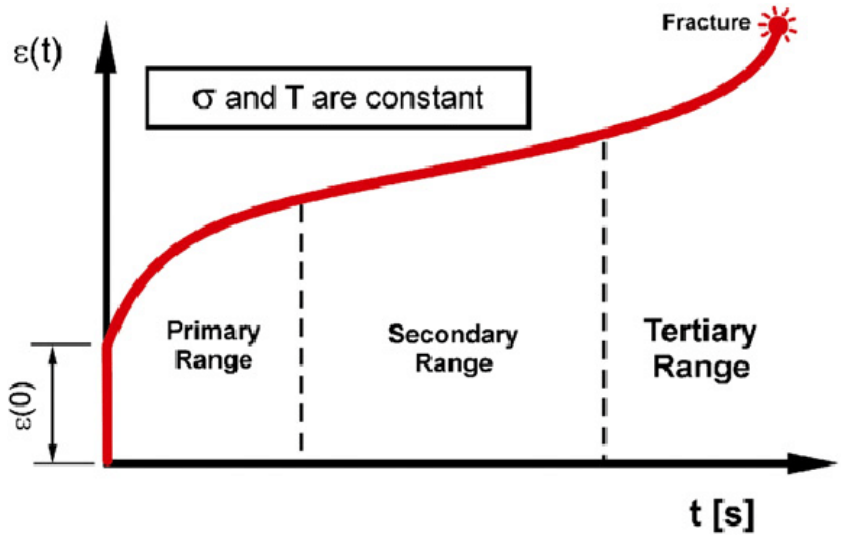


Figure 2.14: *Three-stage creep phenomena [24]*

Creep is a phenomenon that is challenging to isolate and is significantly non-negligible for matrix-dominated composites subjected to cyclic loading. Under load-controlled fatigue testing, the material is essentially subjected to interrupted creep. Due to the viscoelastic nature, the strain is not fully regained during the unloading stage. This strain accumulates each cycle, and is a phenomenon called **cyclic creep** or **ratcheting** [25]. For matrix-dominated composites, this accumulation of strain can be larger than the failure strain even if the applied stress is well below the static strength.

One of the driving parameters for cyclic creep is the mean stress. It can be visualized as the somewhat 'constant' load that is constantly pulling on the material, while the amplitude stress is wiggling it back and forth helping the polymer chains untangle. At zero mean stress, the ratcheting is minimized (approximately zero) as the tension creep and compression creep cancel out, assuming the material has parallel behavior for tension and compression - which is usually not the case for composites. As the mean stress increases, ratcheting becomes faster. One of the main accelerators of ratcheting, contributing to this 'snowball effect' is the self-heating. The viscous component of the matrix causes larger hysteresis loops which leads to more heat generated, thereby softening the matrix further, and as temperature reaches the glass transition temperature, creep accelerates - and the cycle repeats.

- **Relaxation**

  Relaxation is defined as the time-dependent decrease in stress required to maintain a constant strain subjected to the material. If the polymer is stretched and held in one place, the internal molecular chains rearrange to a lower energy, relieving the stress without shape changes.

  Stress relaxation is a governing mechanism if the cyclic loading is applied in a displacement-controlled manner. Contrary to creep, cyclic relaxation could extend the fatigue life. Ellyin et al. [25] states that for deformation-controlled cases, the damage development could be decreased due to stress relaxation. As this thesis aims to focus on load-controlled cases, stress relaxation is of limited relevance and is therefore not discussed in detail.

- **Recovery**

  Recovery is defined as the time-dependent reduction in the strain once the stress is removed. This is a complementary phenomenon, alongside creep, consisting of two components; instantaneous elastic recovery - the spring-back - and delayed viscoelastic recovery - as the polymer chains recoil and gradually return to the shape. For most composites, the deformation does not fully recover due to plastic damage or friction.

  Creep and recovery are intrinsically linked. A schematic diagram of a creep-recovery test can be seen in Figure 2.15. The concept of recovery becomes more important for nonlinear cases where the stress-dependent terms can be extracted from recovery tests [26].

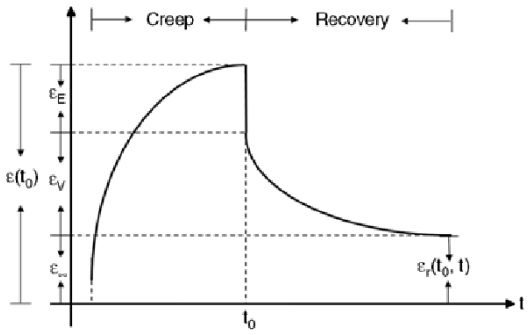


Figure 2.15: *Schematic diagram of a creep-recovery test [27]*

While time-dependent phenomena can be characterized independently, the primary challenge lies in understanding their interaction with cyclic-dependent effects, the relative influence of which depends on the loading spectrum and material type. The interaction between creep and fatigue is regarded as complex, difficult to separate, and definitely cannot be overlooked. Reifsnider [28] comments that one must be careful to not fully detach time-dependent characteristics for such analysis. Vassilopoulos [29] presents a comprehensive overview of the mechanical behavior of ±45° glass/epoxy composites subjected to different loading profiles, forming the basis of this chapter. For each loading profile, the variation in structural changes are explored, along with their effects on mechanical, thermal and optical behaviour.

Short Tests

Although this thesis focuses on fatigue behaviour, attention is also given to understanding the material behavior under short-term tests and how it contrasts with long-term fatigue tests. As demonstrated in Krieg's thesis [1], short-term characterization methods such as DMA can provide valuable insight for fatigue life prediction, motivating the exploration of similar physics-based shortcuts in the present work on ±45° laminates.

- **Dynamic Mechanical Analysis (DMA)**

  DMA is a characterization method that has roots in rheology - the study of viscoelastic properties. DMA relies on the application of a sinusoidal stress (or strain) to a material, and the reaction is measured. Figure 2.16 shows this difference in the applied sinusoidal stress curve and the output strain curve for ideal elastic, viscoelastic and ideal viscous materials [30].

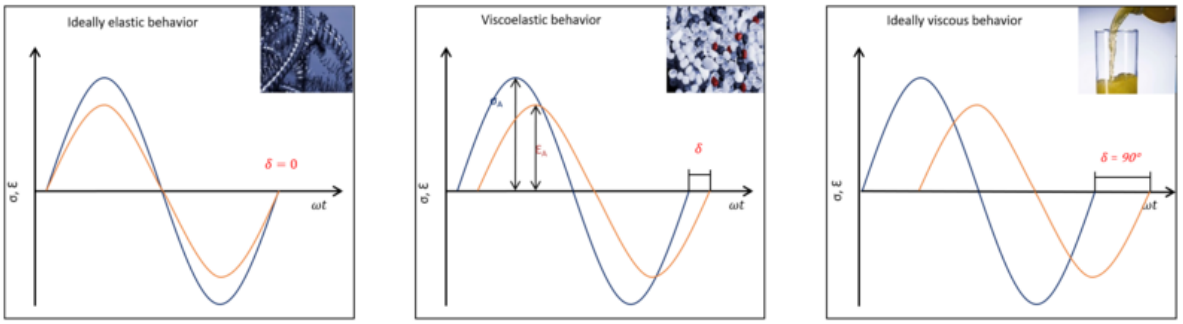


Figure 2.16: *Generalized material responses for ideal elastic, viscoelastic and ideal viscous materials [30]*

For the composite matrix, due to its inherent viscoelastic nature, the strain is time-dependent and it lags behind the stress. This phase lag allows the machine to quantify the material's resistance. The main outputs are: Storage Modulus (E'), Loss Modulus (E'') and the damping ratio $\tan\delta = E''/E'$. The general stiffness quantity is denoted as the complex modulus $E^* = \frac{E''}{E'}$, where the 'star' exponent indicates it is a dynamic stiffness value.

With the use of an environmental test chamber, sweep tests can be done with DMA. Sweep tests are performed by applying a small oscillatory stress/strain and systematically sweeping one variable; these can be amplitude, frequency, temperature, humidity and time [30]. There are different methods as to how the sinusoidal waveform is applied: tension, bending, torsion/shear or compression.

The outputs from the DMA can be used to extract useful information about the material. In the case of ±45° laminates, several authors have performed DMA tests to obtain the glass transition temperature T_g. Vassipolous [29] acquired the T_g by plotting the evolution of the storage modulus against temperature, shown in Figure 2.17.

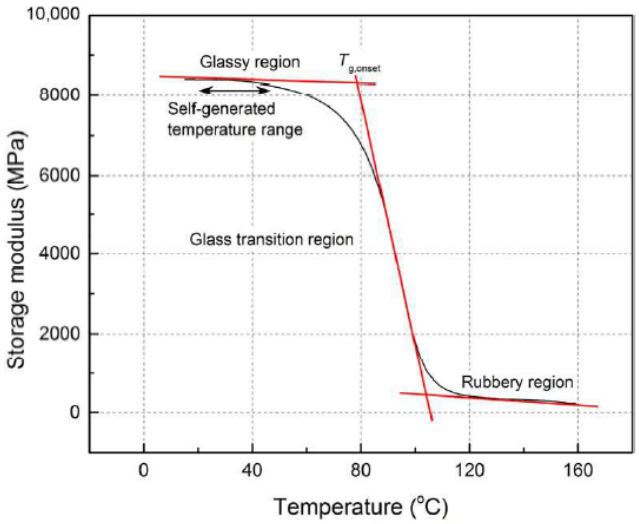


Figure 2.17: *Determination of T_g on a E′ vs. T graph for ±45° glass/epoxy [29]*

It shows a clear transition regime from glassy to rubbery, where the regime ranges from 70° to 100° Celsius. The onset of the glass transition temperature is denoted as 80°. Karvanis et al. [31] plotted the storage modulus, loss modulus and the loss factor as a function of temperature. Figure 2.18 presents Karvanis et al.'s storage modulus as a function of temperature [31] - showcasing a transition range from 90° to 120°, when analyzed similarly to Vassipolous [29].

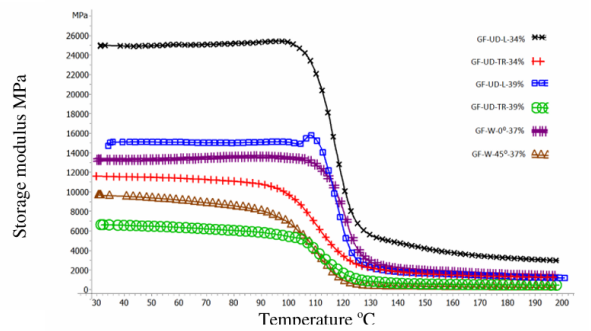


Figure 2.18: *Storage Modulus vs. Temperature [31]*

As Karvanis et al. [31] mention, the determination of the T_g is a well-known point of debate for scientists. Karvanis et al. [31] acquires the glass transition temperature from the peak from loss modulus vs. temperature and loss factor vs. temperature graphs - shown in Figure 2.19 and Figure 2.20. This gives an onset of transition at 110° and 120°

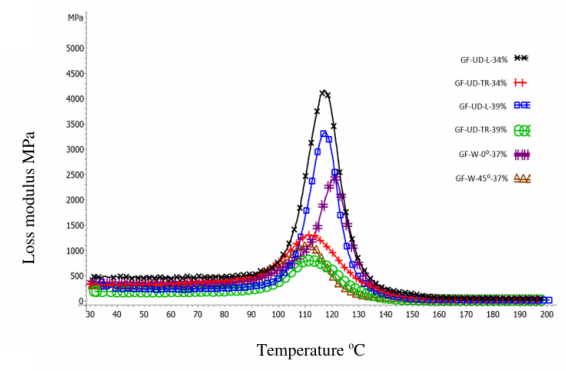


Figure 2.19: *Loss Modulus vs. Temperature [31]*

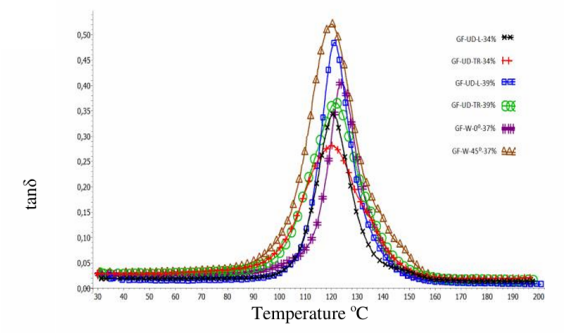


Figure 2.20: *Loss Factor vs. Temperature [31]*

The discrepancies between the two studies arise from differences in resin systems, curing procedures, experimental configurations, and fibre architecture. Specifically, Karvanis et al. [31] utilized a three-point bending setup, while Vassilopoulos [29] employed a single-cantilever configuration, and the materials differed in laminate architecture (UD versus woven). If these variables are controlled, the results may be considered repeatable. In the context of fatigue, the primary relevance lies in assessing how closely self-heating temperatures approach the glass transition temperature, beyond which the polymer transitions from a glassy to a rubbery state, fundamentally altering its mechanical response.

Esse et al. [32] perform Dynamic Mechanical *Thermal* Analysis (DMTA) which is DMA but highlighting the temperature sweep conducted. This paper highlights the work of Miyano et al. [33] who developed fatigue-life prediction model that relies on trading time for temperature - in other words, testing at high temperatures can be mathematically shifted to predict failure at low temperatures under viscoelastic failure. This only holds for thermorheologically simple materials meaning that the failure mechanism does not change but simply accelerates in speed. Esse et al. [32] used a graph of loss vs. storage modulus to show that GFRP $\pm 45^{\circ}$ is indeed thermoheologically simple under DMA testing. The paper shows differences in the DMA outcomes for neat epoxy versus the GFRP, due to the presence of fibers physically slowing down the relaxation of the matrix.

As previously mentioned in Subsection 2.2.2, Lennart Krieg's thesis relies heavily on DMA as he uses the loss factors derived from this as "pristine" viscoelastic properties of the material before damage. As the effective loss factors derived from fatigue test data are plotted against the stress level, the intersection between the pristine loss factor and the power-law trendline of these points results in the HCFS.

- **Monotonic Tensile Tests**

  Vassipolous [29] reports monotonic tensile tests at quasi-static rates of 1mm/min and 30.5kN/s as displacement control and load controlled tests, respectively. Figure 2.21 shows the rate-dependent nonlinear stress-strain curves.

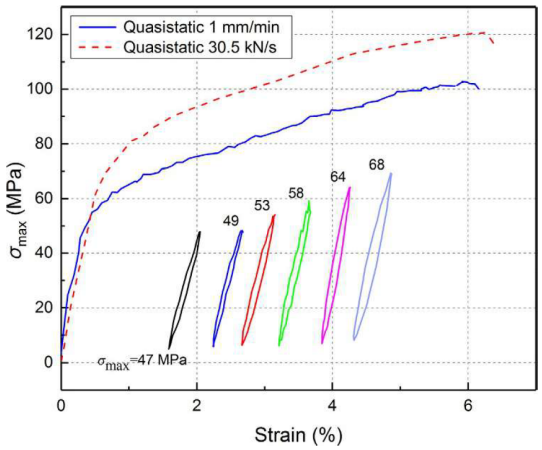


Figure 2.21: *Quasi-static stress-strain curves for GFRP ±45° laminates [34] [29]*

Compared to 1mm/min, the loading rate at 30.5kN/s yielded higher yield and ultimate strength. This sets the starting point for a discussion on the influence of loading parameters, such as frequency, loading rate, strain rate and time at peak load, on the material response. This is attributed to the viscoelastic nature of the material, an effect that is expected to be particularly pronounced and intertwined for ±45° laminates. This interplay is expected to be equally, if not more, significant under fatigue loading and will therefore be revisited during the experimental design phase, where the primary research questions will guide the prioritization and isolation of loading parameters for fatigue validation.

Ellyin et al. [25] perform tensile loading tests on ±45° laminates at different strain rates: ranging from $10^{-6}/s$ to $10^{-3}/s$. Figure 2.22 shows the influence of the strain-rate on the stress-strain curves, where the biggest influence is seen in the decreasing tangent modulus of the curve at higher stress levels.

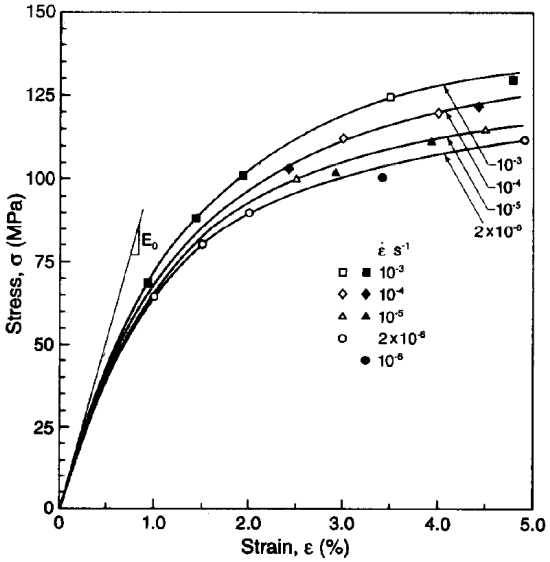


Figure 2.22: *Influence of strain rate on the stress-strain curves of GFRP ±45°, illustrating the increase in the tangent stiffness with increasing strain rate. [25]*

In comparison to other stacking configurations like multidirectional $[\pm 45°, 0°]_s$ and/or off-axis UD 45°, angle-ply ±45° showcases the most ductile curves - resulting in much greater strain at failure values. The nonlinear curves showcase the absence of a clear elastic-plastic transition. In addition, at higher strain levels, the fibre reorientation towards the loading direction contributes to an apparent rise in the stiffness, which superimposes with the ongoing matrix-dominated damage processes.

- **Pure Creep**

  Movahedi-Rad et al. [35] (reported by Vassipolous [29]) tested six GFRP ±45° laminates under pure creep at different constant stress levels; 48.6, 58.2, 58.2, 64.2, 68.0 and 70.0. Thereafter, the strain response as a function of time was plotted and can be seen in Figure 2.23.

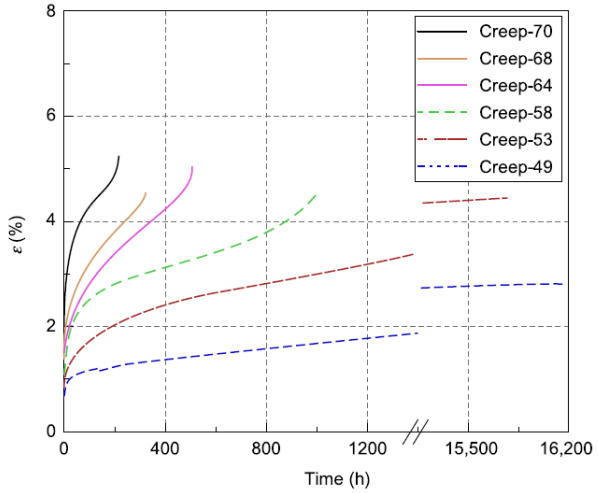


Figure 2.23: *Creep curves at different stress levels for GFRP ±45° [29]*

The creep strain follows three stages as previously mentioned. The elastic strain and the creep rate increase proportionally to the stress but the failure strain does not differ much. Vassipolous also monitored the translucency where he saw that up until secondary stage, there was no damage - seen in Figure 2.24.

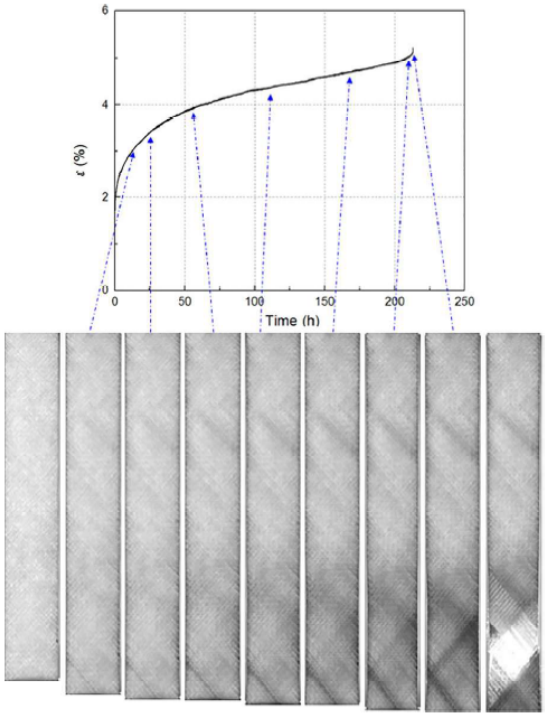


Figure 2.24: *The corresponding light transmittance at different stages of creep for 70MPa stress level [29]*

Note that Vassipolous [29] focuses on the mechanical characterization and failure analysis of these GFRP ±45° laminates under pure creep at relatively high stress levels. At these stress levels, the material

exhibits nonlinear behavior and has exceeded the linear viscoelastic regions. A common use of creep tests is the use of Time-Temperature Superposition (TTSP) to construct a master curve and predict time of rupture, yet at high stress levels, the material is damaged and is not thermohereologically simple which means no use of TTSP.

In contrast, Xu et al. [36] explores the creep behavior of Flax-fibre-reinforced polymers, but under the same stacking sequence of ±45°. Unlike Vassipolous [29], who uses dead weight and waits the entire duration till rupture, Xu et al. [36] trades temperature for time and creates a master curve. For the construction of the master curve, unlike 0° laminates, which require horizontal and vertical shifting, ±45° only needs horizontal shifting. However, this could only be the case for stresses low enough such that linear viscoelastic theory can be used.

All in all, the short-term characterization emphasizes the significant viscoelastic sensitivity of the ±45° laminate. While these tests define some static failure envelopes and time-dependent compliance, they do not fully capture the cumulative damage mechanisms encountered when subjected to cyclic loading. Consequently, the following section extends the discussion into the long-term tests.

Fatigue Tests: Constant Amplitude, interrupted and creep-fatigue loading patterns

Vassipolous [29] reports the results of fatigue experiments at constant amplitude, interrupted and creep-fatigue loading profiles at a stress ratio of R=0.1, in a constant temperature of 20°. All the specimens were loaded at a loading rate of 30.5kN/s, which was derived to avoid excessive self-heating. The applied interrupted fatigue loading profile shows a sinusoidal waveform, followed by a two-hour recovery period -at zero stress, while the creep-fatigue loading profile shows the same sinusoidal waveform, but followed up with a 2 h or 48 h creep period - at a maximum cyclic stress level. This can be visualized in Figure 2.25.

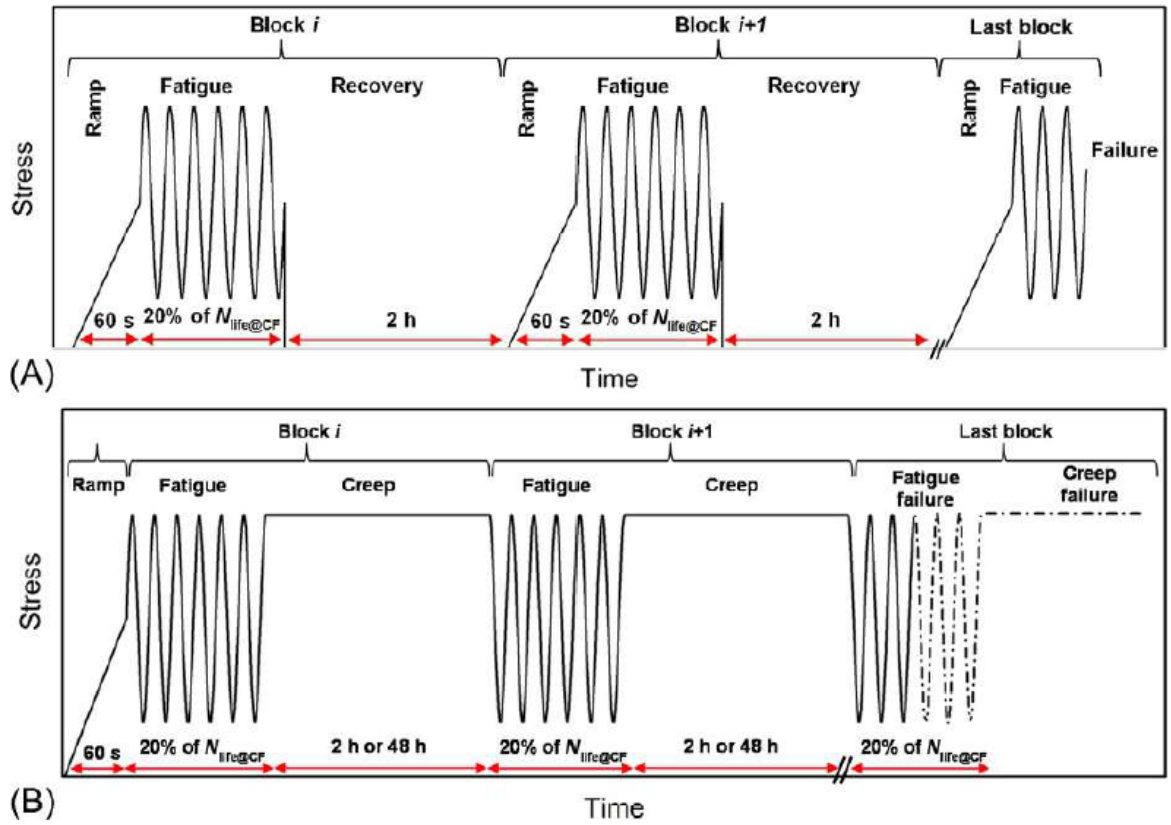


Figure 2.25: *Interrupted (A) and creep-fatigue (B) loading patterns*

In order to capture the full range of fatigue responses under these loading patterns, different instrumentation was used to monitor the mechanical, thermal and optical changes. A video-extensometer was used to capture the variation of strain. The surface temperature was monitored with an infrared thermal camera, and finally, to detect the optical responses, photographs of the translucent specimens were taken at regular points during the fatigue life.

- **Fatigue life**

  Figure 2.26 shows the S-N curves for the different loading patterns; Conf shows the constant amplitude loading, Cref is the creep-fatigue interaction where 2h or 48h denotes the amount of creep time in between sinusoidal loading blocks and Intf is the interrupted loading pattern.

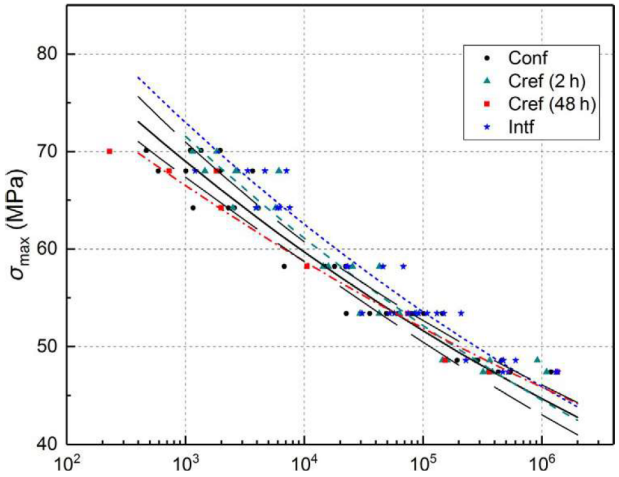


Figure 2.26: *S–N curves for the different loading patterns, illustrating the influence of creep and interrupted loading on fatigue life. Conf denotes constant-amplitude fatigue loading, Cref (2 h) and Cref (48 h) denote creep–fatigue loading with 2 h and 48 h creep periods inserted between fatigue loading blocks, respectively, and Intf denotes the interrupted-fatigue loading pattern. [29]*

The creep-fatigue loading for 48hrs seems to have the most shallow slope while the interrupted loading shows the highest slope. At higher stresses such as 70MPa, the influence of creep caused a smaller number of cycles while at lower stresses, the influence of creep was not as significant. For the interrupted loading pattern, the recovery period recovers some strain of the viscoelastic matrix allowing for a higher number of cycles to failure at higher stresses.

Ellyin et al. [25] investigated the S-N curve changes as the frequency changes. Figure 2.27 shows two S-N curves for frequencies 3.6 Hz and 0.417 Hz.

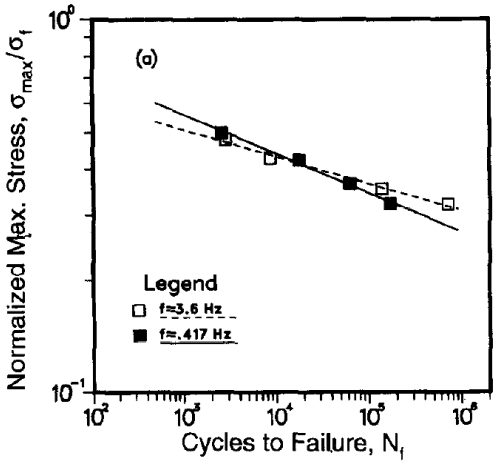


Figure 2.27: *S–N curves for loading frequencies of 3.6 Hz and 0.417 Hz, illustrating the frequency-dependent fatigue response and the cross-over in fatigue life between the two loading frequencies [25].*

Figure 2.27 shows a "cross-over" point separating into two distinct behavioral regimes. Stress levels - below this point - have decreasing fatigue life as the frequency is reduced suggesting the time-dependent creep-driven damage dominates in this regime. For stresses above this point, the fatigue life decreases with increasing frequency suggesting the influence of self-heating.

- **Stiffness degradation, energy dissipation and cyclic creep**

Figure 2.28, Figure 2.29 and Figure 2.30 show the cyclic stress-strain curves for continuous, interrupted and creep-fatigue loading patterns, respectively.

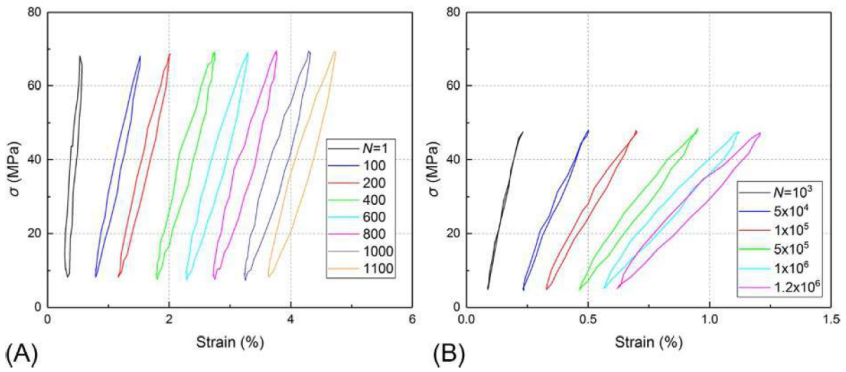


Figure 2.28: *Hysteresis loop evolution for (A) 68 MPa and (B) 47 MPa [29]*

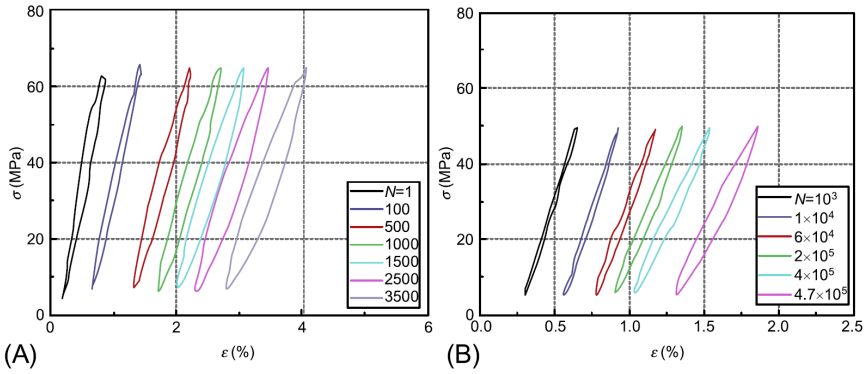


Figure 2.29: *Hysteresis loop evolution for (A) 64 MPa and (B) 49 MPa [29]*

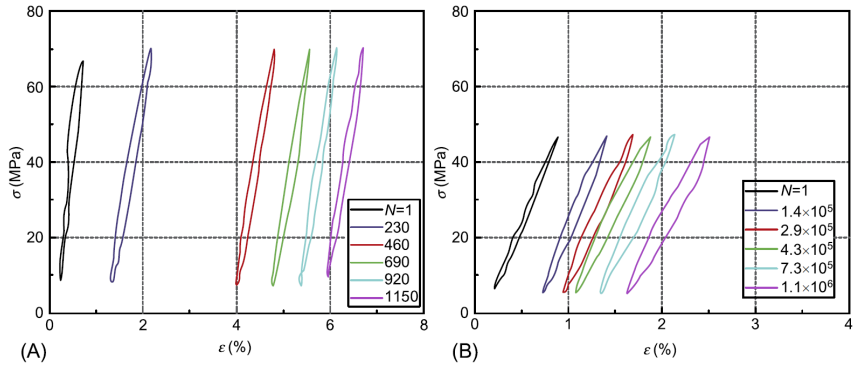


Figure 2.30: *Hysteresis loop evolution for (A) 70 MPa and (B) 47 MPa [29]*

Continuous cyclic loading, in Figure 2.28, show progressive loop widening and gradual stiffness loss and for interrupted loading, in Figure 2.29, there is strain recovery due to the recovery period which is visualized in a backward shift of the next hysteresis loop, but no recovery of the stiffness loss - no slope changes. This can be seen in Figure 2.31. This separates the reversible viscoelastic effects from irreversible damage effects.

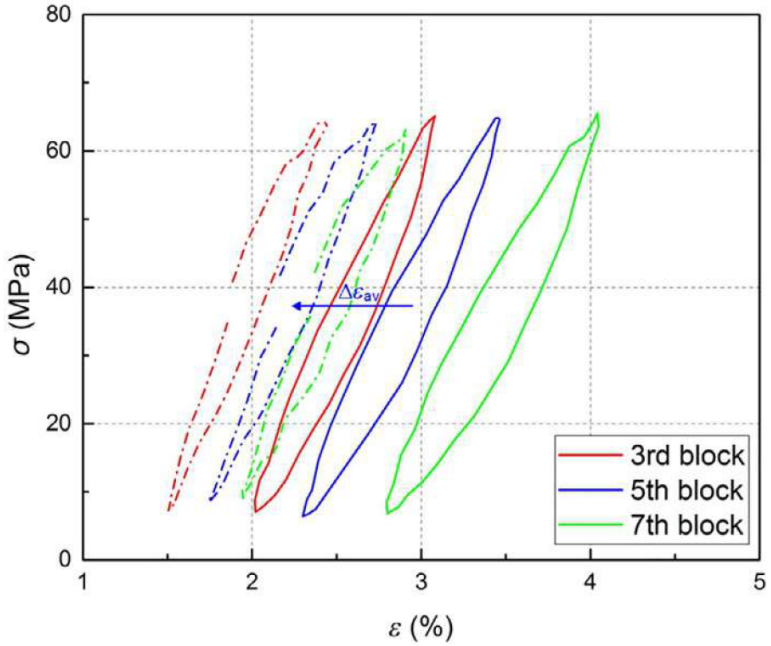


Figure 2.31: *Back shift of hysteresis loops [29]*

Figure 2.32, Figure 2.33 and Figure 2.34 shows the degradation of stiffness as a function of normalized life for continuous, interrupted and creep-fatigue loading patterns, respectively.

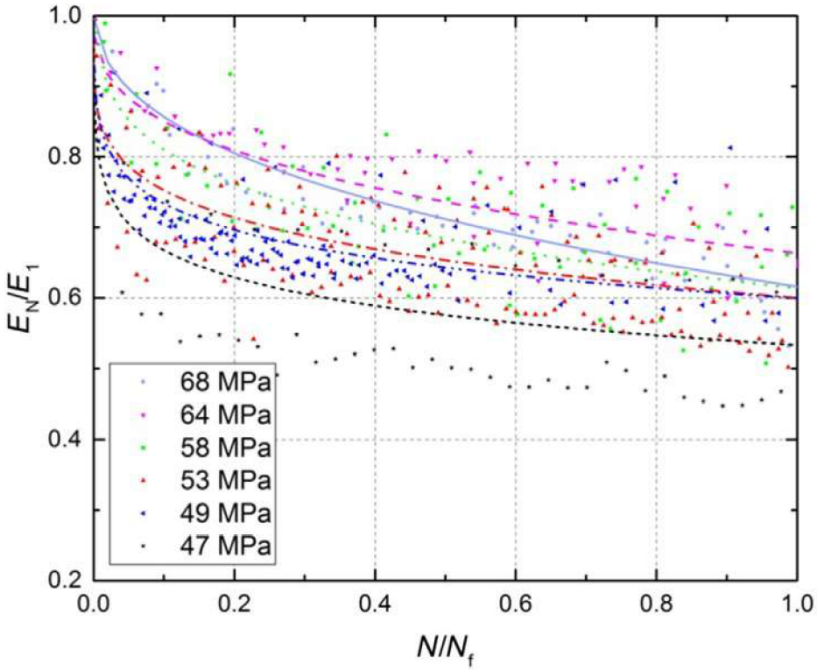


Figure 2.32: *Normalized fatigue stiffness vs. cycles to failure for continuous fatigue loading pattern [29]*

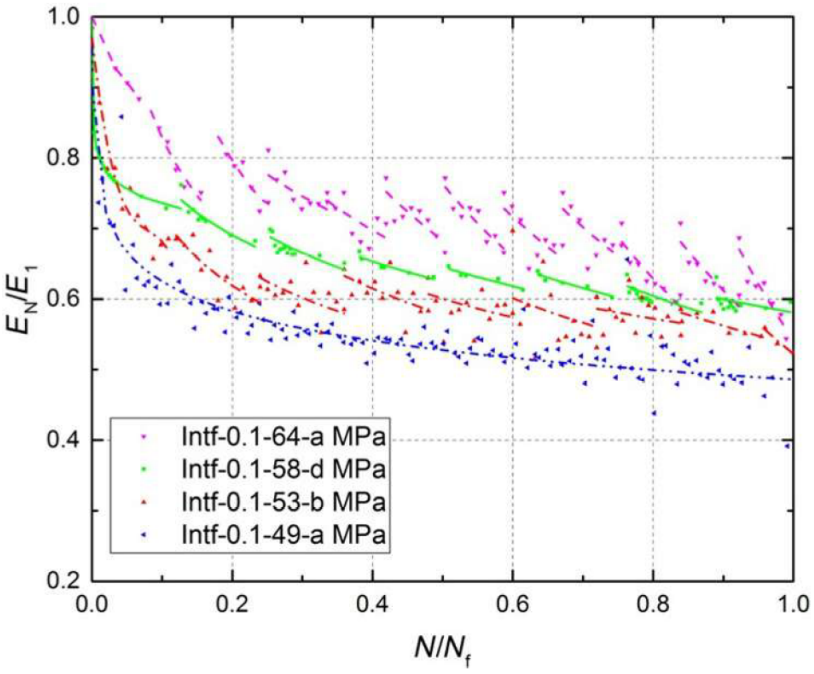


Figure 2.33: *Normalized fatigue stiffness, E_N/E_1, versus normalized fatigue life, N/N_f, for the interrupted-fatigue (Intf) loading pattern. In the legend, "Intf" denotes interrupted-fatigue loading, 0.1 denotes the stress ratio $R = 0.1$, the values 49, 53, 58, and 64 indicate the applied maximum stress in MPa, and the final letters identify the individual specimens [29]*

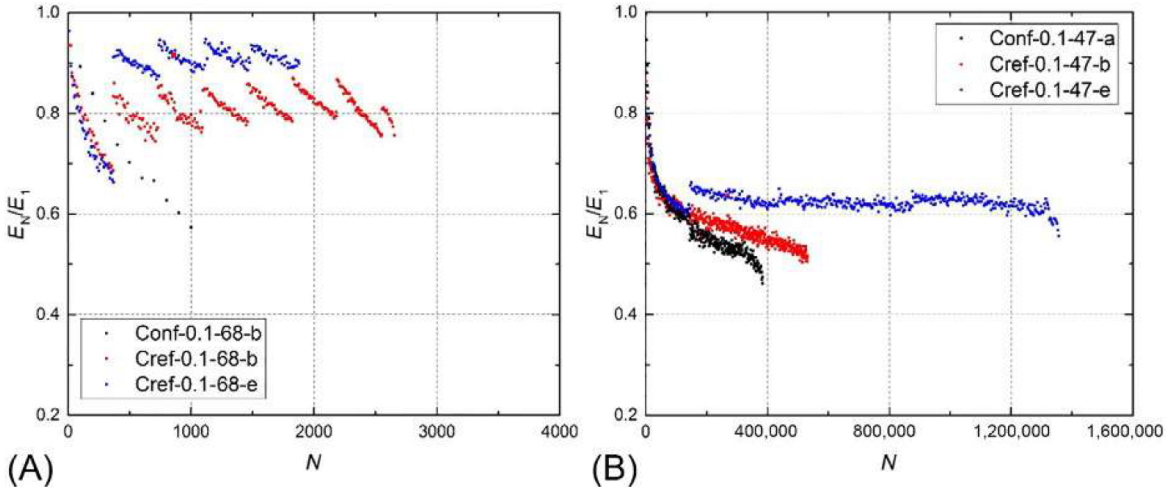


Figure 2.34: *Normalized fatigue stiffness, E_N/E_1, versus number of cycles, N, for constant-amplitude fatigue (Conf) and creep–fatigue (Cref) loading. In the legend, "Conf" denotes constant-amplitude fatigue loading and "Cref" denotes creep–fatigue loading; 0.1 denotes the stress ratio $R = 0.1$, 68 and 47 indicate the applied maximum stress in MPa, and the final letters identify individual specimens. (A) Results at 68 MPa; (B) results at 47 MPa [29]*

When the stiffness is normalized by the first cycle stiffness and plotted against the normalized fatigue life, all specimens show the same degradation shape regardless of stress level or loading pattern - implying that the damage accumulation governs stiffness evolution. The stress level controls the magnitude in degradation - not the trend. Lower stress levels lead to greater total stiffness loss and higher stresses cause faster stiffness loss but less total damage volume. Figure 2.33 shows the influence of the interruption, the partial recovery which decreases at lower stress levels - relating to the viscoelastic recovery and not damage healing. Figure 2.34 shows the creep-fatigue loading; temporary stiffness recovery after in-

terruptions, accelerated damage growth at high stress and, generally, a shorter fatigue life compared to continuous fatigue. While stiffness degradation provides a clear and robust indicator of damage evolution, it does not readily distinguish between cyclic-dependent and time-dependent contributions to the overall response. As noted by Krieg [1], alternative metrics such as the damping or loss factor offer potential advantages.

Ellyin et al. [25] also present the normalized stiffness as a function of the normalized number of cycles in Figure 2.35.

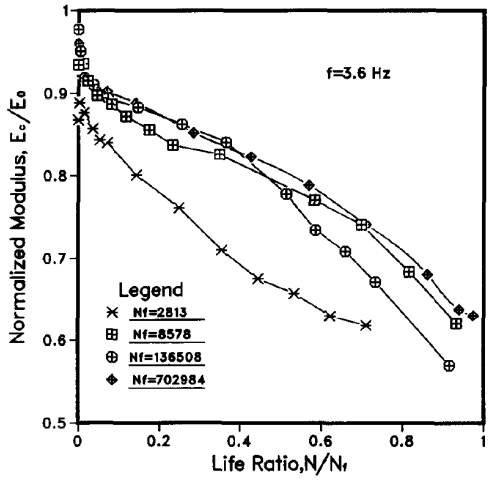


Figure 2.35: *Normalized Stiffness vs. Normalised Life [25]*

The difference between Figure 2.32 and Figure 2.35 may be due to the different loading parameter, where Ellyin et al. load at a constant frequency of 3.6 Hz while Vassipolous loads at a constant load rate of 30.5 kN/s. For higher stresses, the load rate and the frequency is somewhat similar, and consequently, showing a similar degradation trend even though it is steeper and rapidly degrading for Figure 2.35.

Ellyin et al. [25] also monitors the shift of the hysteresis loop, creep strain, as a function of the normalized life. Figure 2.36 shows its rate as a function of the elapsed life for different stress levels, at two different frequencies.

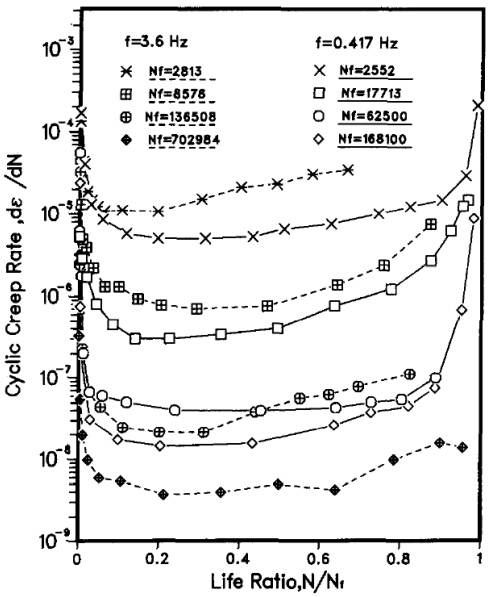


Figure 2.36: *Cyclic creep rate vs. Normalized life [25]*

It can be seen that for higher stresses, the lower frequency shows a generally lower cyclic creep rate but vice-versa for lower stresses, which suggests this "cross-over" point between the two regimes. Consequently, Ellyin et al. [25] compares the stress level vs. cyclic creep rate against the stress level vs. total cycles to failure, shown in Figure 2.37.

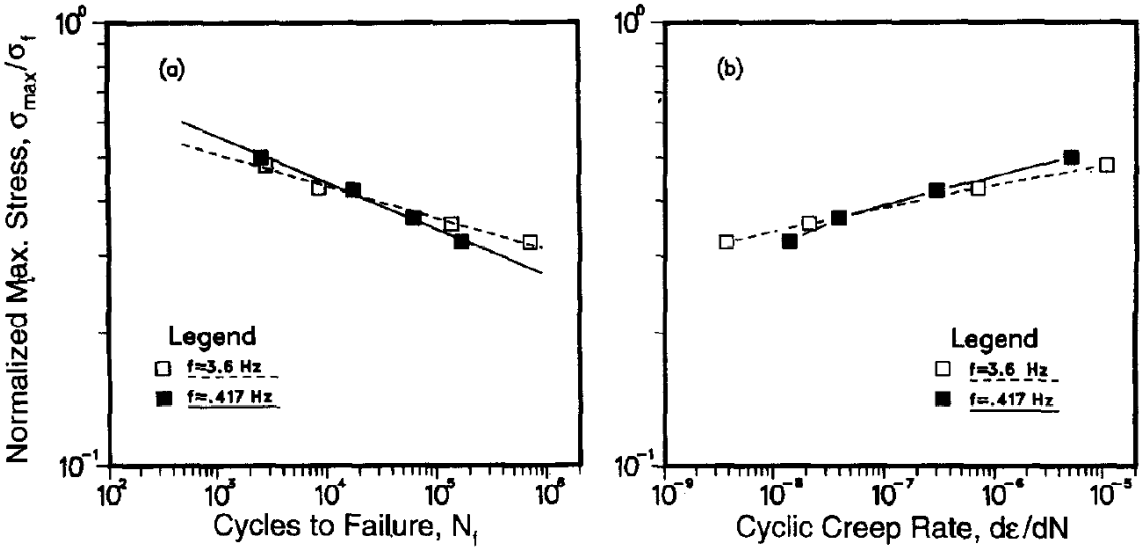


Figure 2.37: *Normalized maximum stress vs. (a) cycles to failure, (b) steady rate of cyclic creep [25]*

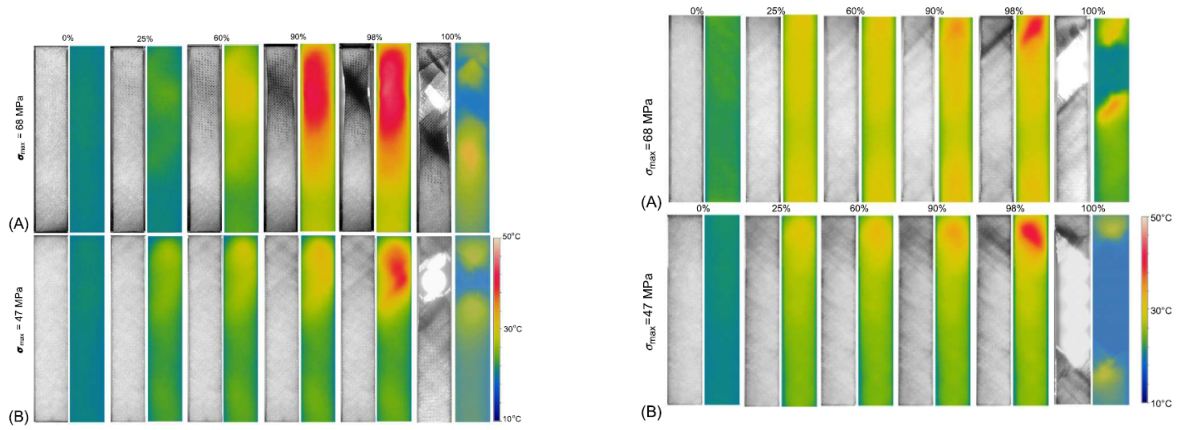
It can be seen that the cross-over point for both plots occurs at similar stress levels providing a strong correlation demonstrating in which Ellyin et al. states "that the frequency effect on the fatigue behavior is a function of the cyclic creep"[25].

- **Thermal and optical behaviour**

  Vassipolous [29] visualized the damage using light transmittance where the darker regions corresponded to higher local damage. They noted that the damage usually develops along the fibre direction, where at higher stress levels, it shows more localized damage that leads to earlier failure while for lower stress levels, the damage is more uniformly distributed.

  Similarly, the self-heating of the specimen can be tracked with the IR camera. Self-heating is significant for ±45° [37]. Early in the fatigue life, the temperature is distributed uniformly and as life progresses, the temperature fields become non-uniform leading to localized hot-spots that generally aligned with the fibre direction. For interrupted loading, the damage and temperature distributions remain relatively uniform throughout most of the life. Load interruptions promote crack blunting in the viscoelastic matrix which delays crack initiation and growth, leading to a longer life. During creep-fatigue loading, at high stress and long hold times, the damage localizes more rapidly and there are temperature spikes near failure. In addition, the fatigue life is shortened due to creep-assisted damage growth. At lower stresses, the damage and temperature remain broadly distributed and failure occurs later.

  The damage and temperature changes as cycles elapse are shown in Figure 2.38a, Figure 2.38b, Figure 2.39 for continuous, interrupted, creep-fatigue loading patterns, respectively.



(a) *Continuous fatigue loading* **(b)** *Interrupted fatigue loading*

Figure 2.38: *Thermal and optical damage evolution under different fatigue loading conditions [29].*

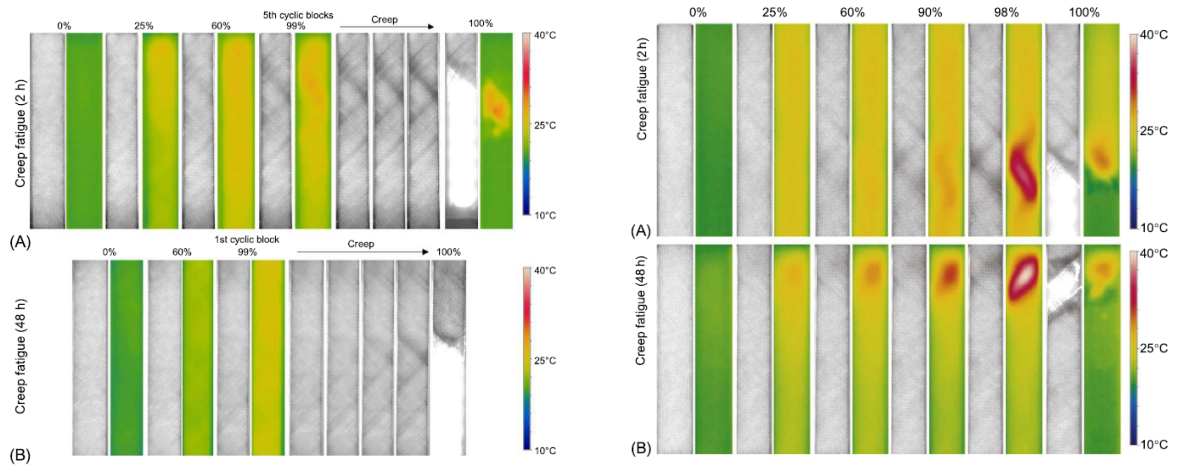


Figure 2.39: *Thermal and optical damage evolution under different creep-fatigue loading patterns [29].*

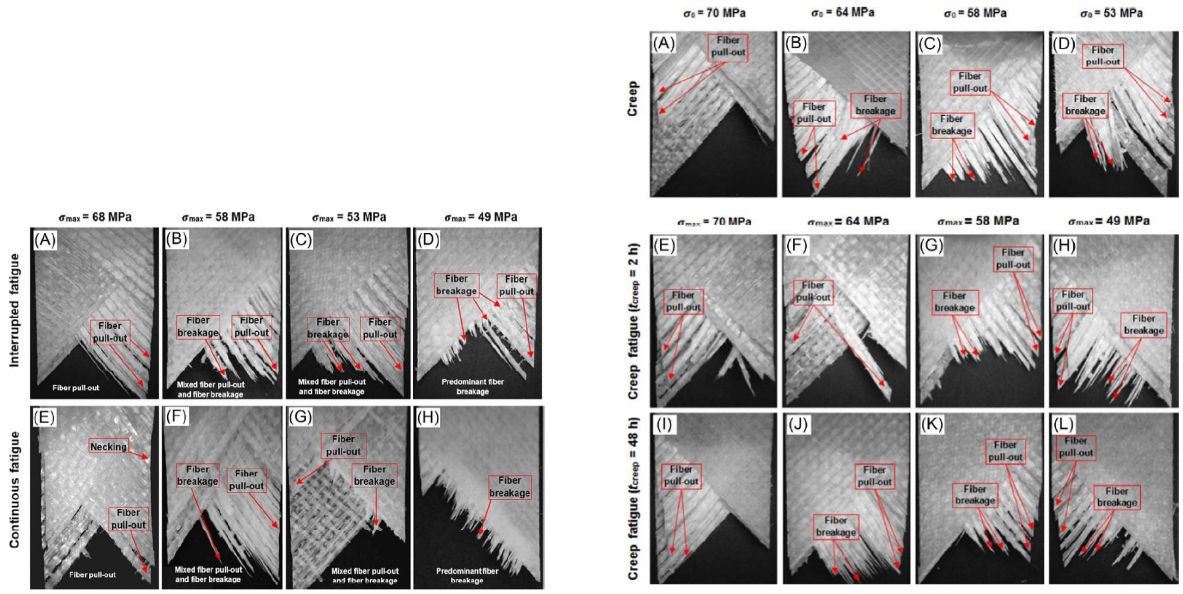
All in all, as the number of cycles progresses, the thermal and optical observations show a transition from distributed to localized damage. Under continuous loading, the temperature and damage remain somewhat homogeneous until rapid localizing near the end of life. Interrupted loading shows 'interrupted' accumulation of temperature, while also remaining localized towards failure. Under creep-fatigue loading, the creep hold can significantly accelerate localized damage, especially at higher stresses and hold times. For lower severity, both the temperature and damage remain relatively distributed allowing for a gradual progression till failure. Ultimately, the localized thermal trends give insight into where it transitions from distributed matrix damage to dominant macroscopic failure.

- **Failure analysis**

  Vassipolous et al. [29] also looked into the main failure mechanisms that spanned across all specimens and loading conditions. The main two dominant failure mechanisms that were identified at failure are fiber breakage and fibre-pull out. Most specimens failed through a mixed-mode combination of these two mechanisms.

  For higher stress levels, the failure was dominated by extensive fibre pull-out, reflecting severe degradation of the matrix-fibre interfaces and reduced load transfer from matrix to fibres. For lower stress levels, failure shifted toward predominant fibre breakage, corresponding to a more uniform and less severe damage distribution that allowed stresses to be effectively transferred to the fibre before failure.

For continuous and interrupted, the overall failure modes were similar, although the interrupted loading showed slightly less severe damage localization - shown in Figure 2.40a. Creep and creep-fatigue loading produced diagonal damage patterns aligned with the fibre orientation, confirming matrix and interface-dominated damage mechanisms. Under creep–fatigue conditions, longer hold times and higher stresses promoted interface degradation, increasing the extent of fibre pull-out and accelerating failure. This can be seen in Figure 2.40b.



(a) *Continuous and Interrupted fatigue*

(b) *Creep-fatigue loading patterns*

Figure 2.40: *Failed Specimens Images*

Above a lot of information is noted on the nature and behavior of matrix-dominated composites, specifically looking into ±45° stacking sequence. The most important concluding remarks to note are as follows.

- These time-dependent mechanisms, such as creep, recovery, ratcheting and self-heating are non-negligible and should be explicitly acknowledged when interpreting fatigue response.
- The loading method, whether it is frequency, strain rate or stress rate, can shift the governing mechanisms. Therefore, variations in these parameters between different points on an S–N curve may reduce the direct comparability of the resulting fatigue behaviour across stress levels.
- Self-heating becomes localized as failure starts forming, and creep-fatigue loading at high stress/long hold time accelerates this localization.

These coupled factors make specific assumptions of Krieg's framework questionable, so each assumption must now be explored individually.

2.3.2. Breakdown of Assumptions

Subsection 2.2.2 summarized the main findings of Krieg's thesis and highlighted the areas where discrepancies may arise when the framework is applied to matrix-dominated composites. Having discussed the behaviour unique to matrix-dominated composites in Subsection 2.3.1, the key assumptions underlying the framework, and how and why these assumptions break down in the context of matrix-dominated composites are identified in this section.

- **The "Closed Loop" Assumption**

  Krieg assumes that the hysteresis loops are considered "closed", as depicted in Figure 2.41, suggesting that the framework decouples creep acknowledging its negligibility for fibre-dominated cases.

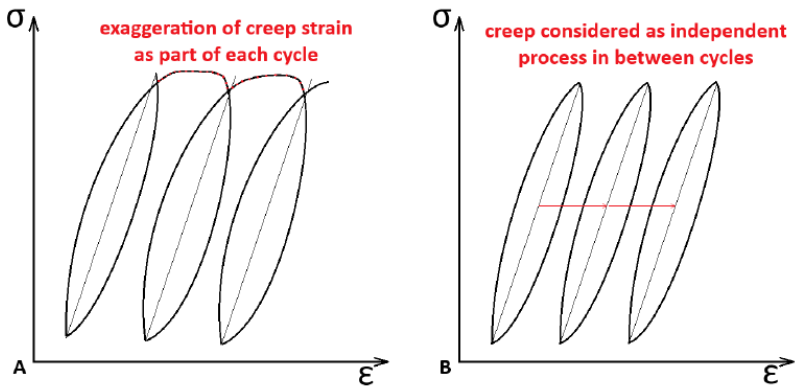


Figure 2.41: *"Closed" Loop Assumption as depicted in Krieg's thesis [1]*

Movahedi-Rad et al. [38] studied ±45° glass/epoxy laminates and outlined that the shift of the hysteresis loops constitutes the cyclic effects of the material which are non-negligible in matrix-dominated composites. Therefore, the two cannot be cleanly decoupled; the hysteresis loop shape from the loop shift as the coupled mechanisms drive the viscoelastic matrix flow, which is more prevalent for matrix-dominated composites.

- **Independence of Creep & Fatigue**

  Similarly to the "decoupled" nature discussed above, Krieg treats creep and fatigue as independent processes, stating that "if indeed the total dissipated energy... follows a constant power-law relation...independent of the R-ratio as suggested by Movahedi-Rad et al..". However, for ±45°, Movahedi-Rad et al. [39] explicitly identify that neglecting the creep term leads to non-applicability of this idea when the stress ratio increases towards 1.0, allowing the mean stress to increase and therefore, a larger presence of creep. Movahedi-Rad et al.'s [11] paper presents a model where the total dissipated energy W is the summation of the dissipated energy due to cyclic loading W_{cyclic} and creep loading W_{creep}, and they propose stress ratio correction factors due to the cyclic and creep loading, as ψ_{cyclic} and ψ_{creep} respectively. The specific correction terms written as a function of stress-ratio R is shown below:

$$\psi_{\text{cyclic}}(R) = \frac{(1+R)}{(1+R_0)}\frac{(1-R)^2}{(1-R_0)^2} \qquad \psi_{\text{creep}}(R) = \left[\frac{(1+R)}{(1+R_0)}\right]^{1+n} \tag{2.14}$$

  Krieg only makes use of the cyclic stress ratio correction in his life prediction equation, which suggests that incorporating the time-dependent creep term might exhibit more accurate predictions for ±45° laminates. While acknowledging the absence of the creep term, the use of the same stress-ratio term is questionable.. This is because Movahedi-Rad et al. [11] derives this term using Thale's theorem by assuming that the cyclic stiffness would be comparable at different R-ratios and the stiffness does not affect the hysteresis loop area. The question becomes if this is still the case for matrix-dominated cases. Consequently, the limitations are twofold: the negligence of the creep term but also if Thales' theroem still holds.

- **Constant vs. Dynamic Stiffness**

  Krieg's life prediction equation makes use of the "average complex modulus" ($|E^*|_{avg}$) as shown below.

$$N_{f,R_2} = N_{f,R_1}\frac{\left(\frac{1-R_1}{1+R_1}\right)^2}{\left(\frac{1-R_2}{1+R_2}\right)^2}\frac{\left(1-R_1^2\right)|E^*|_{\text{avg},R_2}\sin\left(\phi_{\text{eff},R_1}\right)}{\left(1-R_2^2\right)|E^*|_{\text{avg},R_1}\sin\left(\phi_{\text{eff},R_1 2}\right)} \tag{2.15}$$

  Contrary to fibre-dominated composites, ±45° laminates showcase a three-stage stiffness degradation phenomenon that is too significant to be classified under one "averaged" quantity. This is supported

by Manjunatha, C. [40] who studied how shear-loaded laminates, such as the ±45° one, initially, go through a rapid drop, followed by a linear decline and finally, an accelerated descent due to delamination. Numerically, the stiffness can drop by 20-30% which discourages the use of an "average" quantity. In addition, Movahedi-Rad et al. [38] and Sartorio, S. [41] both note that during the specimen's life, it is subjected to fiber re-alignment, meaning more fibre in the direction of the load and therefore, a larger stiffness value. This is something that is overlooked in Krieg's model.

2.4. Fatigue Life Prediction

Having established the challenging nature of ±45° laminates and the resulting limitations that may surface when applied to Krieg's framework, attention is now directed towards the primary objective of this thesis: fatigue life prediction. Subsection 2.4.1 provides a general overview of existing fatigue life prediction models for fibre-reinforced composites. Subsequently, Subsection 2.4.2 transitions into the prediction model applicable to this thesis, and presents the research objectives formulated to address the identified research gaps.

2.4.1. Overview

The purpose of this thesis is not to entirely develop an extensive model of every related damage mechanism individually, but rather to explore whether measurable macroscopic quantities can be used to predict fatigue life while acknowledging a physically meaningful underlying reasoning.

Vassipoulos [29] gives a high-level overview of existing fatigue life prediction models for composites. The broadest group of theoretical models used to predict composite fatigue behavior is the macroscopic failure theories, which are predominantly empirical. This is chosen largely because of its simplicity. Building on August Wohler's 1850s work, these models plot experiment pairs of stress levels and the number of cycles to failure on a log-log scale, commonly known as the S-N curve. Basquin in 1910 introduced a power-law relationship that fits this trend, with exponents that range between 7 and 25 for composite materials.

$$\sigma_a = \sigma'_f (2N_f)^b \tag{2.16}$$

This is highly relevant to this current thesis due to the extensive use of the S-N curve. However, augmenting onto Krieg's framework, this thesis attempts to move past empirical dependence. Secondly, there are strength and stiffness degradation fatigue theories. These theories model and predict fatigue life by monitoring the actual physical damage state using metrics such as residual strength or residual stiffness. Stiffness degradation is far more evident than strength degradation, noted by Vassipolous [29]. Despite this, it still stands that monitoring the residual strength and stiffness still requires extensive fatigue testing, which, at the end of the day, are intended to be made obsolete with new physics-based prediction models. In addition, other modern modeling techniques exist, such as multiscale modeling which models virtual testing environments that minimize the need for costly physical prototypes and extensive experiments. Nonetheless, it requires a large number of parameters that researchers rarely quantify.

Krieg employs the S-N curve, and sees whether its trend can be predicted using measurable macroscopic quantities such as stiffness degradation and loss factor (using dissipated and applied energy). Subsequently, these quantities prove to be independent/weakly-dependent on R-ratio allowing for a prediction that is fully on the R-ratio correction terms. For the present extension, it should be explored whether this independency still holds for matrix-dominated composites, or if physics-based augmentation parameters are required. The main thing to note is that the current thesis seeks to remain within a physics-based modeling framework and to minimize reliance on empirical data, with fatigue testing used primarily for model validation.

2.4.2. Research Gaps and Questions

Within this framework, the fatigue life prediction problem is structured around the three defining constituents of the S–N curve: the slope, the lower fatigue limit (bottom anchor), and the high-stress or short-life regime (upper anchor). Four principal gaps emerged from the literature concerning the applicability of existing findings to ±45° laminates.

GAP-01: Limited understanding of R-ratio and stress-level dependence on the loss factor for ±45°, and whether its use as a standalone damage metric adequately captures the underlying fatigue mechanisms.

This also is closely related to the dependence of TDE vs. stress-level on R-ratio. Due to their proportionality, it is believed that addressing one of these metrics will lead to resolutions of the other.

GAP-02: Unverified validity of the loss-factor intersection method for HCFS identification, for ±45° laminates.

GAP-03: Ambiguity in defining final-damage onset for CDE, for ±45° laminates.

GAP-04: Uncertainty in the R-ratio dependence of complex modulus E^*, for ±45° laminates.

In addition, severe degradation of the complex modulus E^* raises questions regarding the definition of E_{avg} and its comparability across different stress ratios.

Slope

Addressing Gap-01, Gap-03 and Gap-04 is required to preserve the applicability of Lennart Krieg's fatigue life prediction model, which primarily governs the slope of the S-N curve - as is, therefore, relevant for this section.

Potential Extensions for GAP-01/GAP-03

Lennart Krieg derived his fatigue life prediction framework under the assumption that the relationship between total dissipated energy (TDE) and stress level collapses across different stress ratios. In practice, this assumption was found to break down due to the pronounced increase in energy dissipation during the final failure stage, which introduces a strong stress-ratio dependence. To address this, Krieg introduced a finite integration limit, defining the critical dissipated energy (CDE) by excluding the final failure phase.

While this approach can, in principle, be extended to ±45° laminates, a key challenge lies in identifying whether the onset of the final failure stage can be defined in a clear and physically meaningful manner. In particular, it remains unclear whether suitable criteria such as the onset of tertiary creep or accelerated stiffness degradation can be consistently identified, and whether these indicators coincide. Consequently, the primary objective becomes the systematic observation of fatigue response trends and their dependence on parameters such as stress level, stress ratio, temperature, strain rate, and frequency, in order to assess whether a robust integration limit can be defined that restores collapse of the energy–stress relationship across different stress ratios.

In addition to the uncertainty surrounding the integration limit for CDE, the use of the loss factor as a standalone damage metric for ±45° laminates remains unresolved. This can be investigated by comparing its evolution with complementary indicators derived from the same cyclic stress–strain response, including stiffness degradation, dissipated energy and cyclic ratcheting strain. Agreement between these quantities would support the loss factor as a representative damage metric, whereas diverging trends may indicate that the matrix-dominated response cannot be adequately described by a single scalar parameter. Such a comparison also provides insight into whether the observed dependencies on stress level and R-ratio reflect a consistent underlying damage process.

Research Question-01

To what extent do trends in stiffness degradation, cyclic ratcheting strain, loss factor and dissipated energy derived from cyclic stress–strain data exhibit consistent trends across stress levels and R-ratios, and to what extent can the loss factor therefore serve as a representative standalone damage metric for ±45° laminates?

Potential Extensions for GAP-01/GAP-04

Rather than modifying the integration limit to exclude the final failure stage, an alternative approach is to redefine the energy-based metric itself. It is hypothesized that an appropriate augmentation parameter can be introduced such that the corrected total dissipated energy becomes invariant with respect to the stress ratio. By reformulating the energy metric in this manner, the collapse of fatigue life data across different R-ratios may be achieved without requiring a subjective definition of the onset of final failure. This approach preserves the full fatigue history while shifting the focus toward identifying a physically meaningful correction that accounts for stress-ratio effects in the dissipated energy measure.

So the idea is to introduce an augmentation parameter Ψ such that the corrected TDE is constant with changing R-ratio.

$$\mathrm{TDE}_{\mathrm{corr}}(R) = \Psi(R) \cdot \mathrm{TDE}(R) \tag{2.17}$$

This leads to a modified fatigue life scaling between the two stress ratios R_1 and R_2.

$$N_{f,R_2} = N_{f,R_1} \left(\frac{\frac{1-R_1}{1+R_1}}{\frac{1-R_2}{1+R_2}} \right)^2 \left(\frac{1-R_2^2}{1-R_1^2} \right) \frac{|E^*|_{\text{avg},R_1} \sin(\phi_{\text{eff},R_1})}{|E^*|_{\text{avg},R_2} \sin(\phi_{\text{eff},R_2})} \frac{\Psi(R_1)}{\Psi(R_2)} \tag{2.18}$$

Research Question-02

How can a physics-based augmentation parameter, Ψ, be formulated to reformulate Lennart's fatigue-life prediction equation and compensate for deviations in stiffness degradation and effective loss factor across different stress ratios?

Once the trends are observed and proposed correction concepts are tested, it could be the case that neither the integration limit nor the energy metric redefinition alone may be sufficient to fully isolate stress-ratio effects. Instead, a combination of both approaches may be required to better isolate the relevant damage evolution and enable potential collapse of the TDE vs. stress-level relationship across different R-ratios.

Alternative Slope Determination without Input R_1 fatigue data

Krieg's fatigue life prediction equation, whether used with or without the proposed augmentation parameter, still requires an experimental fatigue dataset at the reference stress ratio R_1 in order to predict the fatigue life of a desired stress ratio R_2. This still imposes some fatigue-testing burden. An approach to eliminate this burden is currently being researched by Sartorio (personal communication) [41]. The idea employs stress-sweep testing (SST) on a single specimen to determine a prediction of the slope of the S-N curve, with the potential to substantially reduce the experimental effort required compared with conventional extensive fatigue campaigns involving multiple specimens.

Sartorio suggests subjecting the specimen to successive blocks of increasing stress amplitude, and implementing Miner's rule to iteratively adjust the S-Nslope until the cumulative damage condition is satisfied. The exact procedure is covered in the subsequent chapter in Section 3.2. While this is currently researched on angle-ply CFRP laminates, its applicability to matrix-dominated ±45° GFRP remains unknown and is of interest to the present study. If successfully applied, the SST-derived slope could potentially replace the input R_1 fatigue dataset required by Krieg's framework, further reducing reliance on extensive constant-amplitude fatigue testing.

Research Question-03

To what extent can stress-sweep testing, and the implementation of Miner's rule, be used to determine the S-N curve for ±45° GFRP laminates, and thereby replace the reference R_1 fatigue dataset required by Krieg's fatigue-life prediction framework?

Bottom Anchor

The discussion of the bottom anchor of the S–N curve is closely linked to GAP-02, which concerns the stress dependence of the effective loss factor. In fibre-dominated laminates, the effective loss factor versus stress level has been shown to collapse across different stress ratios, allowing its intersection with the pristine DMA-derived value to be used as a definition of the high-cycle fatigue strength (HCFS).

However, for matrix-dominated laminates, the collapse is not expected to fall as neatly. The question is whether applying a correction factor is the right way to approach this. The hypothesis is that the stress-ratio dependence should be explicitly acknowledged, and that the individual intersections of the loss-factor curves with the pristine reference may correspond to distinct HCFS values for different R-ratios. Exploring whether these intersections exhibit a consistent and physically meaningful relationship therefore becomes central to understanding the bottom-anchor behaviour.

Research Question-04

How does the effective loss factor vary with stress level across different stress ratios, and how do its intersections with the pristine DMA loss factor correspond to stress-ratio-dependent HCFS values?

Alternative Bottom-Anchor Determination without DMA data

The aforementioned stress-sweep tests may also provide an alternative method for estimating the bottom anchor of the S-N curve. Sartorio proposed that the evolution of the ratio between dissipated energy and applied energy, per successive stress blocks, could be used to identify the onset of fatigue-related damage. Using bilinear regression, the point where this linear trend deviates to a greater slope could suggest the emergence of damage, and may yield an approximation of the fatigue limit. Further details of this determination are presented in Section 3.2.

In combination with the SST-derived input R_1 S-Nslope, this method could potentially reduce all long-duration constant amplitude fatigue tests allowing for a unified physics-based prediction model.

Research Question-05

To what extent can the transition between two linear regimes in the TDE-to-total-work ratio during stress-sweep testing be used to identify a reliable lower fatigue-limit estimate for ±45° laminates?

Upper Anchor

The upper anchor of the S–N curve is not directly associated with the identified gaps; however, there is growing discussion in the literature suggesting that dynamic testing performed at fatigue-equivalent loading rates may provide a more representative measure of strength than conventional quasi-static tests. This motivates a comparison between dynamic and quasi-static test results to assess their relevance for defining the upper anchor. If short-term dynamic tests are shown to reproduce stiffness degradation trends comparable to those observed in fatigue, they could offer a valuable and efficient means of characterizing upper-anchor behaviour and contribute to modeling the S-N curve without fatigue tests.

Research Question-06

To what extent can dynamic tests performed at fatigue-equivalent loading rates provide a suitable basis for defining the upper anchor of the S–N curve?

Main Research Question

The question that unifies all six aforementioned questions is as follows

To what extent do ±45° composite laminates conform to Krieg's modified linear viscoelastic fatigue prediction framework, and how can previously overlooked matrix-dominated behaviors be used to justify the framework's deviation, and be leveraged to extend it?

All in all, the literature review culminates in one main research question and six supporting sub-questions. These address the three principal constituents of the S-N curve, while targeting the four research gaps identified through exploring the matrix-dominated composite behaviour and its hypothesized limited conformity to Krieg's modified linear viscoelastic framework. The six supporting research questions are restated below for completeness.

1. To what extent do trends in stiffness degradation, cyclic ratcheting strain, loss factor and dissipated energy derived from cyclic stress–strain data exhibit consistent trends across stress levels and R-ratios, and to what extent can the loss factor therefore serve as a representative standalone damage metric for ±45° laminates?
2. How can a physics-based augmentation parameter, Ψ, be formulated to reformulate Lennart's fatigue-life prediction equation and compensate for deviations in stiffness degradation and effective loss factor across different stress ratios?
3. To what extent can stress-sweep testing, and the implementation of Miner's rule, be used to determine the S-N curve for ±45° GFRP laminates, and thereby replace the reference R_1 fatigue dataset required by Krieg's fatigue-life prediction framework?
4. How does the effective loss factor vary with stress level across different stress ratios, and how do its intersections with the pristine DMA loss factor correspond to stress-ratio-dependent HCFS values?
5. To what extent can the transition between two linear regimes in the TDE-to-total-work ratio during stress-sweep testing be used to identify a reliable lower fatigue-limit estimate for ±45° laminates?
6. To what extent can dynamic tests performed at fatigue-equivalent loading rates provide a suitable basis for defining the upper anchor of the S–N curve?

The question then becomes: what comes next? The thesis now progresses toward the development of the augmentation parameter, $\Psi(R)$, which forms the focus of the following chapter.

3 The Proposed Framework

This chapter follows the exploration into Schapery's Nonlinear Viscoelastic theory and investigates how its constituent principles can be leveraged to extend Krieg's fatigue-life prediction equation through the introduction of an augmentation parameter $\Psi(R)$, directly addressing Research Question-02. The chapter also positions Research Questions-03, -04, -05 and -06 within the proposed framework, concluding with a schematic representation of the overarching framework.

Section 3.1 introduces Schapery's 1971 paper on the Nonlinear Viscoelastic Theory, followed by how it can be used to augment Krieg's framework. Section 3.2 covers the exact protocol used to acquire these model parameters, while also addressing the bottom- and upper-anchor constituents of the S-N curve, consolidating with the overall schematic overview in Section 3.3.

3.1. Nonlinear Viscoelastic Extension of Krieg's Fatigue-Life framework

Krieg's framework is based on a modified linear viscoelastic theory so extending this framework naturally motivates the consideration of nonlinear viscoelasticity. Lou and Schapery published a paper in 1971 titled 'Viscoelastic Characterization of a Nonlinear Fiber-Reinforced Plastic', which discusses the nonlinear characterization of unidirectional, glass fiber-epoxy material using a thermodynamically based nonlinear constitutive equation [26].

The linear viscoelastic theory is mostly used for the characterization of polymeric materials when the stresses are sufficiently low, which gives a very narrow range relative to the practical total range prior to failure. In reality, most composite materials show a considerable amount of nonlinearity, except for fibres parallel to the loading direction. Naturally, this leads to the discussion of a nonlinear viscoelastic constitutive equation that is required to characterize a matrix-dominated composite, which is the interest of this thesis. Therefore, the motivation lies in reformulating the TDE metric so that its linear component continues to cancel out, thereby isolating only the newly nonlinear factor while otherwise preserving the original structure of Krieg's framework.

A range of constitutive theories has been developed to describe material behaviour by relating stress to the resulting strain response [42]. For nonlinear viscoelastic materials, the constitutive description becomes more complex and require extensive simplifications for simple use. However this characterization necessitates only uniaxial creep and recovery tests which means the constitutive equation for the uniaxial loading condition is sufficient. The corresponding equation is given by

$$\epsilon = g_0 A(0)\sigma + g_1 \int_0^t \Delta A(\psi - \psi') \frac{dg_{2\sigma}}{d\tau}\, d\tau \tag{3.1}$$

This equation treats stress σ as an independent state variable, which is consistent with the load-controlled fatigue tests adopted in this study. The parameters are defined as follows:

- A_0 - Initial linear elastic compliance component
- $\Delta A(\psi)$ - Transient linear elastic compliance component
- ψ - Reduced time, follows $\psi = \psi(t) \equiv \int_0^\tau \frac{dt'}{a_\sigma}$; $\qquad \psi' \equiv \psi(\tau) \equiv \int_0^t \frac{dt'}{a_\sigma}$
- g_0, g_1, g_2 and a_σ - the four stress-dependent parameters that distinguish the nonlinear formulation from its linear counterpart.

In simpler terms, the nonlinear constitutive equation is composed of two parts: the initial component and the transient component of strain. The transient component is referred to as 'delayed' compliance that depends on reduced time, which is time corrected by a stress-dependent term a_σ which controls how quickly the material experiences viscoelastic time under a given stress state.

For the present application, the stress-dependent terms are assumed to remain constant within one fatigue loading cycle. Even though the cyclic stress $\sigma(t)$ is time-varying, the nonlinear parameters are kept at a constant representative stress state. This assumption is justified by the fact that the stress-dependent parameters are considered relatively constant over a duration of a single fatigue cycle, especially at higher stress ratios where the amplitude is smaller. At the same time, the higher mean stress associated with higher stress ratios may increase creep and ratcheting effects which may make this framework particularly relevant in that

regime. Under this assumption, the reduced time simplifies to

$$\psi(t) = \int_0^t \frac{dt'}{a_\sigma} = \frac{t}{a_\sigma}. \qquad \Longrightarrow \qquad \psi - \psi' = \frac{t-\tau}{a_\sigma}. \tag{3.2}$$

Subsequently, under the assumption that the linear transient creep compliance follows a power-law relation, it becomes

$$\Delta A(\psi) = C\psi^n \qquad \Longrightarrow \qquad \Delta A(\psi - \psi') = C\left(\frac{t-\tau}{a_\sigma}\right)^n. \tag{3.3}$$

In addition, since g_2 is also considered constant over a cycle,

$$\frac{d\left[g_2\sigma(\tau)\right]}{d\tau} = g_2\frac{d\sigma(\tau)}{d\tau}. \tag{3.4}$$

Finally reducing to

$$\epsilon(t) = g_0A(0)\sigma(t) + \frac{g_1g_2}{a_\sigma^n}\int_0^t C(t-\tau)^n\frac{d\sigma(\tau)}{d\tau}\,d\tau. \tag{3.5}$$

Essentially, this can be presented as the elastic component and viscous component, which together define the viscoelastic strain response.

$$\epsilon(t) = \underbrace{g_0A(0)\sigma(t)}_{\text{elastic part}} + \underbrace{\int_0^t C(t-\tau)^n\frac{d\sigma(\tau)}{d\tau}\,d\tau}_{\text{viscous part}}. \tag{3.6}$$

For comparison, the linear constituent equation can be acquired by simply equating the stress-dependent terms to one ($g_0 = g_1 = g_2 = a_\sigma = 1$).

$$\epsilon(t) = A_0\sigma + \int_0^t C(t-\tau)^n\frac{d\sigma}{d\tau}\,d\tau \tag{3.7}$$

Considering the transient terms, it shows that the nonlinear viscous strain response is related to the linear counterpart where the proportionality term is a ratio between the stress-dependent terms.

$$\epsilon_{\text{nl, viscous}} = \left[\frac{g_1g_2}{a_\sigma^n}\right]\epsilon_{\text{linear, viscous}} \tag{3.8}$$

. This can be adopted to extend the definition of dissipated energy. The dissipated energy is defined as the enclosed area of a stress-strain hysteresis loop, refer to Figure 2.1.

$$W_{\text{cycle}} = \oint \sigma(t)\,d\epsilon = \pi\sigma_0\epsilon_0\sin(\delta) \qquad \text{where} \quad \epsilon_0 = \epsilon_{\text{nl, viscous}}. \tag{3.9}$$

The strain ϵ can be scaled by the proportionality term Ψ, thereby scaling the dissipated energy itself.

$$\Delta W_{\text{nl}} = \left[\frac{g_1g_2}{a_\sigma^n}\right]\Delta W_{\text{linear}} \qquad \Longrightarrow \qquad \text{TDE}_{\text{nl}} = \left[\frac{g_1g_2}{a_\sigma^n}\right]\text{TDE}_{\text{linear}}. \tag{3.10}$$

This provides the first stepping stone into introducing Schapery's nonlinear viscoelastic description into Krieg's framework. Krieg [1] states that his life-prediction equation is under the assumption that the total dissipated energy follows a constant power-law relation with maximum stress, independent of the stress-ratio. However, it is still of question whether this still holds for matrix-dominated cases where the higher stress-ratios would still equate to the same total dissipated energy at the same maximum stress.

Therefore, introducing nonlinearity, the total energy dissipated becomes

$$\text{TDE}_{nl} = \Psi\cdot\text{TDE}_l. \tag{3.11}$$

At the same maximum stress, the equivalent ratio corresponding to a different R-ratio R_2 can be related to the first test through Equation 2.8.

$$\frac{\left(\frac{\text{TDE}}{\text{TW}}\right)_{R_1}}{\left(\frac{\text{TDE}}{\text{TW}}\right)_{R_2}} = \frac{\left(\frac{1-R_1}{1+R_1}\right)^2\sin\left(\phi_{\text{eff}}\right)_{R_1}}{\left(\frac{1-R_2}{1+R_2}\right)^2\sin\left(\phi_{\text{eff}}\right)_{R_2}}. \tag{3.12}$$

Under the assumption of a constant *linear* TDE_l for equal maximum stress,

$$\frac{\left(\frac{\mathrm{TDE}}{\mathrm{TW}}\right)_{R_1}}{\left(\frac{\mathrm{TDE}}{\mathrm{TW}}\right)_{R_2}} = \frac{\left(\frac{\Psi_{R_1}\,\mathrm{TDE}_l}{\mathrm{TW}}\right)_{R_1}}{\left(\frac{\Psi_{R_2}\,\mathrm{TDE}_l}{\mathrm{TW}}\right)_{R_2}} = \frac{\mathrm{TW}_{R_2}}{\mathrm{TW}_{R_1}}\frac{\Psi_{R_1}}{\Psi_{R_2}}. \tag{3.13}$$

The total applied work ratio on the right-hand side of Equation 3.13 can be further extended using Equation 2.7. Thereafter, it can be equated to each other to form Equation 3.14.

$$\frac{\left(1-R_2^2\right)N_{f,R_2}\,|E^*|_{\mathrm{avg},R_1}\,\Psi_{R_1}}{\left(1-R_1^2\right)N_{f,R_1}\,|E^*|_{\mathrm{avg},R_2}\,\Psi_{R_2}} = \frac{\left(\frac{1-R_1}{1+R_1}\right)^2 \sin\left(\phi_{\mathrm{eff}}\right)_{R_1}}{\left(\frac{1-R_2}{1+R_2}\right)^2 \sin\left(\phi_{\mathrm{eff}}\right)_{R_2}}. \tag{3.14}$$

Finally, the aforementioned equation can be re-arranged to predict the number of cycles to failure for a stress ratio of R_2, given a dataset for R_1.

$$N_{f,R_2} = N_{f,R_1}\frac{\left(\frac{1-R_1}{1+R_1}\right)^2}{\left(\frac{1-R_2}{1+R_2}\right)^2}\frac{1-R_1^2}{1-R_2^2}\frac{|E^*|_{\mathrm{avg},R_2}}{|E^*|_{\mathrm{avg},R_1}}\frac{\sin\left(\phi_{\mathrm{eff}}\right)_{R_1}}{\sin\left(\phi_{\mathrm{eff}}\right)_{R_2}}\underbrace{\frac{\Psi_{R_2}}{\Psi_{R_1}}}_{\text{New}}. \tag{3.15}$$

Consequently, the novel extension to Krieg's original fatigue life prediction equation is the augmentation parameter,

$$\frac{\Psi_{R_2}}{\Psi_{R_1}}. \tag{3.16}$$

In this proposed formulation, R_1 is modeled to be smaller than R_2, in the regime of tension-tension fatigue $R > 0$. For example, a commonly tested stress ratio in the literature is R=0.1 [43] [44], which can be used as the reference condition to predict higher, less-common stress ratios, $R_2 > R_1$. Given this interpretation, R_2 fatigue behavior is expected to display a greater nonlinearity than R_1, due to the larger mean stress in higher stress-ratios. As an initial approximation, the nonlinear augmentation parameter at the reference condition R_1 is approximated to 1.

$$\frac{\Psi_{R_2}}{\Psi_{R_1}} \approx \frac{\Psi_{R_2}}{1} \qquad \text{where} \quad \Psi_{R_2} = \frac{g_1 g_2}{a_\sigma^n}. \tag{3.17}$$

This approximation is also compatible with the intended characterization protocol for the nonlinear parameters. The identification is based on step-wise isothermal, uniaxial creep and recovery tests, where during the creep hold, the specimen is subjected to a constant prolonged stress. If this creep stress was equated in the context of maximum stress in fatigue loading σ_{max}, then two fatigue conditions with the same maximum stress but different stress-ratios will still be characterized by the same creep stress. Under this consideration, the physical distinction between the two Ψ values for the stress-ratios becomes unclear.

An important feature of Krieg's final applied formulation of Equation 3.15 is that effectively the stiffness and effective loss-factor ratios were collapsed to unity across the investigated stress-ratios. Under this observation, the corresponding terms were removed from the final equation, yielding a simpler prediction equation. Whether this same simplification remains valid for this present study of $\pm 45°$ is uncertain. Ideally, these terms would still either be shown to remain somewhat invariant and approximate to unity, or be replaced by a physically meaningful ratio to ensure limited empirical fitting. This is directly addressed in Research Question-01, which examines whether relevant fatigue-response quantities evolve in a sufficiently consistent manner to permit such a simplification. In the proposed framework, the goal is to retain only the explicit stress-ratio correction terms along with the nonlinear augmentation extension, while avoiding empirical corrections.

Overall, the proposed framework preserves the structure of Krieg's original fatigue-life prediction while introducing a nonlinear viscoelastic correction through the augmentation parameter $\Psi = \frac{g_1 g_2}{a_\sigma^n}$. Given the material, a high 'nonlinearity' score could allow for augmentation of the equation while for more linear states, the ratio approaches unity and the formulation reduces to Krieg's original equation.

$$\text{Life Prediction Equation}: N_{f,R_2} = N_{f,R_1}\frac{\left(\frac{1-R_1}{1+R_1}\right)^2}{\left(\frac{1-R_2}{1+R_2}\right)^2}\left(\frac{1-R_1^2}{1-R_2^2}\right)\left(\frac{g_1 g_2}{a_\sigma^n}\right) \tag{3.18}$$

3.2. Identification of Model Parameters

This section establishes the exact protocol required to extract the parameters required to apply the proposed framework. Note that the creep and recovery testing procedures are described later in the methodology chapter, the present discussion assumes that the creep and recovery strain data is available and presents the post-processing methodology to obtain parameters g_0, g_1, g_2 and a_σ^n in Subsection 3.2.1. Thereafter, the section is extended by discussing the identification of required parameters to characterize the remaining constituents of the S-N curve, in Subsection 3.2.3.

3.2.1. Model Parameters for the Slope Constituent (Implementation of Ψ Augmentation)

The procedure beings with the measured creep and recovery strain data as a function of time, ϵ_c and ϵ_r respectively. This should be obtained at several constant stress levels. The steps undertaken to achieve these parameters are numbered and referenced in the schematic diagram presented in Section 3.3.

Extracting n and a_σ from recovery data.

Step 1) **Plot the recovery strain data on reduced coordinates**

For each of the different stress levels, plot the recovery data ϵ_r against the reduced time,

$$\lambda = \frac{t - t_1}{t_1}, \tag{3.19}$$

where t_1 denotes the duration of the preceding creep hold. Both axes should be represented on a logarithmic scale. This should result in a family of curves corresponding to different stress levels. An example can be seen in Figure 3.1.

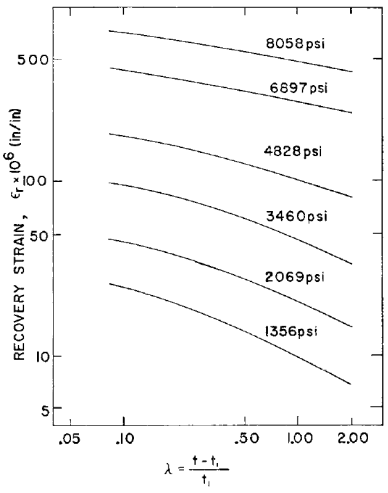


Figure 3.1: *Example plot of the recovery curves from Schapery et al. [26]*

Step 2) **Form a master curve**

Identify the recovery curve at a sufficiently low stress level that can be assumed to be in the linear viscoelastic regime. This becomes the reference curve. The remaining curves will be horizontally and vertically shifted until they collapse onto one curve, thereby forming the master curve. Figure 3.2 shows an example master curve.

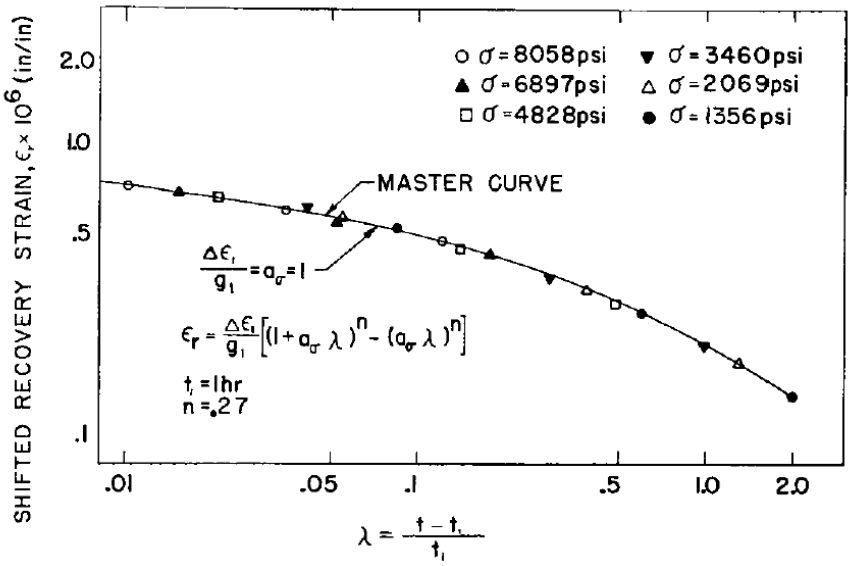


Figure 3.2: *Example Plot of the master curve from Schapery et al. [26]*

Step 3) **Determine the creep power-law exponent *n***

The following relation can be used to fit the master curve,

$$\log(\epsilon_r)_{\text{ref}} = \log\left[(1+\lambda)^n - \lambda^n\right]. \tag{3.20}$$

The exponent n is adjusted until the relation provides the best fit for the existing reference recovery curve.

Step 4) **Determine the stress-dependent time-scale factor a_σ**

The horizontal and vertical shifts used to superpose the curves onto the master curve provide useful parameters for the analysis.

$$\text{Horizontal Shift} = \log(a_\sigma), \quad \text{Vertical Shift} = \log(\frac{\Delta\epsilon_1}{g_1}) \tag{3.21}$$

The horizontal shift directly determines a_σ per stress-level, and the vertical shift will be used in the subsequent steps.

Extracting g_0, g_1 and g_2 from creep data.

Step 5) **Determine intermediate parameters using the low-stress reference data σ**

The following power-law form can be used to fit the creep strain vs. time data.

$$\epsilon(t) = \epsilon_{\text{intercept}} + K t^n. \tag{3.22}$$

where n is one acquired in step 3. Given this fitting, intermediate parameters A_0 and C can be determined as follows,

$$A(0) = \frac{\epsilon_{\text{Intercept}}}{\sigma} \qquad \text{and} \qquad C = \frac{K}{\sigma}. \tag{3.23}$$

Step 6) **Determine g_0, g_1 and g_2 from the next incremental stress level σ_1**

This step requires the strain ϵ_c vs. time curve, a_σ value and the vertical shift = $\log(\frac{\Delta\epsilon_1}{g_1})$ for this stress level σ_1.

Similarly, fit the following curve onto the strain ϵ_c vs. time curve,

$$\epsilon(t) = \epsilon_0 + K' t^n. \tag{3.24}$$

where g_0 can be calculated as [26],

$$g_0 = \frac{\epsilon_0}{A(0)\,\sigma_1}. \tag{3.25}$$

using Equation 3.21 and $\Delta\epsilon_1 = \epsilon(t_1) - \epsilon_0$, g_1 can be found as

$$g_1 = \frac{\Delta\epsilon_1}{10^{(\text{vertical shift})}}. \tag{3.26}$$

Lastly, g_2 can be obtained by calculating the net creep compliance at $t = t_1$ [26],

$$\widetilde{\Delta A}(t_1) = \frac{\epsilon(t_1) - \epsilon_0}{\sigma_i}. \tag{3.27}$$

and given,

$$\widetilde{\Delta A}(t_1) = C\frac{g_1 g_2}{a_\sigma^n} t_1^n \qquad \therefore g_2 = \frac{\widetilde{\Delta A}(t_1)\, a_\sigma^n}{C\, g_1\, t_1^n}. \tag{3.28}$$

Thereafter, repeat this step for the next incremental stress levels.

This provides the nonlinear augmentation parameter which should be used to determine the slope constituent of the S-N curve at a stress-ratio of interest,

$$\text{Life Prediction Equation}: N_{f,R_2} = N_{f,R_1} \frac{\left(\frac{1-R_1}{1+R_1}\right)^2}{\left(\frac{1-R_2}{1+R_2}\right)^2} \left(\frac{1-R_1^2}{1-R_2^2}\right) \frac{g_1(\sigma)\, g_2(\sigma)}{a_\sigma(\sigma)^n}. \tag{3.29}$$

The interdependence of the identified model parameters is summarized in Figure 3.3, which traces how the creep and recovery data are used to determine n, a_σ, g_0, g_1, and g_2, before combining them into the final nonlinear augmentation parameter term used in the fatigue-life prediction framework.

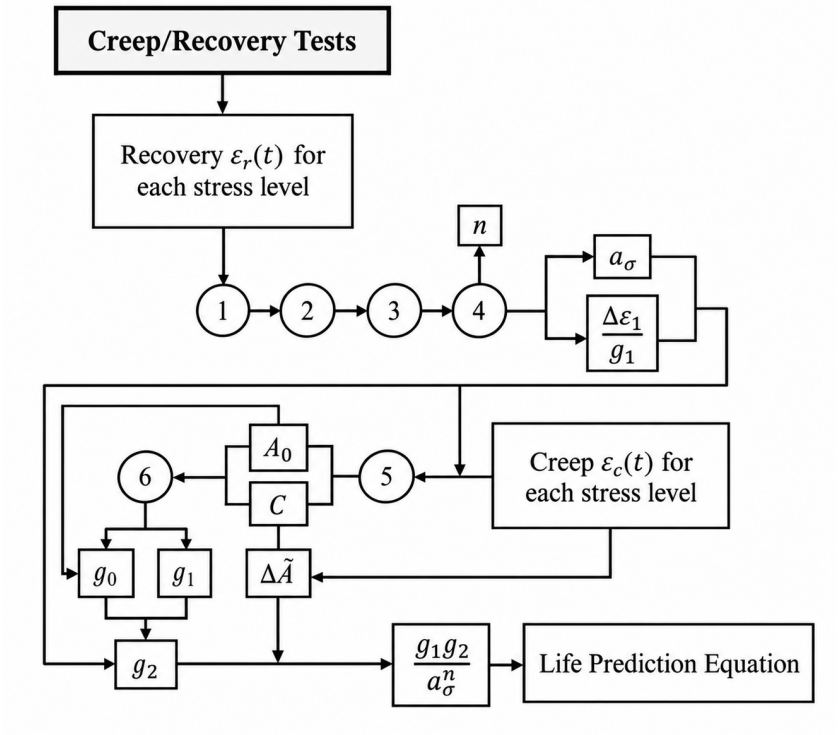


Figure 3.3: *Schematic overview of the nonlinear parameter-identification procedure. Numbered circles denote the sequential identification steps, while rectangular boxes indicate the quantities or model parameters obtained as outputs from each step and subsequently used to determine the final augmentation term.*

3.2.2. Model Parameters for the Slope Constituent (Implementation of SST Miner's Rule)

This section outlines the procedure used to incorporate Sartorio's stress sweep testing approach as an alternative means of estimating the slope of the S-N curve.

Step α) **Identification of damage-active stress levels.**

For each successive stress block, the ratio of the total dissipated energy to the total applied work,

$$\frac{TDE}{W_{tot}}, \tag{3.30}$$

is calculated and plotted against the corresponding stress level. A schematic is shown in Figure 3.4. A bilinear regression approach is used to identify the transition between the two linear regimes. The lower-stress regime is interpreted as the baseline response, where the subsequent stress levels correspond to the onset of fatigue damage. These higher stress levels are hereafter referred to as the *damaged stress levels.*

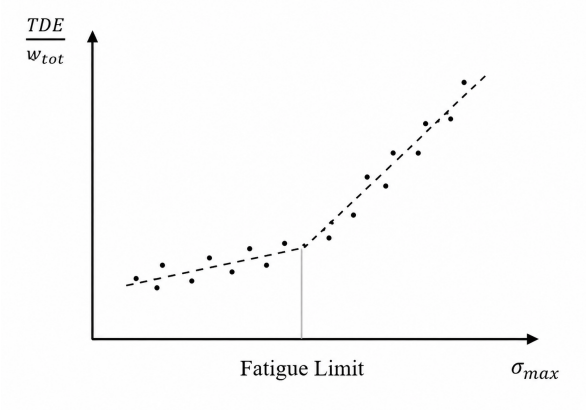


Figure 3.4: *Schematic of TDE/W_{tot} per stress-level allowing determination of the damaged stress levels, and the fatigue limit.*

Step β) **Slope identification using Miner's rule.**

The damaged stress levels are now used as the summation points in a cumulative-damage calculation based on Miner's rule,

$$D = \sum_i \frac{n_i}{N_i}, \tag{3.31}$$

for each *i-th* damaged stress level where n_i is the number of cycles applied, which should be the same for all stress levels, and N_i is the corresponding number of cycles to failure which is the output prediction of this optimization.

The S-N curve slope is then iteratively adjusted such that the damage parameter satisfies

$$D \approx 1. \tag{3.32}$$

The resulting slope can be used as an alternative method to predict the S-N curve for either the input reference stress-ratio R_1, or even the desired stress-ratio R_2 given that the stress-sweep test itself complies with the same stress-ratio of interest.

It should be noted that Miner's rule is used here as an empirical cumulative-damage approximation rather than as a physically based description of fatigue damage. The rule assumes linear damage accumulation and neglects load-sequence effects, interaction between damage mechanisms and changes in the material response as damage evolves. These assumptions are particularly restrictive for matrix-dominated composites, where nonlinear viscoelasticity, ratcheting and interacting failure mechanisms may cause the damage contribution of a given stress level to depend strongly on the preceding loading history. Accordingly, the condition $D \approx 1$ is treated here as a pragmatic criterion for slope identification, rather than as evidence that the accumulated damage has a unique physical meaning.

3.2.3. Model Parameters for the Upper and Bottom Anchor

Contrary to the slope of the S-N curve, which addressed a novel extension to the equation, the two remaining constituents, namely the upper and bottom anchors, are retained from Krieg's original approach rather than reformulated through Schapery's theory. The upper anchor is obtained from fatigue-equivalent strain rate monotonic strength, while the bottom anchor is obtained from the intersection between the pristine DMA loss factor and the fatigue-derived effective loss factor trend against the stress levels. Note that only the parameter-identification procedure is described here, detailed experimental procedures are presented later in Chapter 4.

Upper Anchor

Step a) **Determine the fatigue-equivalent loading rate.**

The monotonic tensile test is performed at a strain rate representative of the fatigue loading condition of interest. Commonly, most monotonic test machines require a displacement rate rather than a strain rate, and therefore the equivalent crosshead displacement rate can be calculated, using the clamp-to-clamp gauge length, as $\dot{\delta} = L\dot{\epsilon}$, where L is the clamp-to-clamp length and $\dot{\epsilon}$ is the target strain rate.

Thereafter, determine the ultimate tensile strength UTS.

The peak value on the resulting stress-strain curve is used to identify the ultimate tensile strength, UTS. This value is represented as the upper anchor at $N_f = 1$. In addition, the UTS value is used to design the stress-sweep tests defining the suitable stress amplitudes per successive blocks.

Bottom Anchor (DMA)

Step i) **Determine the pristine DMA response.**

A temperature sweep is performed using the DMA testing device to obtain the pristine loss-factor response against a working temperature range. The response also provides information on the glass-transition temperature, T_g, which is useful for defining suitable thermal conditions for the creep and recovery characterization methodology which is described later in the methodology chapter.

Step ii) **Select a representative pristine loss factor.**

From the measured loss-factor vs. temperature plot, a representative pristine loss factor is selected from the approximately stable region below the onset of the glass-transition response. This is expected to be less stable for more temperature-sensitive material, such as matrix-dominated composites. This value is intended to characterize the undamaged viscoelastic state of the material.

Step iii) **Identify the HCFS intersection.**

From the reference R_1 fatigue dataset, the effective loss factor can be calculated for each stress level using

$$\sin\left(\phi_{\text{eff}}\right) = \frac{1}{\pi}\frac{\text{TDE}}{\text{TW}}\left(\frac{1+R}{1-R}\right)^2. \tag{3.33}$$

The resulting values are plotted against their corresponding stress level to establish a linear best-fit line, where the pristine loss factor's intersection with this line results in the HCFS value. This intersection defines the bottom anchor of the S-N curve.

Bottom Anchor (SST)

The same stress-sweep dataset can also provide an alternative approach of estimating the bottom anchor of the S-N curve. As described above, the ratio TDE/W_{tot} is evaluated per stress level of each successive block and plotted against the corresponding stress level, refer to Figure 3.4. A bilinear regression is applied to identify the transition between the initial *undamaged* linear baseline and the subsequent linear regime with increased damage. The intersection of the two fitted trends is interpreted as the fatigue limit.

3.3. Schematic Overview of the Proposed Framework

To conclude the chapter, this section presents an overarching schematic representation of the fatigue-life prediction framework. A more detailed workflow for determining Ψ, corresponding to the light-blue dotted region, is provided in Figure 3.3.

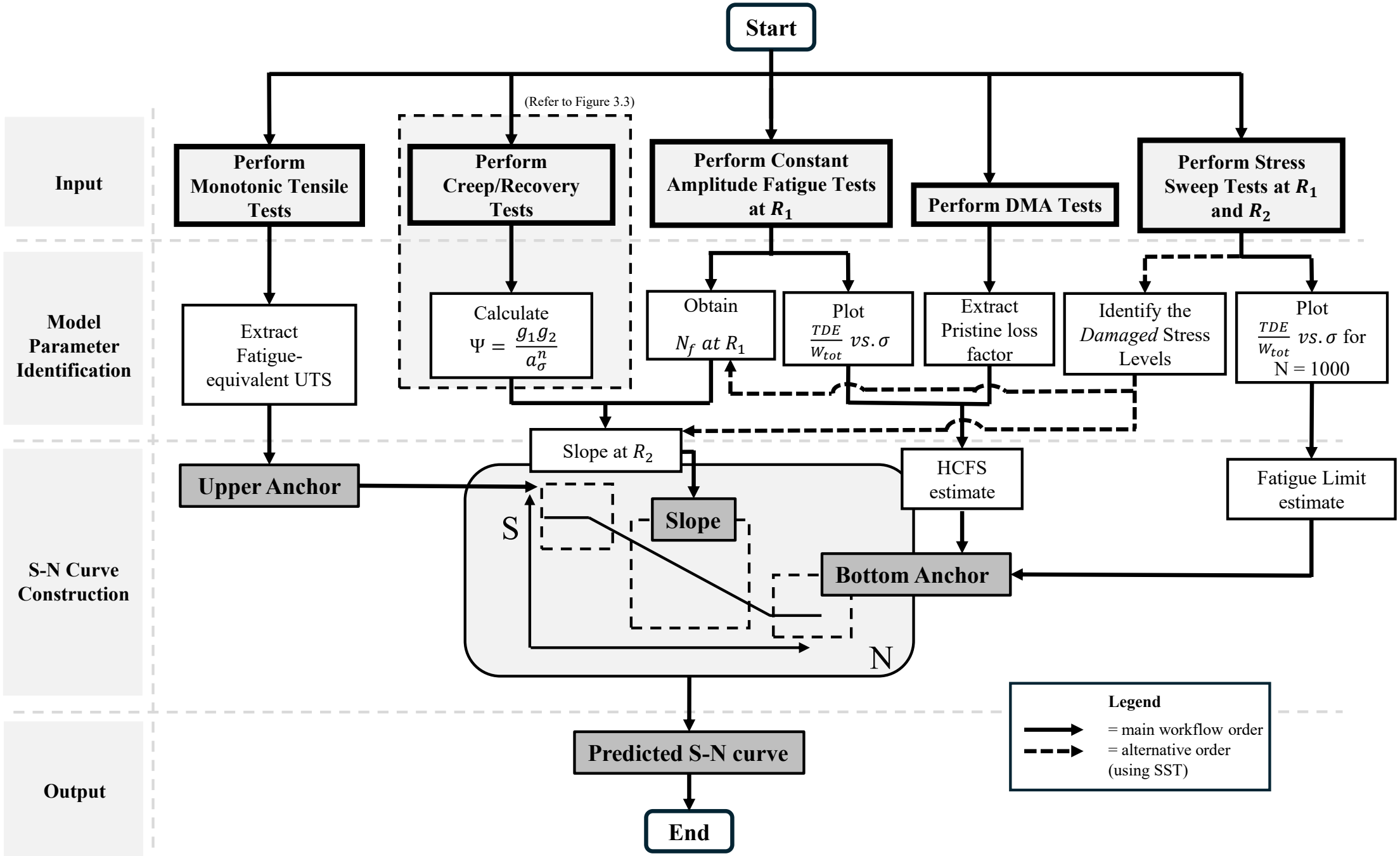


Figure 3.5: *Flowchart of the proposed framework for S–N curve construction.*

4 Experimental Methodology

This chapter covers the methodology undertaken to answer the established research questions. Section 4.1 discusses the major aspects of experimental design considerations such as specimen design and loading parameter. Section 4.2 summarizes the main manufacturing process taken to create the final specimens. Lastly, Section 4.3 presents how the five principal experimental campaigns are designed such that appropriate input and validation data are obtained.

4.1. Experimental Design

Prior to performing the experiments, several major aspects of the experimental design required careful consideration, namely the specimen design and loading strategy. These aspects are investigated in detail in the present study in Subsection 4.1.2 and Subsection 4.1.3, respectively. In addition, the chosen overarching material system is described in Subsection 4.1.1.

4.1.1. Chosen Material and Lay-up

Since the present study is centered around the validation of Lennart Krieg's framework on matrix-dominated composites, the material and laminate selection is straightforward maintaining the same material system as Krieg's, as controlled variables, and only differing the lay-up. The principal independent variable is the stacking sequence: transitioning from Krieg's fibre-dominated $[0/90]_{4s}$ to a matrix-dominated $[\pm 45]_{4s}$ lay-up.

The selection of $[\pm 45]_{4s}$ to represent the matrix-dominated is used as this is widely used in literature and aerospace applications [45] [46]. In literature, ASTM D3518/D3518M specifically necessitates this stacking sequence to determine in-plane shear stress strain response, directly supporting the characterization of matrix-dominated behavior. This makes $[\pm 45]_{4s}$ a suitable configuration for examining the validation of Krieg's framework under a matrix-dominated environment.

To ensure comparability with Krieg's study, the same glass-fibre/epoxy prepreg was selected, and its properties are summarised in the table below.

Table 4.1: *Material properties of the glass-fibre UD prepreg system [1].*

Property	Specification
Material designation	Deltapreg glass UD EGL-200-BT080-34 EF
Fibre type	E-glass
Matrix system	BT080 OoA epoxy-based resin system
Fibre areal weight	200 g/m^2
Resin content by weight	34%
Cured fibre volume fraction	0.49
Cured ply thickness	0.157 mm

4.1.2. Specimen Design

The primary objective of the specimen design is to ensure consistent, localized failure within the central gauge section, avoiding invalid failure modes such as tab debonding or stress concentrations at the gripping interface. While ASTM D3479 provides standard guidelines for tension-tension fatigue of polymer matrix composites, it typically suggests rectangular specimens (250mm × 25mm). However, for matrix-dominated laminates such as ±45°, the lower transverse stiffness and shear-driven deformation mechanisms require specific geometric modifications to minimize the influence of clamping constraints and Poisson contraction at the grips.

To address these challenges, a custom dogbone geometry is adopted, maintaining comparability with previous work by Krieg while exploring a novel geometry design developed by Sofia Sartorio and Julia Carvalho [47], hereafter referred to as the *Double Euler* geometry.

Tab Design

For the tab design, attention is given to minimizing the stiffness mismatch. The ASTM D3039 suggests E-glass reinforced composite tab at an orientation of ±45° to the load direction, which advantageously is the same

stacking sequence as the specimen material allowing for minimized stiffness mismatch. According to the same aforementioned standard, a thickness of 1.5 mm is chosen and it is bonded to the main material using Loctite AE 3430. For proper grip, a tab length of around 60 mm is chosen. Both of these remain the same as Krieg's specimen allowing comparability.

Table 4.2: *Summary of tab-design parameters.*

Parameter	Selected value / specification
Tab material	±45° GFRP/epoxy (same as specimen)
Tab thickness	approx. 1.5 mm (ten plies)
Tab length	60 mm
Adhesive	Loctite EA 3430 structural adhesive

Specimen Geometry Selection

Dogbone-type specimens are promoted to force failure in the gauge section rather than at the grips. This can be achieved by reducing the gauge width relative to the tabbed section which attracts a greater local stress at the gauge due to its smaller cross sectional area. However, curved transitions could allow for additional shear stresses and therefore are not generally preferred in literature. Yet, with some numerical optimizations, a carefully constructed geometry could be used such that failure outside of the gauge section is not risked.

On this basis, five different geometry concepts were considered for this exploration; rectangular, single radius, double radius, linear and Double Euler as can be seen in Figure 4.1.

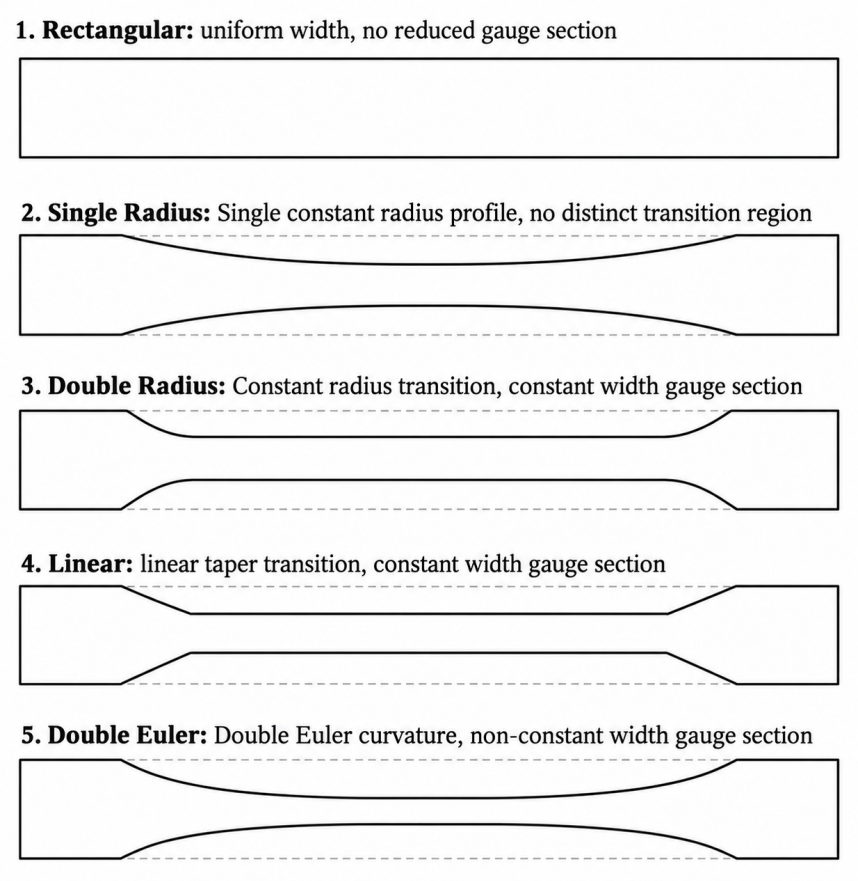


Figure 4.1: *Comparison of specimen geometries: rectangular, single-radius, double-radius, linear-taper, and double-Euler profiles. The gauge width was held constant across all five geometries to maintain the same nominal gauge stress for direct comparison; this constant gauge width is not accurately represented in the schematic.*

Krieg evaluated the linear, single radius and double radius geometries, ultimately selecting the single-radius geometry for his corresponding fibre-dominated specimens. These concepts are retained in the current study as useful basis for comparison and assessing suitability for this ±45° stacking sequence. In addition, a conventional rectangular specimen is explored because ASTM D3518 or ISO 14129 adopt straight-sided rectangular specimens, and therefore their suitability can be assessed in comparison with the other geometries. Finally, a further geometry, developed by Sartorio and Carvalho [47], was also explored, called "Double Euler". This builds on the non-parallel gauge width, similarly to the single radius, with the aim to further optimize and force the greater local stress within the gauge.

The primary aim of the optimization is to compare the different geometries under an equivalent gauge-section stress state. This was conducted on ABAQUS, subjected to a tensile load selected to achieve consistent gauge-section stresses for all the geometries. The parameters of importance are,

- S_{11}, representing the normal stress in local fibre direction of each +45 and −45 plies, and
- S_{12} representing the in-plane shear stress in the local 1-2 plane.

These two parameters were extracted as a function of distance along the clamp-to-clamp length, which are presented in Figure 4.2.

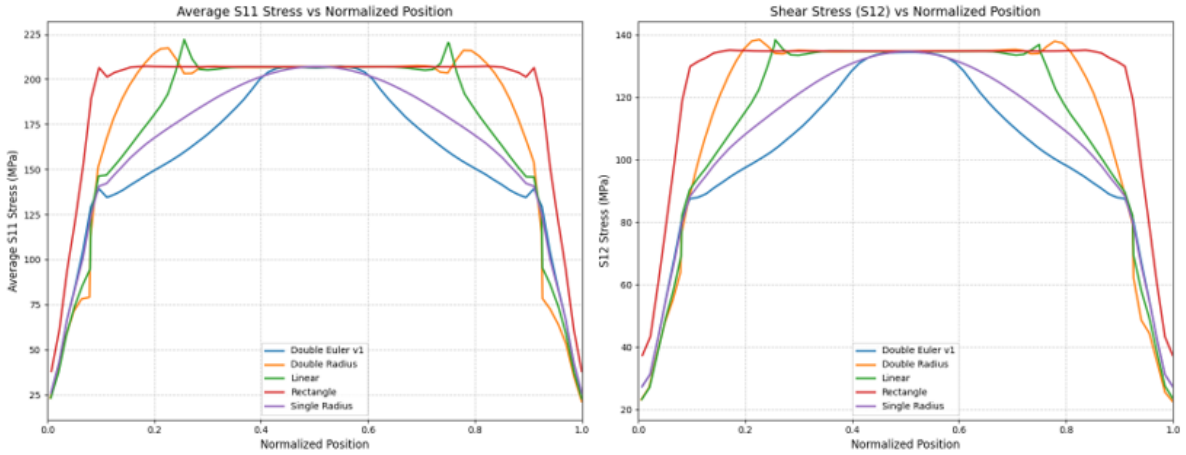


Figure 4.2: *S11 normal stress (left) and S12 shear stress (right) against the clamp-to-clamp distance of the specimen, for the five geometry concepts.*

The preferred geometry was identified as the geometry concept that allowed the peaks of S_{11} and S_{12} to be close to each other, and overall being near the gauge section. Therefore Figure 4.2 shows that the "best" specimen geometry in this case is the Double Euler.

The discussion is shifted to the size and dimensions of the selected geometry, with particular attention to the gauge-to-tab width ratio. Krieg discusses the importance of a criterion of

$$w_{gauge}/w_{tab} < 0.8 \tag{4.1}$$

to avoid grip-related failure. The same reference may not be as strict for angle-ply ±45° configuration yet a narrower gauge section would be advantageous nonetheless. Therefore, a parametric study is conducted on ABAQUS evaluating the S_{11} and S_{12} responses to three different w_{gauge}/w_{tab} ratios of 0.68, 0.71 and 0.78. The latter two are comparable in relation to Krieg, and 0.68 was included to compare with the specimens used by Sartorio, who adopts this ratio [41].

The results of this parametric study can be seen in Figure 4.3 which showcases limited sensitivity. On this basis, a w_{gauge}/w_{tab} ratio of 0.71 was adopted.

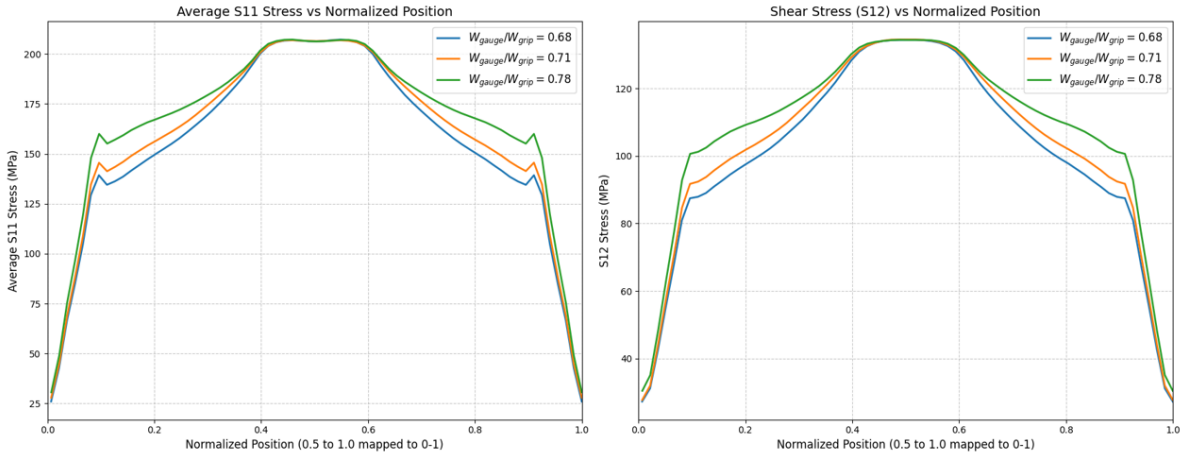


Figure 4.3: *S11 normal stress (left) and S12 shear stress (right) against the clamp-to-clamp distance of the specimen, for a narrowing ratio of 0.68, 0.71 and 0.78.*

Final Specimen

Figure 4.4 presents the final chosen geometry, and the relevant dimensions; gauge width of 16.4 mm, gauge thickness of approximately 3 mm (16 plies), tab length of 60 mm, tab thickness of approximately 1.5 mm (10 plies), overall specimen width of 23 mm and a total length of 290 mm.

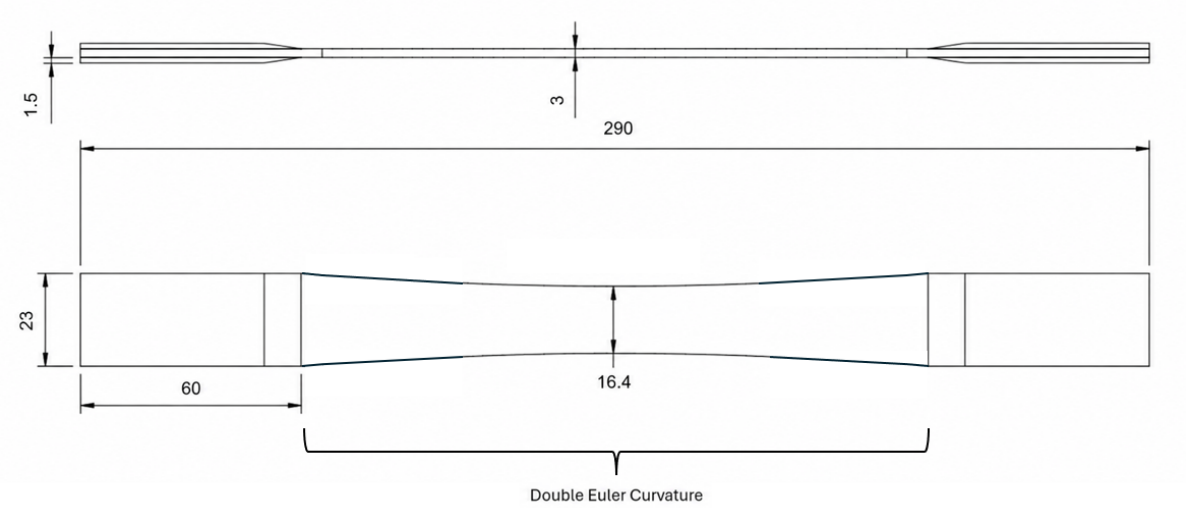


Figure 4.4: *Final Specimen Geometry and Dimensions*

The *Double Euler* curvature can be seen more accurately in Figure 4.5 which presents the ABAQUS sketch and the real-life geometry side-by-side.

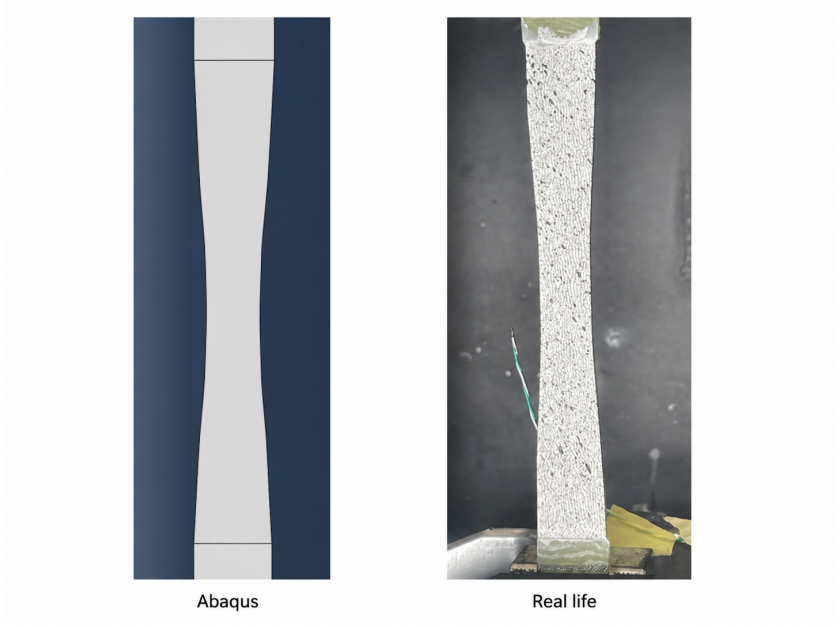


Figure 4.5: *Side-by-side view of ABAQUS sketch (left) and real-life specimen (right), showing the Double Euler Geometry.*

4.1.3. Loading Strategy

A critical deviation from standard industrial practice is the selection of the loading parameter in fatigue testing. While standard composite fatigue protocols, such as ASTM D3479/ASTM D379M, often suggest a fixed loading frequency in the range of 5- 10 Hz, this approach fails to account for the material's viscoelastic rate sensitivity and self-heating, leading to inconsistent material behaviour across different stress levels and stress-ratios.

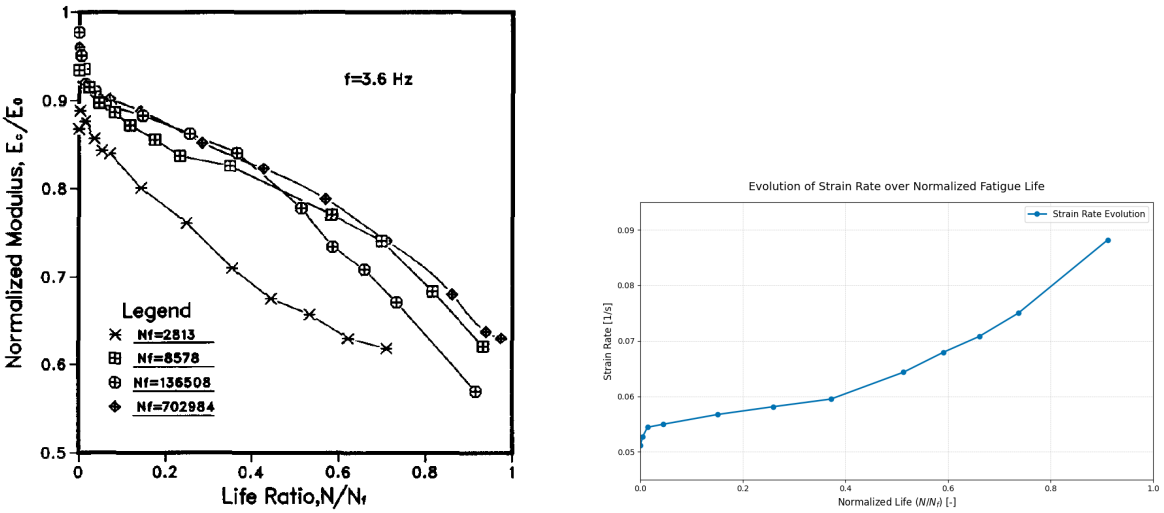
Frequency controlled testing introduces competing effects, where self-heating and viscoelastic/creep effects evolve simultaneously and non-uniformly across different stress levels and stress-ratios, making direct comparisons difficult. A constant strain rate approach is adopted following the recommendation of Lennart Krieg, as it is consistent with the objective of this thesis to evaluate composite fatigue behaviour from an energy dissipation ratio perspective. This requires acknowledging rate-dominated effects on stiffness, strength, damage propagation and viscoelastic characteristics of the material itself. Mitigating the creep- and self-heating-related effects associated with frequency variation requires the definition of lower and upper frequency bounds, respectively, which in turn directly informs the selection of the target strain rate.

Therefore, similarly to Krieg, this study adopts a constant strain rate approach. Rather than fixing the frequency (f), the frequency for each test is calculated individually to maintain a consistent target strain rate across all stress levels and stress ratios. The specific loading frequency for each test is derived using the stiffness E, the stress ratio R, and the maximum applied stress, according to the following relationship:

$$f = \frac{\dot{\epsilon}_{target} \cdot E_{avg}}{2(1-R) \cdot \sigma_{max}}. \tag{4.2}$$

While the constant strain rate approach proposed by Lennart Krieg is well-suited for fibre-dominated laminates such as $[0/90]_{4s}$, its application to $\pm 45°$ laminates introduces a significant complication. In contrast to fibre-dominated configurations, $\pm 45°$ layups exhibit pronounced matrix- and shear-dominated behaviour, resulting in substantial stiffness degradation throughout fatigue life. This degradation fundamentally challenges the assumption of a constant strain rate. Although the loading frequency is selected based on the initial modulus to achieve a target strain rate, the progressive reduction in stiffness necessitates an increase in strain amplitude to maintain the imposed stress level. Consequently, the effective strain rate increases continuously as damage accumulates. This implies that the constant strain rate condition is only strictly satisfied at the onset of the test, after which the specimen experiences an evolving, and ultimately accelerating, deformation rate. The issue is particularly critical given that this increase in strain rate directly elevates the rate of energy input into the material, raising the risk of thermally driven failure mechanisms rather than the

intended mechanical fatigue processes. Figure 4.6b illustrates this evolution, modeled using the generalized stiffness degradation trend for GFRPs described by Ellyin and Kujawski [25], shown in Figure 4.6a.



(a) *Experimental stiffness degradation trend (Ellyin and Kujawski) [25]*

(b) *Strain rate evolution based on stiffness degradation model*

Figure 4.6: *Evolution of strain rate as a consequence of stiffness degradation in GFRP laminates.*

As shown, the strain rate begins at the target value of $0.05\,s^{-1}$ and gradually increases as the modulus drops, accelerating sharply towards the end of the fatigue life ($N/N_f \rightarrow 1$). By failure, the effective strain rate has increased significantly (approaching $0.09\,s^{-1}$ in the final cycles).

Feng et al. [48] show that the presence of ±45° laminates within the composite creates more shear-dominated, transverse matrix cracking, along with interlaminar stress resulting in the lack of the "sharp" transition points found in the more common three-stage degradation trend. This can be seen in Figure 4.7.

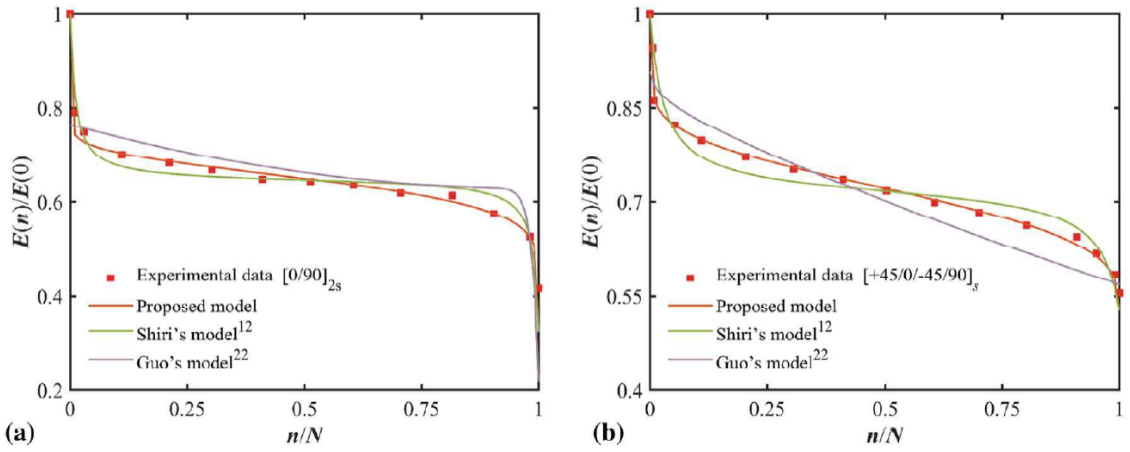


Figure 4.7: *Comparison of Normalized stiffness degradation between* $[0/90]_{2s}$ *(a) vs.* $[+45/0/-45/90]_s$ *(b) at the same stress level [48]*

This naturally leads to discussion on how the trend differs as stress levels vary. As the stress levels increase, the trends change from a smoother transition between damage regimes to a more identifiable larger gradient. In other words, at higher stresses, the trend may appear more continuously nonlinear rather than a clear distinction of the separate three stages.

The challenge becomes mitigating the progressive increase in strain rate resulting from stiffness degradation. Ideally, this would be achieved through continuous adjustment of the loading frequency throughout the test,

such that the target strain rate is maintained as the modulus evolves. However, the MTS fatigue system does not support real-time adaptive frequency control based on material response. As a practical alternative, a stepwise frequency adjustment strategy is implemented, where the test is divided into discrete cycle blocks, each assigned a predefined loading frequency. The key question then becomes the definition of these cycle intervals and corresponding frequency updates.

To address this, a simplified predictive framework should be established to output stiffness degradation trends as a result of the desired stress level. Establishing a general degradation trend, however, remains challenging, as even similar material systems exhibit different sensitivities to changes in stress levels, also just the absolute stiffness jumps within the same trend. Sartorio [41] highlights observing prominent fibre reorientation in the $\pm 45^\circ$ stacking sequence. Therefore, generalizing a predictive stiffness degradation model a priori may be inappropriate for the present material. Accordingly, the study will proceed with conducting initial fatigue tests under a constant frequency, which yields insight into the expected stiffness degradation trend for the material system corresponding to the current study.

Based on this, the initial loading frequency is determined from the target strain rate and the pristine modulus. Subsequently, the total frequency variation required to compensate for stiffness loss over the fatigue life is discretised into a finite number of steps. The number of steps is selected according to a prescribed allowable frequency increment, ensuring stable machine operation while limiting excessive deviations from the target strain rate. Finally, the resulting sequence of frequency values and corresponding cycle intervals is implemented directly within the MTS fatigue program as a block-wise loading schedule. Note that this approach is only applicable when the expected number of cycles to failure exceeds a certain limit that allows the PVC response within the machine to stabilize. For tests below this limit, attempting to use this approach would cause variable amplitude loading as the tests jump between cycle blocks, challenging the comparability of the overall results. Consequently, the high stress tests, below this limit, are expected to operate at a constant frequency throughout the test. Given the relative novelty of this testing approach, the identification of degradation trends, their subsequent modeling, and the selection of inputs for the proceeding tests were undertaken in an adaptive testing strategy, where observations from previous tests were used to design the following tests.

With the constant strain rate methodology established, the specific target value ($\dot{\epsilon}_{target}$) must be selected. This selection is constrained by three factors:

- **Lower Limit:** Lower frequencies result in higher time at peak load which allows for creep effects to take place.
- **Upper Limit:** Higher frequencies cause self-heating, which risks thermal failure, instead of mechanical failure.
- **Operational Limits:** The MTS machine has limits on the maximum frequencies it can operate at.

The following discussion identifies the range of frequencies that can be used for stress levels between 60 MPa and 120 MPa, while respecting limits imposed by creep, self-heating, and machine operability.

The lower bound of the operational frequency window is governed by creep-related effects. Perreux and Joseph [49] investigated the influence of frequency on the tensile–tensile fatigue behaviour of pressurized $\pm 55^\circ$ filament-wound E-glass/epoxy composite pipes. Their results showed that increasing the frequency from 0.2 to 1 Hz led to a consistent increase in fatigue life, expressed in cycles to failure, while little additional benefit was observed between 1 and 5 Hz. A comparison of strain evolution revealed that, despite similar strain amplitudes, both minimum and maximum strains were higher at lower frequencies. This behaviour was attributed to a matrix creep-dominated mechanism, whereby longer dwell times near peak load at low frequencies allow greater accumulation of viscoelastic and viscoplastic strain per cycle, accelerating damage. Based on these findings, a lower frequency limit of approximately 1 Hz can be identified for $\pm 55^\circ$ laminates. However, the $\pm 45^\circ$ lay-up considered in the present study is more shear-dominated and lacks a transverse normal stress component, making it more susceptible to creep effects. Consequently, a lower frequency limit of 1 Hz is adopted.

The upper frequency limit is primarily dictated by self-heating, which is a critical aspect especially with regard to matrix-dominated composites. Hülsbusch et al. [50] proposed an energy-based method for selecting fatigue test frequencies in PA6 by correlating the induced energy rate with the measured temperature rise during multiple frequency tests. In their approach, a limit frequency is defined as the frequency at which the

specimen temperature remains below a selected critical increase, taken as 2 K in their study. This limit is intended to avoid significant thermal softening, stiffness degradation, and premature thermal failure caused by excessive heat generation during cyclic loading. Ideally, the same multiple frequency test procedure should be applied directly to the present composite material to obtain a material- and stress-specific upper frequency limit. However, as will be discussed in the subsequent sections, the limited specimen sample size did not permit a systematic characterization of the upper limit according to Hülsbusch et al. [50]. Therefore, a standard upper limit of 5 Hz was adopted [51].

In addition to material-related constraints, the operational frequency range is further limited by the capabilities of the testing equipment. The upper frequency bound is also challenged by the limit imposed by the actuator velocity of the MTS 100kN machine. The question becomes: given a desired stress level and R-ratio, how fast should the actuator move and what is the maximum frequency limit accordingly?

The cyclic stress imposed onto the material on the machine follows a sinusoidal pattern which mathematically can be written as

$$\sigma(t) = \sigma_m + \sigma_a \sin(2\pi f t). \tag{4.3}$$

Assuming a preliminary linear elastic behavior following Hooke's law, then the strain as a function of time can be denoted as

$$\varepsilon(t) = \varepsilon_m + \varepsilon_a \sin(2\pi f t) \tag{4.4}$$

which differentiated would be

$$\dot{\varepsilon}(t) = 2\pi f \varepsilon_a \cos(2\pi f t). \tag{4.5}$$

Therefore, the maximum strain rate is Equation 4.5 at $\cos(2\pi f t) = 1$,

$$\dot{\varepsilon}_{\max} = 2\pi f \varepsilon_a = 2\pi f \frac{\sigma_a}{E}. \tag{4.6}$$

Given the effective clamp-to-clamp length L, then the required crosshead velocity is related as approximately

$$v_{\max,\text{required}} = L\dot{\varepsilon}_{\max} \qquad \Longrightarrow \qquad v_{\max,\text{required}} = 2\pi f L \frac{\sigma_a}{E} \tag{4.7}$$

which in turn rearranges to a maximum frequency that can be calculated using the following relation,

$$f_{\max} = \frac{v_{\max} E}{2\pi L \left[\frac{1-R}{2}\sigma_{\max}\right]}. \tag{4.8}$$

The maximum allowable actuator velocity of the MTS 100kN machine is 50 mm/s [52] and the effective clamp-to-clamp length is approximately 155 mm. Having established the lower limit concerning creep effects and upper limits addressing self-heating and machine operability, the next step is to determine feasible combinations of target strain rate and stress ratios over the expected stress range.

Monotonic tensile tests, discussed further in later chapters, provided estimates of the ultimate tensile strength for the present material system and therefore an indication of the appropriate stress range of 90 to 200 MPa. In addition, it was shown that both Equation 4.2 and Equation 4.8 require a stiffness modulus value. Ideally, a consistent initial strain rate across all fatigue stress levels is desired, which permits careful input of this value. Preliminary tests showed clear differences in the initial stiffness between specimens. A stress-dependent stiffness trend was later established from experimental data and used to predict the initial modulus per stress level. For the preliminary selection of target strain rate and stress ratios, a conservative modulus of 5000 MPa was used.

Using a stress range from 90 to 200 MPa and a stiffness modulus of 5000 MPa, a feasible operating region was evaluated, as shown in Figure 4.8, therefore settling on a target strain rate of 0.05 and possible stress-ratios from R=0.1 to R=0.7.

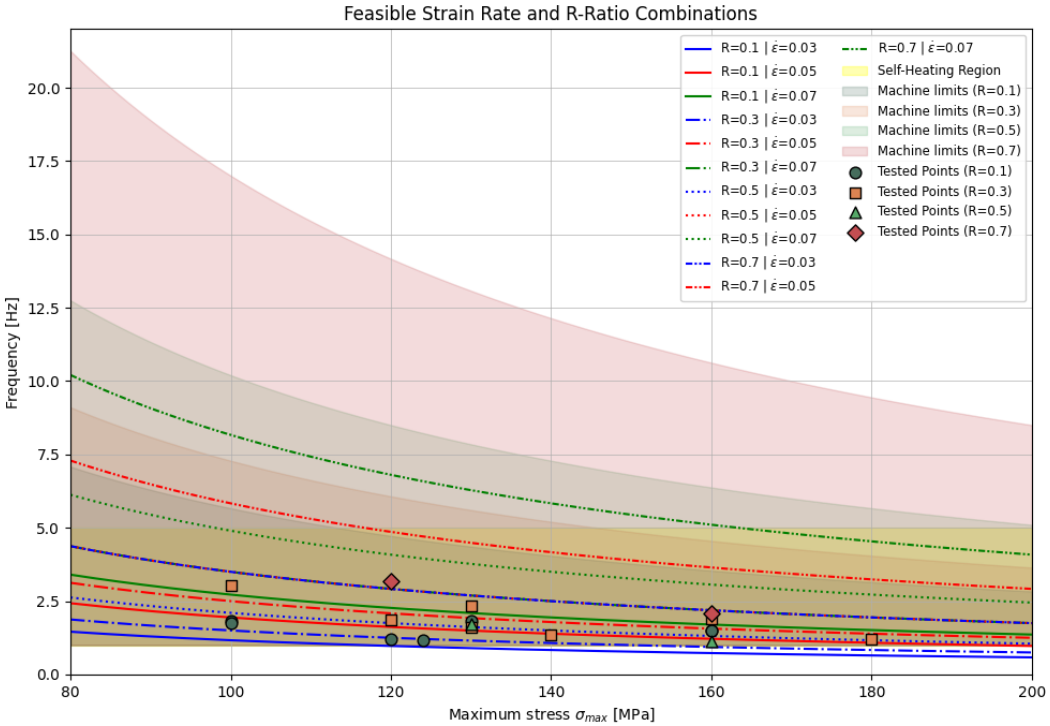


Figure 4.8: *Feasible combinations of strain rate and R-ratios, and consequent required frequencies for desired stress levels. The tested point markers indicate the experimental conditions evaluated at selected combinations of maximum stress, R-ratio and corresponding loading frequency.*

Overview of Loading Parameters

Table 4.3 presents the key loading parameters from the aforementioned discussion.

Table 4.3: *Summary of selected fatigue loading parameters.*

Parameter	Selected value / range
Target initial strain rate, $\dot{\varepsilon}_{\text{target}}$	0.05 s^{-1}
Stress ratios, R	0.1, 0.3, 0.5, 0.7
Strategy	Maintain constant initial strain across stress-levels. For HCF attempt strain rate control using MTS cycle blocks. Follow adaptive testing with progressive refinement.

4.2. Specimen Manufacturing and Preparation

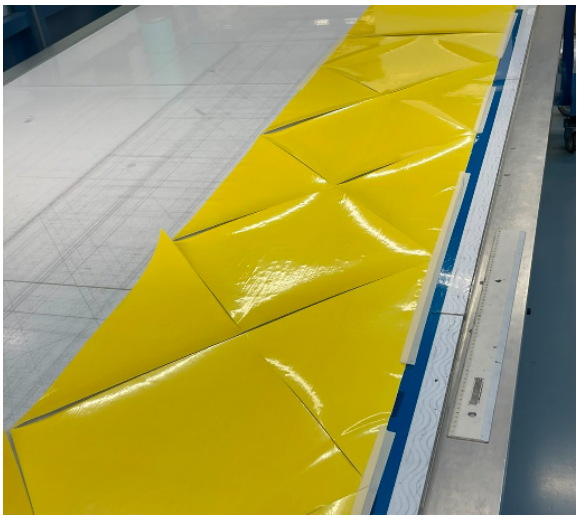
This section provides an overview of the main manufacturing process steps taken to create the final specimens required for the experimental campaign. Subsection 4.2.1 presents the main manufacturing steps to prepare the specimens, and Subsection 4.2.2 discusses the quality of the final specimens, and their distinct "textured" surface quality which should be acknowledged. Finally, the overview of the final specimens and their assigned testing campaigns is presented in Subsection 4.2.3.

4.2.1. Manufacturing Process

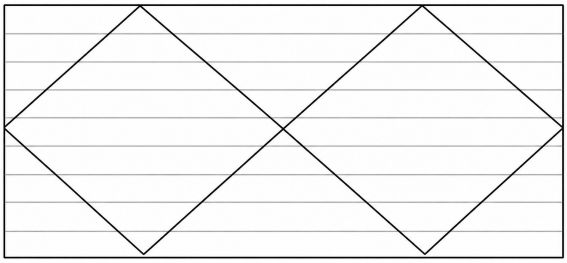
The section summarizes the main manufacturing steps taken to produce the ±45° specimens.

1. **Cutting the UD Prepreg Material.**

   The original pre-preg material, which is usually kept in the freezer, was left to defrost overnight prior to use. Since the material was supplied in a unidirectional fibre configuration, the following procedure was employed to produce the ±45° plies shown in Figure 4.9.



(a) Cutting manner in practice



(b) Cutting pattern

Figure 4.9: *Comparison of the practical cutting process and the corresponding cutting pattern.*

Different tests require different thicknesses, necessitating multiple laminates. The specimens for monotonic, stress-sweep, fatigue and creep tests require sixteen 848 x 848 mm plies of alternating ±45° layers. The tabs of those same specimens require ten plies. The DMA samples require twelve plies. The cutting was done on a GERBERcutter DCS machine. Once the plies were cut into their respective dimensions, they were stored in the freezer until further use to reduce further moisture absorption.

2. **De-bulking and lamination.**

   The next step of the manufacturing process is de-bulking in the lamination room. Every layered ply is ironed with a block of metal, before a three-minute de-bulking is performed to ensure adherence to the main plate and minimize air bubbles within the ply. This was performed with perforated release film and a peel ply layer for air path.

3. **Vacuum Bagging, Curing + Post-Curing**

   The vacuum bag system consists of the tooling plate/mould tool which is the big Aluminium base plate that provides the rigid base for the laminate layup and consolidation. The perforated release film is used with direct contact with the breather during the cure process. This also minimizes the level of voids. Thereafter, the peel-ply is used along with breather fabric ensuring it reaches the vacuum valves. A standard nylon vacuum bag was generously used, ensuring no bridging of the film which could cause the bag to burst in the autoclave. This was vacuum sealed using Black LST90B Tacky Tape. This can be seen in Figure 4.10.

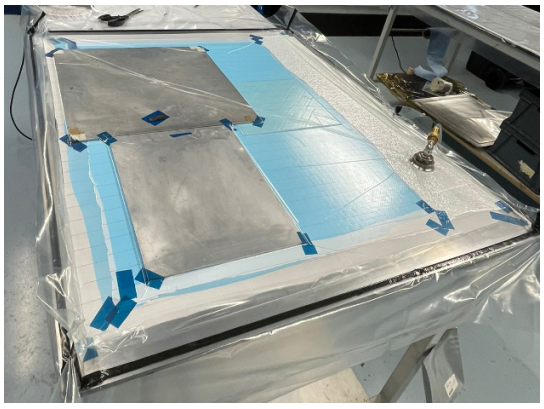


Figure 4.10: *Vacuum Bag Set-Up Prior to Autoclave curing cycle.*

The curing cycle used for the laminates is as follows,

Table 4.4: *Curing cycle steps and specifications.*

Step	Specification	Duration [hrs]
Initial ramp RT–80 °C	2 °C/min	0.5
Dwell	80 °C	12
Post-cure ramp 80–120 °C	0.33 °C/min	2
Post-cure dwell	120 °C	1
Cooldown 120–60 °C	−2 °C/min	0.7
Total curing time		**16–16.5**

4. **Compcut Cutting and Machining.**

   The CompCut ACS 600 CNC diamond-blade water-cooled circular saw cut the specimens after the curing cycle. The DMA specimens were ready for testing, however the specimens required for the other experimental tests were handed into the DEMO shop to construct the Double-Euler specimen geometries.

5. **Tab preparation.**

   The tab material was cut to the designated geometry shown in Figure 4.4, after which a taper angle was applied. The bonding of the tabs consisted of using Loctite AE3430 two-component structural adhesive. The bonding surfaces were ground with 300-grit sandpaper and cleaned with isopropanol. Thereafter, the tabs were bonded using 200 μm glass beads. Finally, they were put in the oven at 50$^{\circ}C$ for 2 hours. The bonded tabs prior to oven curing are shown in Figure 4.11.

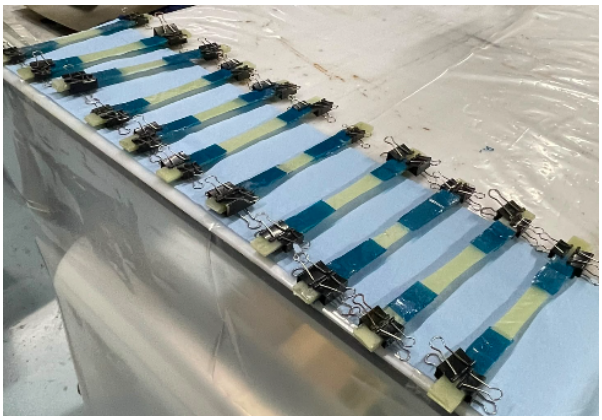


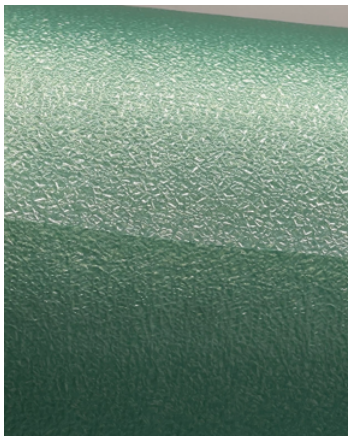
Figure 4.11: *The clamping of the tabs bonded onto the specimens, prior to oven.*

4.2.2. Specimen Quality

The release foil used during the de-bulking stage caused some premature curing into the prepreg which was imprinted onto the final specimens, seen in Figure 4.12. This raises the question of specimen usability. However, it could be argued that if the same textured specimens are fed into the proposed framework, then if the physics holds, the model should still yield consistent outputs. However from this point onward, the limited sample size constitutes an obstacle that requires careful consideration when assigning specimens to their respective tests.



(a) Textured specimen



(b) Release-foil responsible for the print.

Figure 4.12: *Surface texture imprinted on the specimen during processing, showing (a) the textured specimen surface and (b) the release-foil texture responsible for the transferred imprint.*

4.2.3. Overview of Final Specimens

Given the limited number of available specimens, Table 4.5 presents the final specimen set and their assigned testing campaigns.

Table 4.5: *Measured Coupon Dimensions for the Different Mechanical Tests.*

Test	Coupon ID	Gauge width			Thickness			Length		
		Top	Middle	Bottom	Top	Middle	Bottom	Gauge	Total	
Monotonic Tensile	1.1	24.02	16.73	23.86	6.22	3.09	6.03	6.00	155.00	51.70
	1.2.1	24.20	16.72	24.03	6.37	3.19	6.33	6.00	154.83	53.34
	1.2.2	23.49	16.85	23.58	6.74	3.10	6.54	6.00	155.72	52.24
Stress Sweep Test	2.1	24.09	16.71	23.79	6.10	2.87	6.37	6.00	155.77	49.88
	2.2	24.85	17.31	23.90	6.11	2.93	6.51	6.00	155.70	50.72
Fatigue Tests at $R = 0.1$	3.1	24.05	16.65	23.60	6.69	2.95	5.96	6.00	156.00	49.12
	3.2	23.06	16.59	23.56	6.50	2.92	7.00	6.00	156.00	48.44
	3.3	24.13	16.40	23.22	6.39	2.89	6.44	6.00	156.00	47.40
	3.4	23.20	16.60	23.51	6.11	2.78	6.01	6.00	156.00	46.15
	3.5	23.29	16.61	23.19	6.04	2.84	5.85	6.00	156.00	47.17
	3.6	23.79	17.04	24.60	5.95	2.90	6.22	6.00	156.00	49.42
	3.7	23.40	16.55	23.97	6.17	2.85	6.04	6.00	156.00	47.17
Fatigue Tests at $R = 0.3$	4.1	23.88	16.65	24.49	6.00	2.92	6.33	6.00	156.00	48.62
	4.2	23.09	16.77	23.61	6.06	2.86	6.11	6.00	156.00	47.96
	4.3	24.50	16.63	23.65	6.18	2.85	6.48	6.00	156.00	47.40
	4.4	23.85	16.53	24.09	6.11	2.93	6.05	6.00	156.00	48.43
	4.5	24.14	16.68	23.90	6.31	2.96	6.10	6.00	156.00	49.37
	4.6	23.96	16.63	23.80	6.56	2.95	6.51	6.00	156.00	49.06
	4.7	24.11	16.40	24.08	5.95	3.03	6.36	6.00	156.00	49.69
Fatigue Tests at $R = 0.5$	5.1	23.26	16.58	24.40	6.01	3.00	6.59	6.00	156.00	49.74
	5.2	24.21	16.51	24.34	6.44	2.95	6.29	6.00	156.00	48.70
Fatigue Tests at $R = 0.7$	6.1	24.04	16.75	24.24	5.99	2.86	6.07	6.00	156.00	47.91
	6.2	24.03	16.60	23.86	6.46	2.90	6.38	6.00	156.00	48.14
Creep Test	7.1	23.74	16.68	24.22	6.31	2.78	6.27	6.00	156.00	46.37

4.3. Experimental Procedures and Equipment

Building on the established experimental design and loading strategy, this section describes the five principal testing procedures: monotonic tensile testing, stress-sweep testing, constant amplitude fatigue testing, creep and recovery testing and dynamic mechanical analysis (DMA) which can be found in Subsection 4.3.1,Subsection 4.3.2, Subsection 4.3.3, Subsection 4.3.4 and Subsection 4.3.5, respectively. Each subsection presents the purpose of that specific test identifying the key quantities required to answer the research questions. Thereafter, how the experimental method used to obtain these parameters discussed, along with the exact machines and relevant programs used.

4.3.1. Monotonic Tensile Testing

Monotonic tensile tests characterize the strain-rate dependent tensile response of the $[\pm 45]_{4s}$ composite. The quantity of interest is ultimate tensile strength (UTS), which helps answer Research Question 6 and also functions as input information for designing the appropriate stress levels of stress-sweep testing and constant amplitude fatigue testing. The peak of the stress-strain curve yields this value.

Firstly, one specimen was tested at a quasi-static (QS) rate of 2 mm/min. Thereafter, the UTS value from this was used to iterate the appropriate stress range in the target strain rate selection plot Figure 4.8 in Subsection 4.1.3. Once the desired target strain rate of 0.05/s was established, two specimens were tested at a displacement rate equivalent to a strain rate of 0.05/s. This was calculated as follows

$$\dot{\delta} = L\dot{\varepsilon} = 156 \cdot 0.05 = 7.8 \text{ mm/s} = 468 \text{ mm/min}, \tag{4.9}$$

where L is the clamp-to-clamp length of 156 mm, established once the specimen was clamped onto the machine.

Tensile, stress-sweep, constant amplitude fatigue and creep tests were all performed on the MTS 100kN servo-hydraulic test machine which uses hydraulically actuated wedge grips (Figure 4.13), consistent with the experimental setup used by Krieg as well.

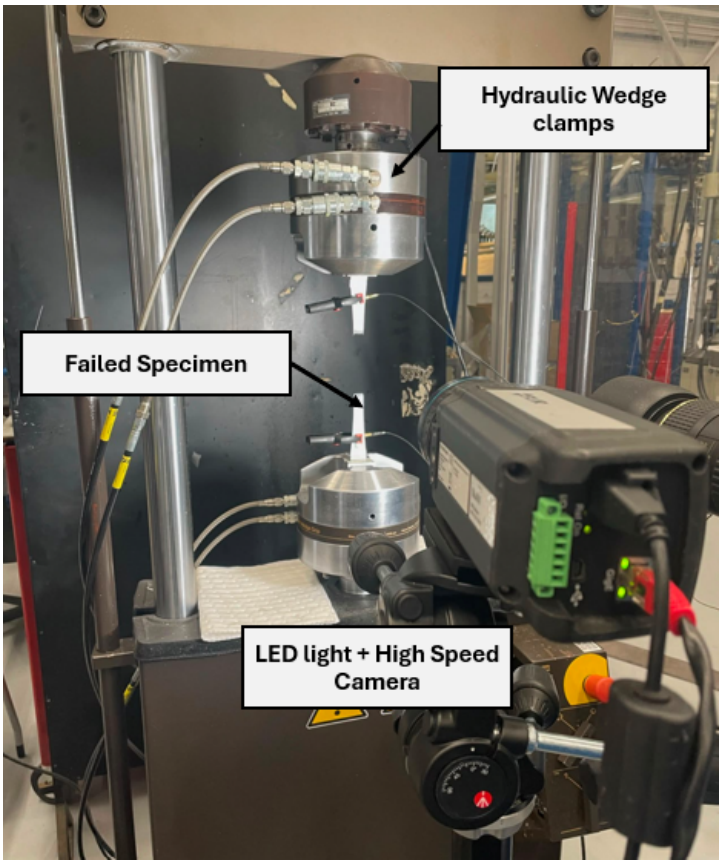


Figure 4.13: *MTS 100kN Servo-Hydraulic machine used for tensile, SST, CA Fatigue and Creep tests.*

4.3.2. Stress-Sweep Testing

Stress-sweep testing addresses research questions 3 and 5, on the slope determination and fatigue limit respectively. This requires the ratio of total dissipated energy over total applied work TDE/W_{tot} for each successive stress block. The cycle stress-strain data are separated into their individual hysteresis loops per cycle, from which the dissipated energy and total applied work are calculated. These quantities are then summed over the corresponding stress block to determine the ratio for that corresponding stress level.

The stress-sweep test starts at 20% of the fatigue-equivalent ultimate tensile strength (FE UTS), obtained from the monotonic tensile tests. The initial stress level was selected to be sufficiently low to minimize likelihood of high damage, staying below the onset of damage and therefore allowing two distinct linear regimes and a resulting deviation point. Every following stress level was increased in increments of 5% UTS, with each stress level programmed to run for 1000 cycles, which is consistent with Sartorio. This stepwise sequence is programmed until the specimen fails. The procedure was performed twice for stress-ratios R=0.1 and R=0.3. The corresponding stress levels and frequencies required to maintain a target strain rate of 0.05 /s for each cyclic stress block are presented in Table 4.6. Although a nominal upper frequency of 5 Hz was adopted as the upper limit when selecting a target strain rate, given that it is the lowest stress level of the entire sweep, the self-heating effect was not expected to be significant.

Table 4.6: *Stress-sweep loading programmes for* $R = 0.1$ *and* $R = 0.3$.

$R = 0.1$				$R = 0.3$			
Block	**UTS (%)**	σ_{max}	f **(Hz)**	**Block**	**UTS (%)**	σ_{max}	f **(Hz)**
1	20	45.48	4.762	1	20	45.48	6.123
2	25	56.85	3.810	2	25	56.85	4.898
3	30	68.22	3.175	3	30	68.22	4.082
4	35	79.59	2.721	4	35	79.59	3.499
5	40	90.96	2.381	5	40	90.96	3.061
6	45	102.33	2.117	6	45	102.33	2.721
7	50	113.70	1.905	7	50	113.70	2.449
8	55	125.07	1.732	8	55	125.07	2.226
9	60	136.44	1.587	9	60	136.44	2.041
10	65	147.81	1.465	10	65	147.81	1.884
11	70	159.18	1.361	11	70	159.18	1.749
12	75	170.55	1.270	12	75	170.55	1.633
13	80	181.92	1.191	13	80	181.92	1.531
14	85	193.29	1.121	14	85	193.29	1.441
15	90	204.66	1.058	15	90	204.66	1.361
16	95	216.03	1.003	16	95	216.03	1.289

4.3.3. Constant Amplitude Fatigue Testing

The constant-amplitude fatigue testing was the largest experimental campaign where its cyclic stress-strain data allowed for determination of metrics such as stiffness degradation, cyclic creep rate, dissipated energy and applied energy, which address Research Question 1. The number of cycles to failure Nf per stress level is used to make S-N curves which serve as both input data for R1, and validation data for R2. This is the starting point to answer research questions 2, 3, 4 and 5.

For R=0.1, fatigue tests were conducted at 80%, 65%, 62%, 60%, and 50% of the fatigue-equivalent UTS. The stress levels were selected progressively to obtain a sufficiently broad range of fatigue lives, spanning approximately from 10^1 to 10^6 cycles. A run-out criterion of 10^6 cycles was adopted due to the experimental time constraints of the thesis. For R=0.3, tests were performed at 90%, 80%, 70%, 65%, 60%, and 50% UTS. For the higher stress ratios, a reduced number of stress levels was investigated: 80% and 65% UTS for R=0.5, and 80% and 60% UTS for R=0.7. Greater experimental coverage was allocated to R=0.1 and R=0.3, as these datasets were of primary importance for model development and validation. At higher stress ratios, the reduced cyclic stress amplitude at a given maximum stress generally results in longer fatigue lives, making extensive testing considerably more time-consuming.

Two frequency-control approaches were employed during the constant-amplitude fatigue campaign. Some

specimens were tested at a constant frequency corresponding to the prescribed initial strain rate, while others were tested using a stepwise frequency-adjustment strategy intended to better maintain the target strain rate as stiffness degradation progressed. The required frequency adjustments were determined either from repeated tests conducted at the same stress level or by interpolation between previously established degradation trends, following the procedure described in Subsection 4.1.3. The tested stress-levels, frequencies and R-ratios are in Table 4.7.

Table 4.7: *Fatigue test conditions for the different stress levels and stress ratios.*

$R = 0.1$		$R = 0.3$	
Stress Level (% UTS)	**Frequency (Hz)**	**Stress Level (% UTS)**	**Frequency (Hz)**
80	1.479	90	1.222
80	1.479	80	1.901
65	1.820	70	1.364–1.695
62	1.157–1.091	65	2.340
60	1.216–1.142	65	1.590–1.893
50	1.809–1.580	60	1.848–2.071
50	1.735	50	3.042
$R = 0.5$		$R = 0.7$	
Stress Level (% UTS)	**Frequency (Hz)**	**Stress Level (% UTS)**	**Frequency (Hz)**
80	1.144	80	2.071
65	1.713	60	3.194

An example of a MTS 100kN program can be found in Table 4.8 for 65% UTS R=0.3, and the stiffness degradation trend on which it was based is shown in Figure 4.14.

Table 4.8: *MTS MPT programming sequence for 65% UTS at* $R = 0.3$.

Block	**Cycles**	f **(Hz)**	**Cumulative Cycles**
1	100	1.590	100
2	200	1.677	300
3	300	1.727	600
4	500	1.783	1100
5	1000	1.843	2100
6	2000	1.891	4100
7	5000	1.919	9100
8	5000	1.929	14100
9	5000	1.929	19100
10	5000	1.919	24100
11	2635	1.893	26735

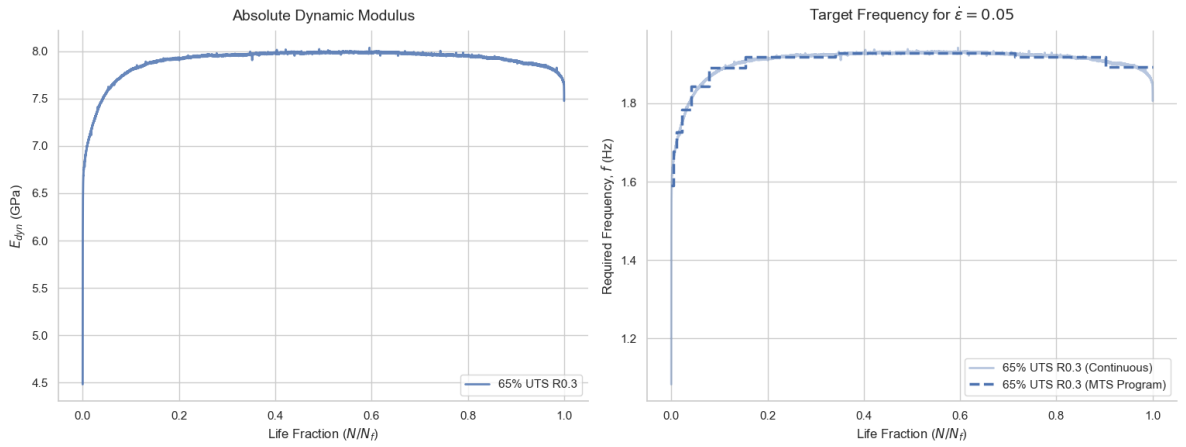


Figure 4.14: *Stiffness degradation at 65% UTS and $R = 0.3$, and the corresponding target loading frequency required to maintain the prescribed strain rate.*

4.3.4. Creep and Recovery Testing

Isothermal, uniaxial creep and recovery tests were used to obtain the strain response at different stress levels required for determination of the nonlinear viscoelastic model parameters and, subsequently, the augmentation parameter Ψ addressing Research Question-02.

Prior to the main creep-recovery program, the specimens were mechanically conditioned. Schapery employed a substantially longer conditioning procedure which consisted of one-hour creep and one-day recovery, for ten days. Due to the time constraints of the present study, an alternative shortened conditioning procedure was adopted, as illustrated in Figure 4.15 [53].

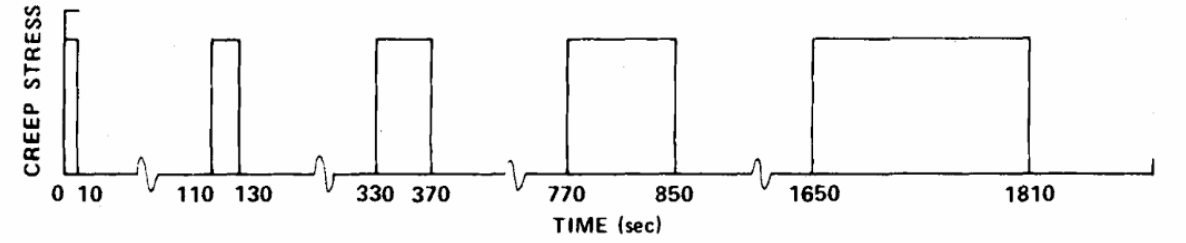


Figure 4.15: *Program for Mechanically Conditioning*

The final conditioning step was repeated until the measured strain response became approximately repeatable between consecutive cycles, indicating satisfactory mechanical conditioning. A maximum conditioning stress of 100 MPa was selected to correspond to the highest stress level intended for the creep tests.

Since the creep-recovery programme was conducted after the constant-amplitude fatigue campaign, the available fatigue results were first examined to identify a stress level that could be sustained for a sufficiently long duration without premature specimen failure. Particular attention was given to stress levels associated with fatigue lives exceeding approximately two hours of loading, from which a conservative upper creep stress of 100 MPa was selected. The tests were conducted at an elevated temperature of approximately 73°, following the temperature used in Schapery's experimental procedure as closely as practical. Owing to the temperature regulation of the available thermal chamber, the actual test temperature fluctuated within approximately $70° - 73°$.

During the main creep-recovery test, each prescribed stress level consisted of a one-hour creep period followed by a two-hour recovery period. The loading sequence began at a sufficiently low stress level to establish an approximately linear viscoelastic response, which is required for the model-parameter identification procedure described in Section 3.2. Similar to the stress-sweep program, the creep sequence was defined using progressively increasing stress levels from 20% to 85% of the selected reference strength. The programme was

intentionally defined beyond the stress level expected to be reached experimentally, since specimen failure was anticipated before completion of the full sequence. Two specimens were tested using this procedure. The specific stress levels applied are summarized in Table 4.9.

Table 4.9: *Creep testing conditions for specimens 7.1 and 7.2.*

Condition	% UTS	Stress (MPa)	Load - 7.1 (N)	Load - 7.2 (N)
Mechanical conditioning	–	100.00	4637.00	4765.80
Creep/Recovery Testing	20	45.48	2108.926	2167.486
	25	56.85	2636.157	2709.357
	30	68.22	3163.389	3251.229
	35	79.59	3690.620	3793.100
	40	90.96	4217.852	4334.972
	45	102.33	4745.083	4876.843

Due to the tests conducted at an isothermal $73°C$, the creep-recovery experiments were performed using the Zwick 200kN test machine equipped with a thermal chamber, as shown in Figure 4.16. Strain gauges were bonded to both sides of the specimen gauge section to measure the longitudinal strain response and to maintain consistency with the measurement approach adopted in Schapery's experimental procedure.

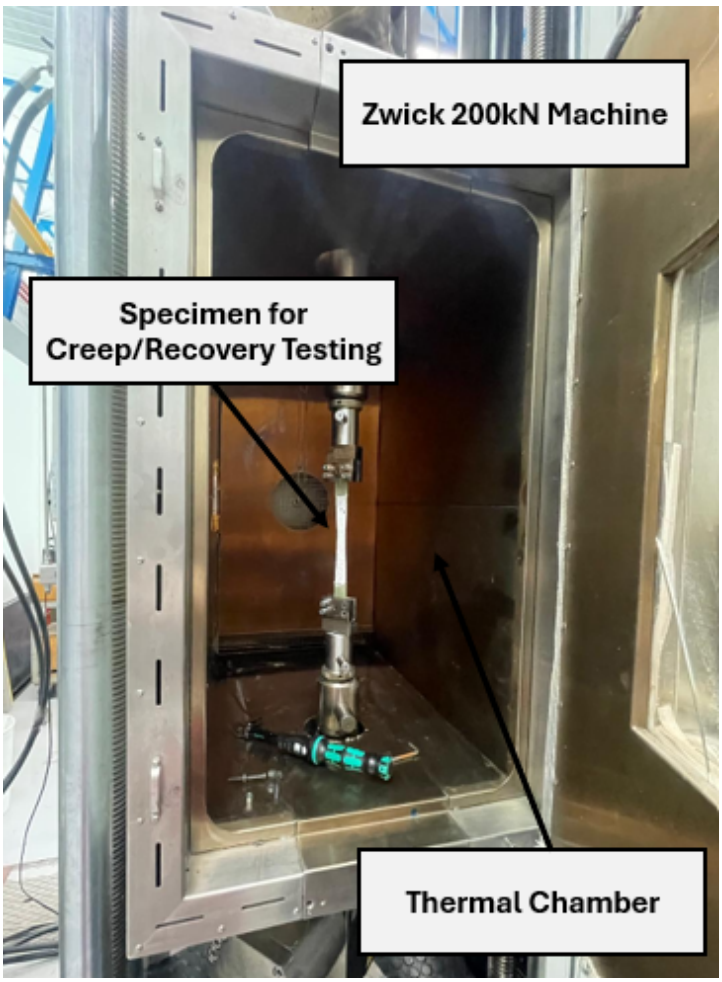


Figure 4.16: *Zwick 200 kN mechanical testing setup equipped with a thermal chamber and specimen arrangement for creep/recovery testing.*

4.3.5. Dynamic Mechanical Analysis

Dynamic Mechanical Analysis (DMA) was performed using a TA Instruments RSA-G2 analyzer, as shown in Figure 4.17. The system permits relatively low applied forces, with a maximum force capacity of approximately 35 N. This load limitation makes tensile testing of comparatively stiff fibre-reinforced polymer specimens impractical. The DMA specimens were therefore tested in flexure using a three-point-bending (3PB) configuration.

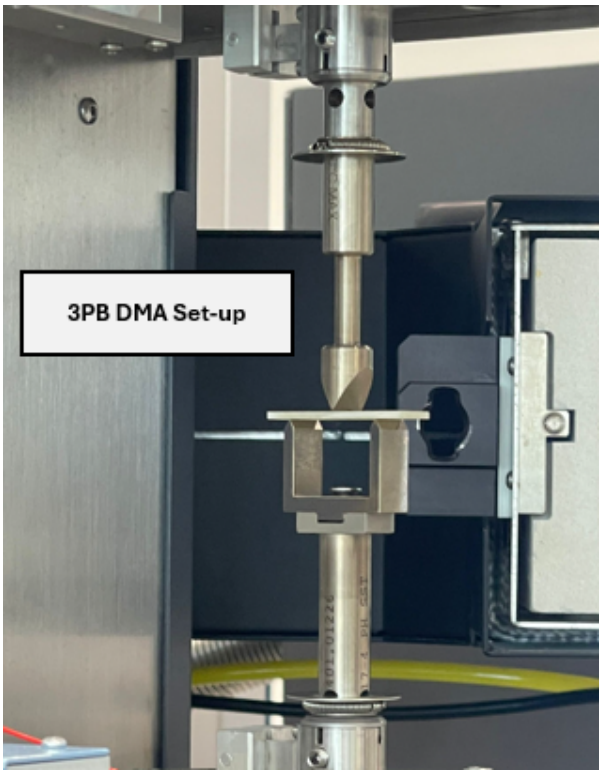


Figure 4.17: *3PB configuration on TA Instruments RSA-G2 solids analyser for DMA Testing.*

The principal quantity of interest from the DMA testing was the pristine loss factor, which is subsequently used in the determination of the high-cycle fatigue strength (HCFS). The loss factor was obtained through a temperature-sweep test extending from approximately room temperature $25^\circ - 30^\circ$ to 160°. Ideally, multiple specimens would have been tested under different bending configurations while reproducing, as closely as possible, the stress ratios and target strain rate of 0.05 /s used in the fatigue programme. However, reproducing this strain-rate condition would have required excitation frequencies beyond the practical operating range of the DMA system, whose usable frequency was limited to approximately 10 Hz before resonance effects became significant.

A further limitation was that the DMA system was not configured for direct load-controlled cycling in the same manner as the servo-hydraulic fatigue machines. Instead, the primary control input was the imposed strain amplitude, corresponding to the maximum cyclic deformation of the specimen. Consequently, the fatigue loading conditions could not be replicated directly. In addition, equipment failure restricted the experimental campaign to a single successful DMA test. The corresponding test conditions are summarized in Table 4.10.

Table 4.10: *DMA test parameters.*

Test ID	Mode	Frequency (Hz)	ε_{max} (%)	ε_{min} (%)	R-ratio
DMA-1	3PB	3	0.1	0.01	0.1

5 Results, Discussion and Limitations

This chapter presents the results obtained from the experimental campaign and is structured to allow the findings to be interpreted directly in relation to the research questions.

Section 5.1 begins with a general exploratory assessment of the ±45° laminate response, especially the fatigue metrics that provide the basis for addressing Research Question-01. The slope constituent of the S-N curve is then explored in Section 5.2, which covers the creep-recovery test analysis and stress-sweep test analysis, assessing whether they can predict the slope of the S-N curve, addressing Research Questions -02 and -03. The bottom anchor is subsequently explored in Section 5.3 through DMA and stress-sweep results, addressing Research Questions -04 and -05. Finally, the upper anchor is evaluated in Section 5.4, addressing Research Question-06. While the preceding sections discuss the S-N curve constituents separately, Section 5.5 brings these findings together and discusses their integration within a unified fatigue-life prediction approach. To conclude the chapter, Section 5.6 summarises the main limitations within the results.

5.1. General Observed Behavior

In this section, the physical observations of the ±45° are presented and discussed, with the aim of answering Research Question-01 in Subsection 5.1.8. The rate-dependent stress-strain responses from the monotonic tensile tests are presented in Subsection 4.3.1. Subsection 5.1.2 presents a summary of the fatigue test results, prior to post-processing. Relevant metrics, acquired from the cyclic stress-strain hysteresis loop, such as stiffness degradation, strain progression, dissipated energy, applied energy and the resulting loss factor are investigated in Subsection 5.1.3, Subsection 5.1.4, Subsection 5.1.5, Subsection 5.1.6 and Subsection 5.1.7, respectively.

5.1.1. Monotonic Tensile Test Results

Monotonic Tensile Tests were performed on three specimens; one at quasi-static displacement rate of 2 mm/min, and two at the fatigue-equivalent dynamic displacement rate of 7.8 mm/s. The stress-strain responses of the three specimens are shown in Figure 5.1.

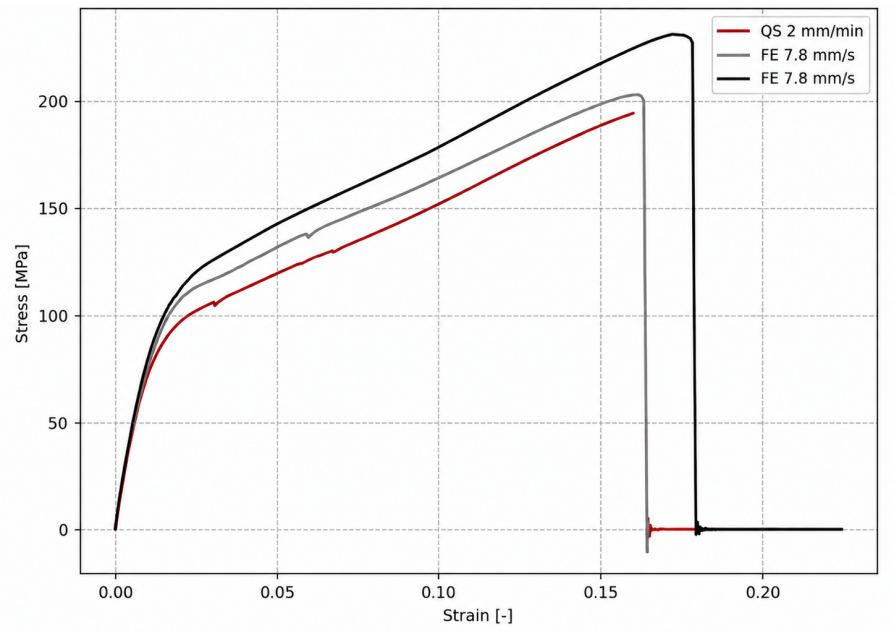


Figure 5.1: *Monotonic Tensile test results at quasi-static (QS) 2 mm/min and fatigue-equivalent (FE) 7.8 mm/s*

Figure 5.1 depicts a two-stage response where the transition between the first linear regime and second quasi-linear regime is initiated by the influence of re-orientation of the ±45° fibres.

Fibre re-orientation is defined as the progression realignment of the fibres relative to the loading direction, as a result of the load. The rotation of the fibres increases the effective stiffness, which is shown in the second quasi-linear regime. This re-orientation angle can be calculated given the gauge strains in the y and x

direction; ϵ_{yy} and ϵ_{xx}, respectively [54].

$$\theta_f = 90 - \arctan\left[\tan\theta_0\left(\frac{1+\varepsilon_{yy}}{1+\varepsilon_{xx}}\right)\right] \tag{5.1}$$

where θ_0 is 45°. This is plotted as a function of the strain for each of the three specimens in Figure 5.2.

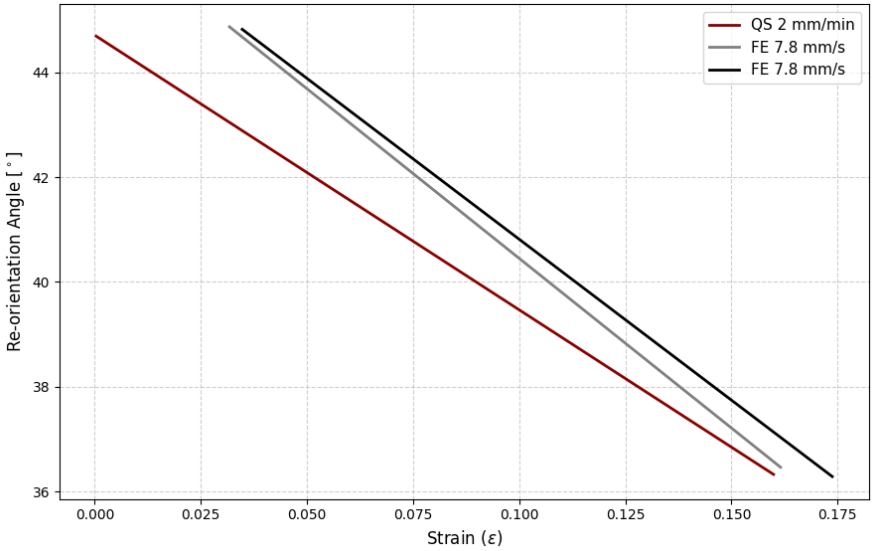


Figure 5.2: *Re-orientation Angle vs. Strain for monotonic tensile tests.*

Figure 5.2 shows that the initial point where re-orientation begins coincides with the transition between the two linear regimes in the stress-strain curves Figure 5.1. All three specimens display a re-orientation from 45° to ≈ 36° − 37° which is a substantial increase in effective stiffness and is clearly seen in Figure 5.1.

The fatigue-equivalent dynamic rate tests show a 4.4% - 18.8% increase in ultimate tensile strength (UTS) and a 2.0% - 11.4% increase in the failure strain. Even though an increase in these parameters was expected, the two specimens show a large range. Based on qualitative observations, specimen FE_1 was considered potentially unreliable. Hereafter, specimen FE_2 was used as the representative fatigue-equivalent reference data-point. However, an important remark is the sensitivity of the fatigue-equivalent stress-strain responses to variables in manufacturing differences, alignment/positioning on the MTS machine and pre-existing defects which result in a fairly large range for the UTS and failure strains.

5.1.2. Overview of General Fatigue Performance

Table 5.1 summarizes the measured cycles to failure, time to failure and final failure strain for the corresponding stress-levels and R-ratios. Given the hypothesized greater contribution of time-dependent mechanisms in ±45° laminates, the time-to-failure T_f is also a relevant metric to evaluate.

Table 5.1: *Fatigue test results for different stress ratios.*

$R = 0.1$					$R = 0.3$				
UTS (%)	σ_{max} (MPa)	N_f	T_f (s)	ε_{fail}	**UTS** (%)	σ_{max} (MPa)	N_f	T_f (s)	ε_{fail}
80	181.92	59	40.46	0.140	90	204.66	39	33.54	0.181
80	181.92	68	47.54	0.151	80	181.92	132	70.96	0.139
65	147.81	398	219.76	0.140	70	159.18	2558	1541.86	0.126
62	140.988	3599	3184.63	0.111	65	147.81	26737	11426.63	0.121
60	136.44	11936	10398.73	0.115	65	147.81	110921	58496.01	0.119
50	113.70	175567	101216.95	0.081	60	136.44	64515	31105.40	0.108
50	113.70	73440	44819.80	0.091	50	113.70	$>10^6$	-	-
$R = 0.5$					$R = 0.7$				
UTS (%)	σ_{max} (MPa)	N_f	T_f (s)	ε_{fail}	**UTS** (%)	σ_{max} (MPa)	N_f	T_f (s)	ε_{fail}
80	181.92	1412	1236.03	0.140	80	181.92	10129	4892.31	0.152
65	147.81	$>10^6$	-	-	60	136.44	$>10^6$	-	-

All the specimens failed in the specimen gauge section confirming the advantage of the Double-Euler geometry. The results discussed hereafter refer to the cyclic stress-strain responses from each of the specimens at their respective stress-level and R-ratio. An example is shown in Figure 5.3.

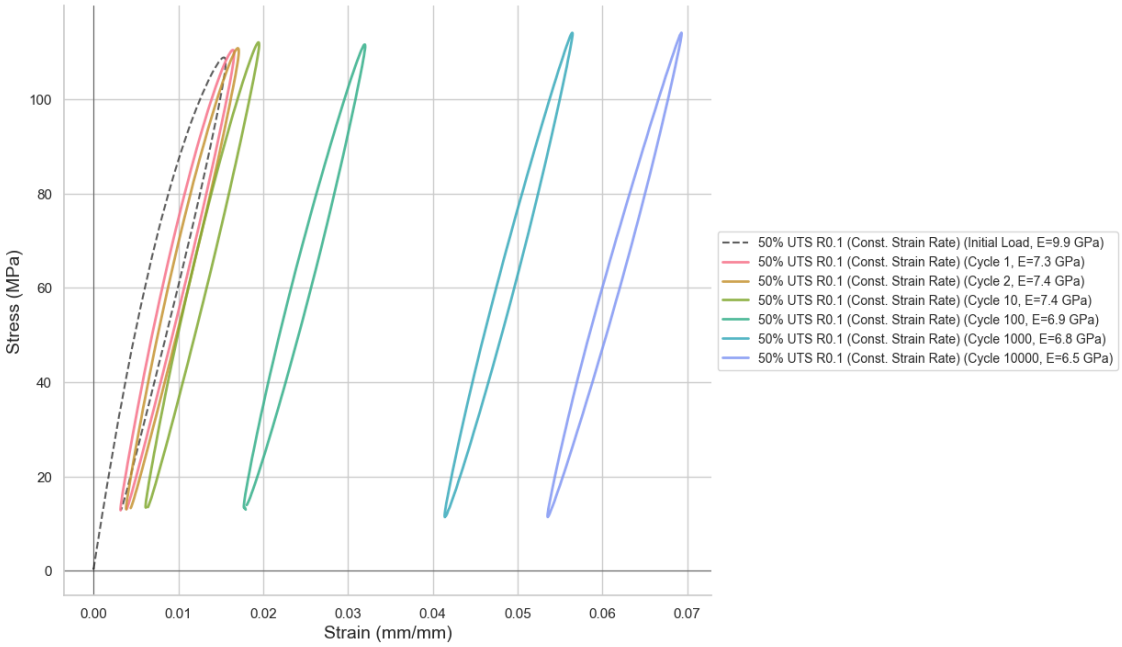


Figure 5.3: *Cyclic Stress-Strain Data resulting in Hysteresis Loops (50% UTS R=0.1).*

The slope of the hysteresis loop represents the stiffness at the corresponding cycle number. The progressive horizontal shift of this hysteresis loop is the ratcheting strain, while the area inside the loop refers to the dissipated energy. The applied energy refers to the total work input during the loading cycle, encompassing both the dissipated energy and the recoverable energy represented by the area beneath the loop. For consistency throughout figures, the R-ratios 0.1, 0.3, 0.5 and 0.7 are plotted in colors blue, orange, purple and green, respectively.

5.1.3. Stiffness Evolution

The stiffness progression during a testing cycle is evaluated by the slope of the hysteresis stress-strain loop, and calculated as follows

$$\left|E_i^*\right| = \frac{\sigma_{\max,i} - \sigma_{\min,i}}{\varepsilon_{\max,i} - \varepsilon_{\min,i}}. \tag{5.2}$$

The stiffness evolution trends for the different stress-levels and R-ratios are shown in Figure 5.4.

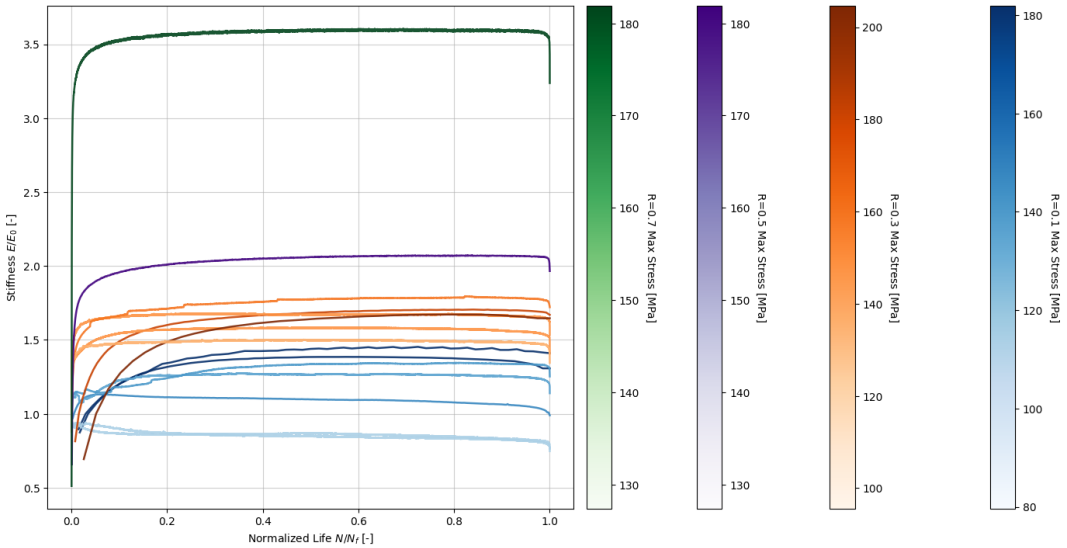


Figure 5.4: *Stiffness Degradation E/E_0 over the Normalized fatigue lives. For the exact stress levels and corresponding test conditions, refer to the test matrix in Table 4.7.*

For the exact stress levels and corresponding test conditions represented in Figure 5.4, refer to the test matrix in Table 4.7. As seen in Figure 5.4, the stiffness shows a common trend of rapid increase at the start of the test, and followed by either a stabilization or gradual decay depending on the stress level. The stiffness response generally exhibits an initial increase followed by stabilization and, at sufficiently long fatigue lives, a subsequent gradual decline. This latter stage is more apparent at lower stress levels, whereas specimens subjected to higher stresses tend to fail before a distinct stiffness-decay regime can develop.

The initial rapid increase in stiffness is again associated with fibre re-orientation. For example, for the 80% UTS specimen at R=0.1, Figure 5.5 shows the re-oriented fibre angle progressions from 45° to approximately 39°, till 15% of the normalized life, which coincides with the stiffness evolution trend seen in Figure 5.3.

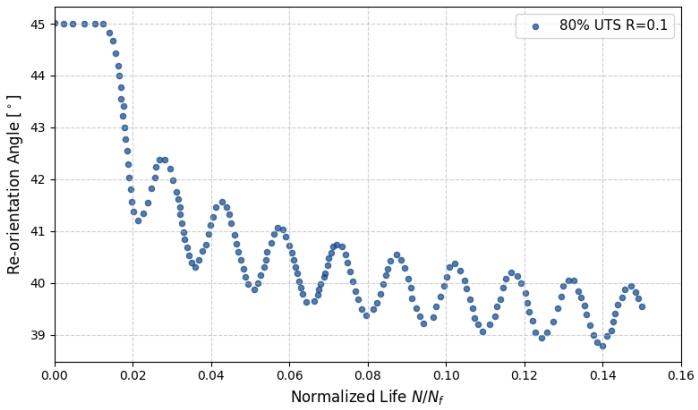


Figure 5.5: *Re-orientation Angle vs. Strain for 80% UTS R=0.1 Fatigue Test.*

Directly proportional to the stiffness is the strain rate, which forms the next point of discussion. Contrary to the hypothesized pronounced strain rate evolution as a result of stiffness degradation, it shows that, past the

re-orientation stage the stiffness remains fairly stable. This suggests that the associated evolution in strain rate may be less severe than initially anticipated, thereby calling into question the necessity of continuously adjusting the loading frequency to maintain a constant strain rate throughout the test.

Instead, more attention should be given to maintaining a consistent initial strain rate across specimens should be present. This remains challenging since the initial stiffness does not correlate to the pristine stiffness values from the monotonic tests (Figure 5.1), and adding to the complexity, the prescribed strain rate evolves almost immediately after loading begins due to re-orientation. In conclusion, the difficulty was initially misattributed to strain-rate evolution throughout fatigue life, whereas the results indicate that the greater challenge lies in establishing a consistent initial strain-rate condition. This is reflected in the strain rate evolution shown in Figure 5.6.

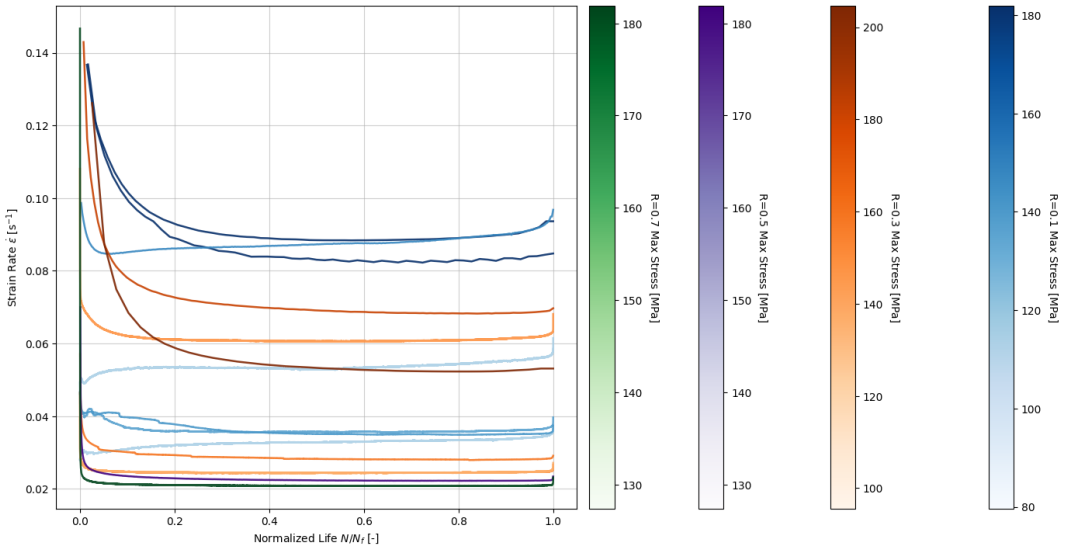


Figure 5.6: *Strain-Rate Evolution over the normalized fatigue lives. For the exact stress levels and corresponding test conditions, refer to the test matrix in Table 4.7.*

Another point of interest is the R-ratio dependence. The stabilized average stiffness value is plotted against the corresponding stress level in Figure 5.7.

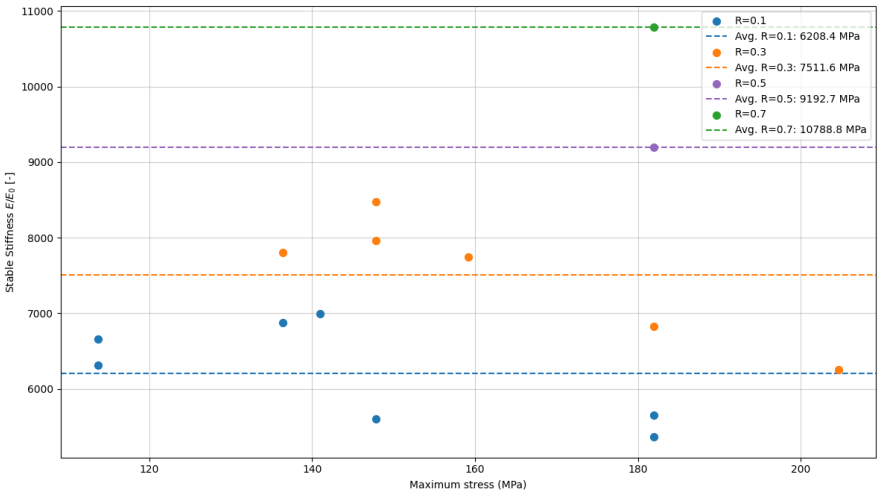


Figure 5.7: *Average Stabilized Stiffness Values across stress-levels and R-ratios.*

Figure 5.7 shows a 21%, 48% and 74% difference between R-ratios 0.3, 0.5 and 0.7 in relation to R=0.1, respectively. In comparison with Krieg's fibre-dominated specimens, that showed a difference of only 1.4%, this is

non-negligible, and challenges the assumption that the stiffness ratio can be omitted from Krieg's fatigue-life prediction equation (Equation 3.15).

5.1.4. Strain Progression

The strain progression is evaluated by reflecting on the shift of the cyclic stress-strain hysteresis loop, calculated using the following equation

$$\varepsilon_{\mathrm{m},i} = \frac{\varepsilon_{\max,i} + \varepsilon_{\min,i}}{2}. \tag{5.3}$$

Figure 5.8 shows the corresponding mean strain value throughout fatigue life for the different stress levels and R-ratios.

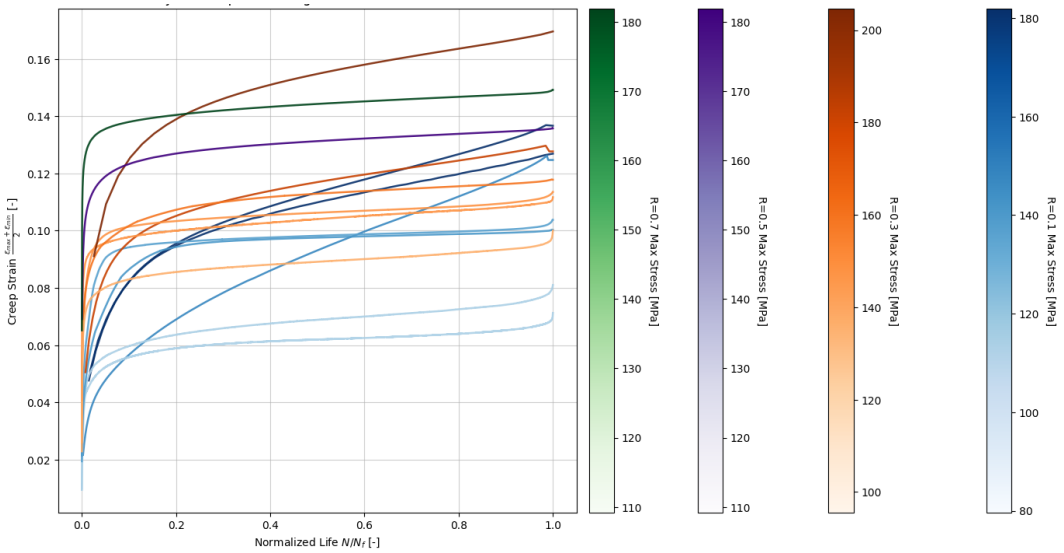


Figure 5.8: *Mean Strain Progression over the normalized fatigue lives. For the exact stress levels and corresponding test conditions, refer to the test matrix in Table 4.7.*

Similarly to the stiffness degradation, Figure 5.8 shows an initial rapid increase as a result of fibre reorientation. Following this stage, lower-stress tests approach a plateau, while higher-stress tests show a continuous increase in strain till failure. Figure 5.9 shows the fatigue failure strains plotted against the maximum stresses for the four R-ratios.

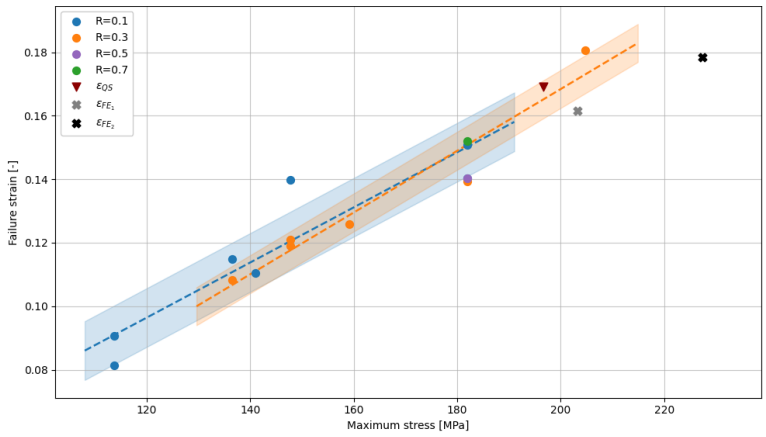


Figure 5.9: *Fatigue Failure Strain vs. Stress Level*

Figure 5.9 exhibits a largely linear relationship across the investigated R-ratios. Krieg's [0/90] results show that the $R = 0.1$ and $R = 0.3$ datasets do not initially collapse onto a single line, although they remain approximately parallel. He found that normalizing the results by a factor of $(1 - R^2)$, representing the ratio of the

work done on the material during a cycle to the maximum strain energy stored at peak loading, causes the two trends to collapse onto a common relationship [1].

In contrast, such a normalization appears unnecessary for the present ±45° results. This suggests that, for both R-ratios, the fatigue strain is governed primarily by the maximum stress rather than by the stress amplitude. This difference can be attributed to the distinct deformation mechanisms of the two laminate configurations. In the fibre-dominated [0/90] laminate, the 0° fibres are aligned with the loading direction, so the deformation and damage are strongly influenced by the cyclic elastic energy imposed on the fibres. For the ±45° laminate, however, deformation is dominated by matrix shear and fibre rotation. In this case, the cyclic stress amplitude influences the fatigue life by controlling how quickly the material ratchets toward its deformation limit, while the final strain capacity remains primarily governed by the maximum applied stress.

Regarding the relationship with the monotonic failure strains, the extrapolated fatigue-failure trends intersect closely with the quasi-static failure marker, as shown in Figure 5.9. During fast, dynamic monotonic loading, the matrix is forced to sustain load over a very short timescale, which limits viscous relaxation. As a result, the matrix exhibits a stiffer response and can sustain a higher stress before extensive in-plane shear deformation develops. In contrast, fatigue tests extend over many cycles and therefore subject the matrix to load over a much longer cumulative duration, making their deformation response more comparable to the quasi-static condition. Considering the two dynamic fatigue results, an increase in strain rate would generally be expected to increase both the ultimate strength and the corresponding failure strain. The comparatively low value of ϵ_{FE1} therefore suggests premature failure, likely caused by a local defect, fibre misalignment, or another specimen-specific imperfection, rather than representing the true ultimate strain capacity of the material.

5.1.5. Hysteresis Dissipated Energy

The dissipated energy is calculated by evaluating the area inside the hysteresis loop, using the following equation,

$$W_{\text{diss}} = \frac{1}{2}\sum_{i=1}^{n}(\epsilon_i\sigma_{i+1} - \sigma_i\epsilon_{i+1})\,. \tag{5.4}$$

The energy metric as a function of the normalized life across different stress levels and R-ratios is shown in Figure 5.10.

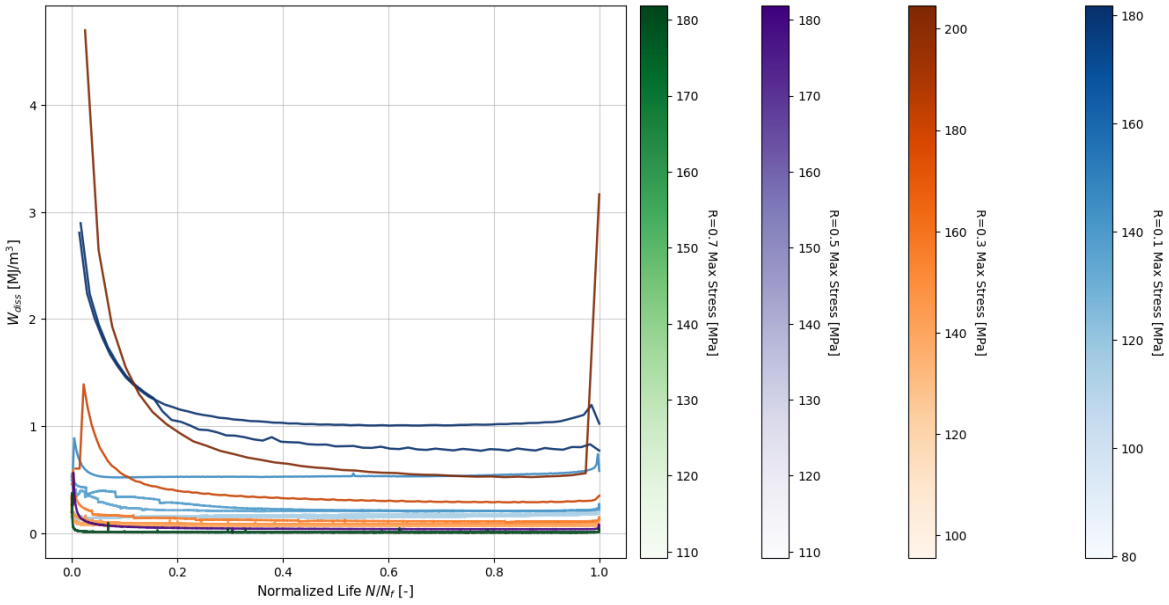


Figure 5.10: *Dissipated Energy over the normalized fatigue lives. For the exact stress levels and corresponding test conditions, refer to the test matrix in Table 4.7.*

Coinciding with the stiffness degradation and ratcheting strain, Figure 5.10 shows heavy dissipation at the start, especially for higher stresses. Following that, it approaches a plateau.

5.1.6. Applied Energy

The applied work is calculated as the area underneath the stress-strain hysteresis loop (Figure 2.1), following the following equation,

$$W_a = \frac{\sigma^2_{\max}}{2|E^*|} - \frac{\sigma^2_{\min}}{2|E^*|}. \tag{5.5}$$

Similar trends to the aforementioned metrics are depicted in Figure 5.11.

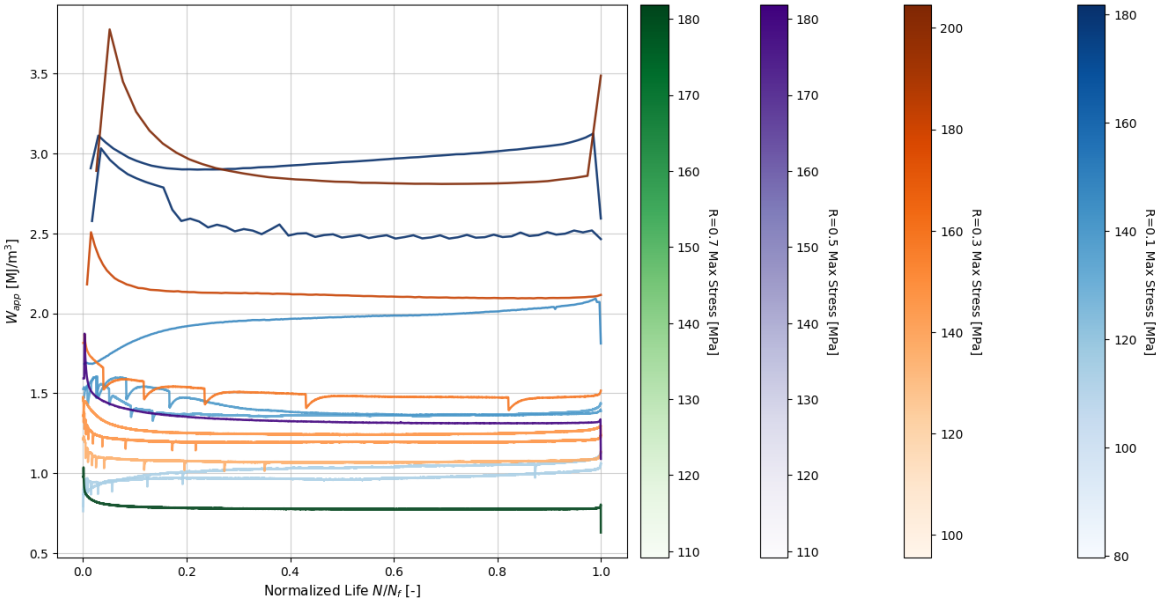


Figure 5.11: *Applied Energy over the normalized fatigue lives. For the exact stress levels and corresponding test conditions, refer to the test matrix in Table 4.7.*

Figure 5.11 shows a similar trend, with a relatively stable response at lower stress levels and subtle scattered behaviour as the stress level increases.

5.1.7. Loss Factor

The ratio between the dissipated energy and applied work is a critical parameter in the present study. Figure 5.12 and Figure 5.13 show the W_{diss}/W_a ratio and the viscoelastic loss factor against normalized life, respectively.

$$\text{Viscoelastic Loss Factor} \implies \sin(\phi) = \frac{1}{\pi}\frac{W_{diss}}{W_a}\left(\frac{1+R}{1-R}\right)^2, \qquad 0 \le R \le 1 \tag{5.6}$$

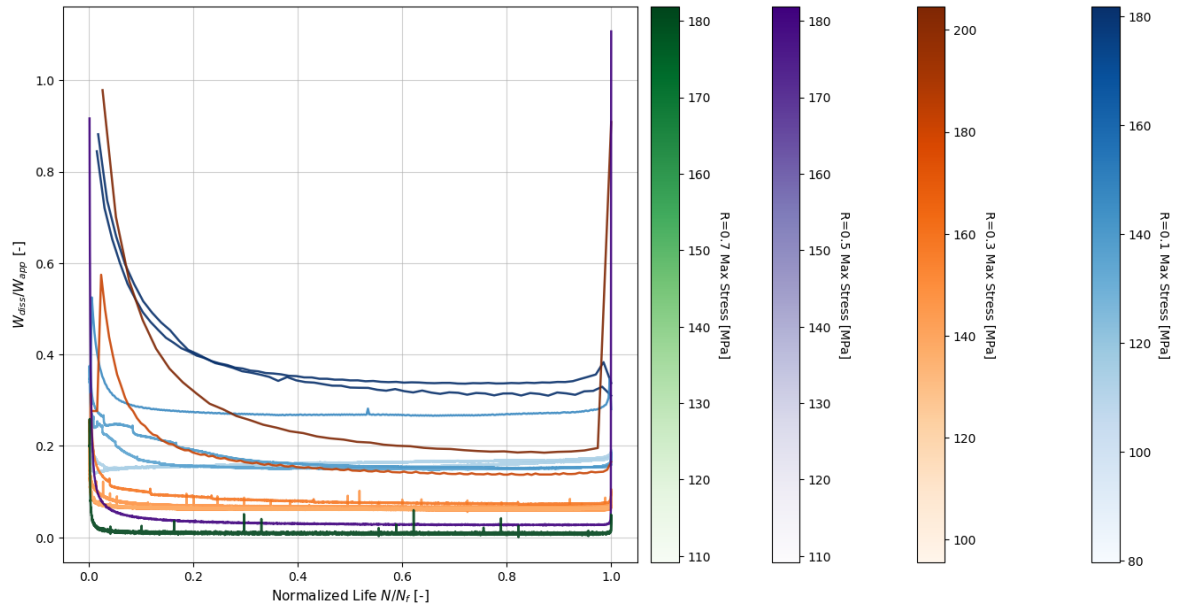


Figure 5.12: *Loss factor W_{diss}/W_a over the normalized fatigue lives. For the exact stress levels and corresponding test conditions, refer to the test matrix in Table 4.7.*

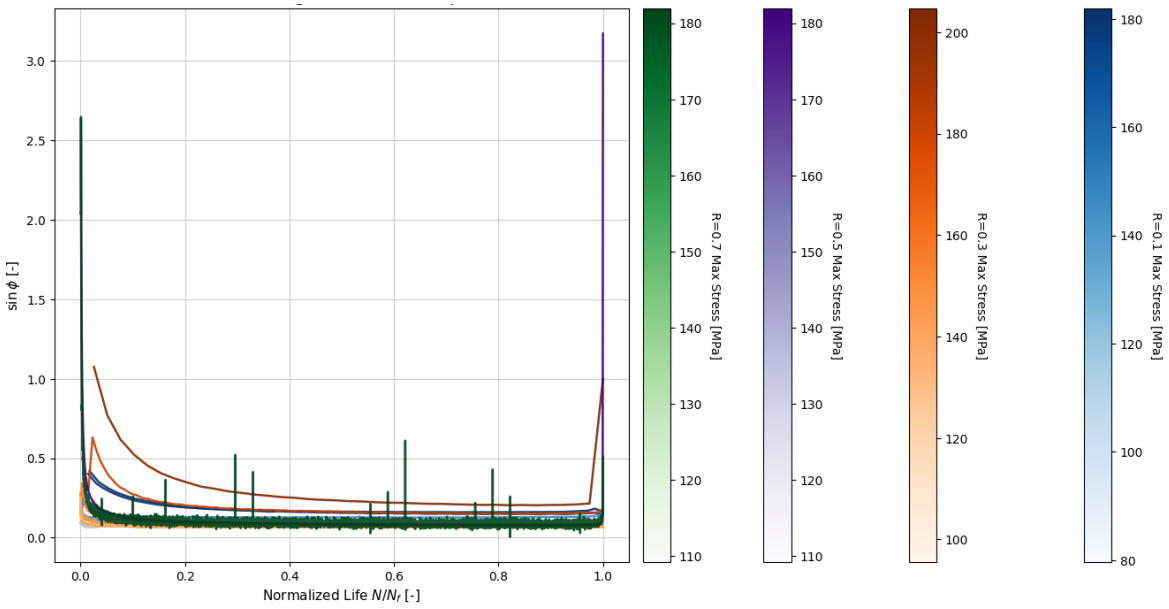


Figure 5.13: *Viscoelastic Loss factor* $\sin(\phi)$ *over the normalized fatigue lives. For the exact stress levels and corresponding test conditions, refer to the test matrix in Table 4.7.*

Both loss-factor metrics exhibit the same general evolution of a pronounced initial stage followed by a comparatively stable plateau over most of the fatigue life. The R-ratio terms in Equation 5.6 account for R-ratio-dependent differences in cyclic input energy, thereby enabling comparison of the derived loss factors across R-ratios. Referring back to Chapter 3, Krieg demonstrated that the stress-ratio dependent effective loss factor terms collapse such that,

$$\frac{\sin\left(\phi_{\text{eff}}\right)_{R_1}}{\sin\left(\phi_{\text{eff}}\right)_{R_2}} \approx 1. \tag{5.7}$$

The same can be said for the $\pm 45^\circ$ laminate as seen in Figure 5.13.

5.1.8. Answers to Research Question-01

This section concludes the above discussion on the exploratory observed behavior of the ±45° material, thereby answering the question,

> *To what extent do trends in stiffness degradation, cyclic ratcheting strain, loss factor and dissipated energy derived from cyclic stress–strain data exhibit consistent trends across stress levels and R-ratios, and to what extent can the loss factor therefore serve as a representative standalone damage metric for ±45° laminates?*

The trends in stiffness, cyclic strain progression and energy metrics were found to coincide in an overall consistent and physically meaningful manner. All showcased a pronounced initial transient that was caused by the fibre re-orientation during the early stages of loading, < 15% of fatigue life. This resulted in the stiffness increasing rapidly, while the mean strain and energy metrics changed drastically.

Following the initial stage, the responses exhibit a more stable trend approaching a plateau. At higher stresses, the strain continued to accumulate more strongly toward failure and for stiffness, responses showed a stiffness "enhancement" rather than degradation as it did not reach a distinct decay regime due to early failure. Therefore, the correspondence between the metrics is rather qualitative than strictly proportional. They exhibit similar stages of initial jump, followed by a stable plateau, although the degree of correspondence varies with the stress level and R-ratio.

The overall shapes of dissipated energy and applied work done are broadly similar, but the normalization removes much of the absolute energetic information. Two tests can therefore exhibit similar loss-factor trends while having very different absolute levels of dissipated energy, applied work, creep accumulation, or strain-rate evolution. The loss factor provides a useful normalized description of the dissipative behaviour, yet it does not uniquely capture irreversible strain accumulation, absolute energy dissipation, or changes in loading response. Consequently, for ±45° laminates, it is better interpreted alongside complementary metrics rather than as a standalone damage parameter.

5.2. Fatigue Life Prediction and Validation

In this section, the main slope constituent of the S-N curve is explored in relation to the creep-recovery test analysis (Subsection 5.2.1) and the stress-sweep test analysis (Subsection 5.2.3), with the aim of answering Research Questions-02 and -03 in Subsection 5.2.2 and Subsection 5.2.4, respectively.

5.2.1. Creep-Recovery Analysis, and the Augmentation Parameter Ψ

The creep-recovery test results are presented according to the sequence of analysis. Figure 5.14 shows the recovery strain ϵ_r as a function of reduced time λ before and after shifting to form the master curve. The 20% UTS curve is selected as the reference curve and is treated as representing the baseline linear response.

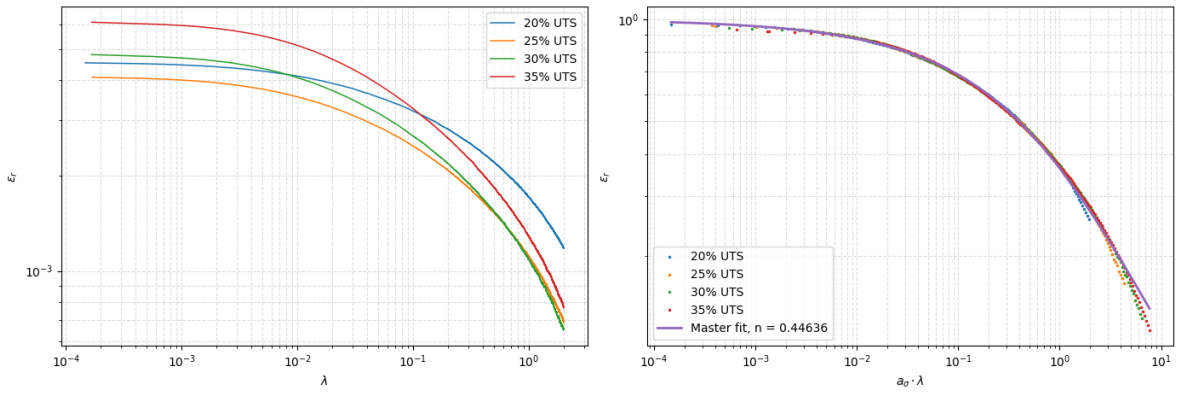


Figure 5.14: *Recovery Strain Curves against reduced time, before (left) and after (right) shifts*

Following Schapery's method of identifying model parameters, an n value of 0.446 is obtained. Schapery's paper [26] yields an n value of 0.27 which, in the context of the power law,

$$\Delta A(\psi) = C\psi^n \tag{5.8}$$

implies a higher time-dependence, meaning a more rapid creep accumulation. Using the n value of 0.446, the individual creep curves are fitted to obtain the remaining relevant stress-dependent parameters. The creep curve fits can be seen in Figure 5.15.

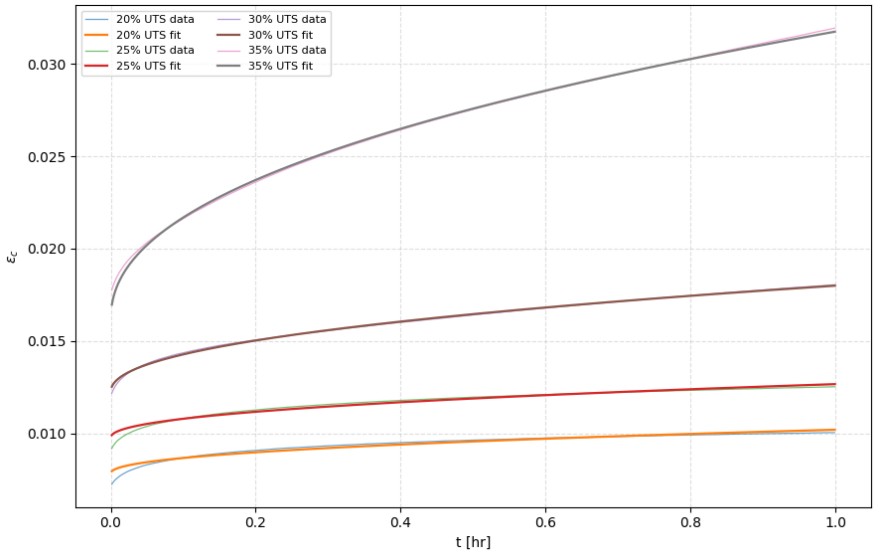


Figure 5.15: *Fitted creep strain vs. time curves for 20%, 25%, 30% and 35% UTS*

The final acquired stress-dependent parameters can be found in Table 5.2.

Table 5.2: *Identified Lou–Schapery model parameters at the investigated stress levels.*

UTS (%)	σ (MPa)	a_σ	g_0	g_1	g_2	Ψ	RMSE
20	45.48	1.000	1.000	0.507	1.973	1.000	0.000117
25	56.85	2.195	0.997	0.683	2.041	0.981	0.000113
30	68.22	3.286	1.039	1.136	2.431	1.623	0.000048
35	79.59	3.910	1.173	2.392	2.892	3.764	0.000111

Schapery's parameters were identified over stress levels ranging from 13.79 to 55.16 MPa (2000 to 8000 psi), with 2000 psi used as the baseline stress level. Similarly to Schapery's reported augmentation values, which ranged from approximately 1.0 to 3.3 - 4.0, the present analysis yielded values of Ψ ranging from 1.0 to 3.764. The only deviation is observed in the shift factor, a_σ which increases with stress in the present analysis, whereas Schapery reported a decreasing trend. This difference is associated with the direction of horizontal shifting required to construct the recovery master curve, with the present recovery curves shifted to the right rather than to the left.

5.2.2. Answers to Research Question-02

For ease of reference, the relevant research question is restated below.

How can a physics-based augmentation parameter, Ψ, be formulated to reformulate Lennart's fatigue-life prediction equation and compensate for deviations in stiffness degradation and effective loss factor across different stress ratios?

The augmentation parameters, Ψ, have now been obtained from Schapery's creep-recovery analysis. The next question is whether these parameters can be incorporated into Krieg's fatigue-life prediction model to account for the nonlinear viscoelastic behaviour observed in the $\pm 45°$laminates. A key limitation, however, concerns the mechanical conditioning procedure used prior to parameter identification. The maximum conditioning stress was limited to 100 MPa to ensure a repeatable strain response and to characterize the pristine nonlinear viscoelastic behaviour. This stress level is lower than the minimum stress level investigated

in the constant-amplitude fatigue campaign. Consequently, applying the identified augmentation parameters at the higher fatigue stress levels would require extrapolation beyond the experimentally characterized creep-recovery range. The question therefore becomes whether such an extrapolation is physically justified. Figure 5.16 shows the measured augmentation parameters in relation to the required values in order to accurately predict the fatigue lives.

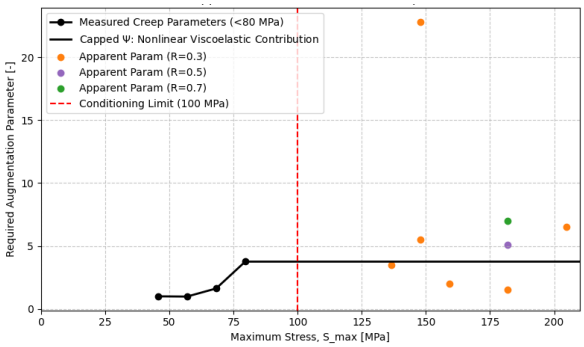
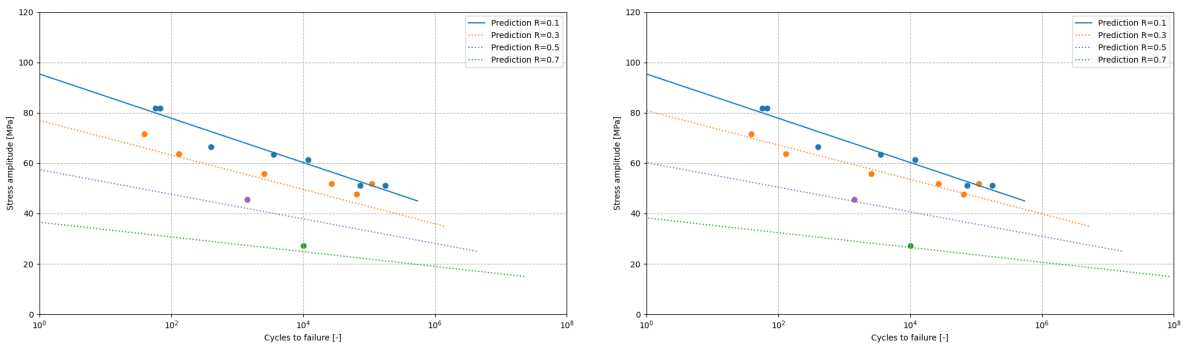


Figure 5.16: *Required Augmentation Parameters, in relation to yielded Parameters from Creep-Recovery tests.*

Figure 5.16 shows that blindly extrapolating would not be justifiable in this case. Schapery's nonlinear viscoelastic framework assumes that a material's non-linearity is strictly driven by stress-enhanced molecular mobility (such as an increase in free volume allowing polymer chains to slide easily) which is classified under a reversible thermodynamic process. Therefore, extrapolating would imply an "exaggerated" viscoelastic flow. In reality, this is not the case. At high stress levels, there are two competing mechanisms: viscoplasticity and continuum damage, that are unaccounted for in this case. Characterizing either or both would therefore provide a more physically accurate basis for defining this Ψ factor.

Therefore, as a first approximation, the following procedure is proposed. A threshold stress is first identified from the creep-recovery tests, defined by the stress level at which the creep-recovery test fails. For the identified parameters to remain representative primarily of nonlinear viscoelastic behaviour, this threshold should lie below the mechanical-conditioning limit, beyond which damage and viscoplastic effects may become significant. The augmentation parameter, Ψ, is then capped at the value corresponding to this threshold and treated as a saturated viscoelastic contribution at higher stress levels (see Figure 5.16). In this formulation, Ψ is intended to capture only the nonlinear viscoelastic contribution, while excluding additional effects associated with damage and viscoplastic deformation. So below this threshold stress, the measured augmentation parameters are used and above this threshold, the capped Ψ is applied. Figure 5.17 presents the resulting S–N curves, using the $R = 0.1$ dataset as the model input and predicting the response at $R = 0.3$, 0.5, and 0.7, with comparison against the corresponding validation fatigue data. Figure 5.17a shows the original Krieg framework excluding the new augmentation parameter, while Figure 5.17b shows the new augmented version.



(a) *Krieg-based fatigue-life prediction.*

(b) Ψ *Augmented fatigue-life prediction.*

Figure 5.17: *Comparison of the fatigue-life predictions obtained using the original Krieg formulation and the augmented model.*

Merely applying Krieg's life prediction equation gives a root-mean-square error (RMSE) of 0.656, 0.710 and

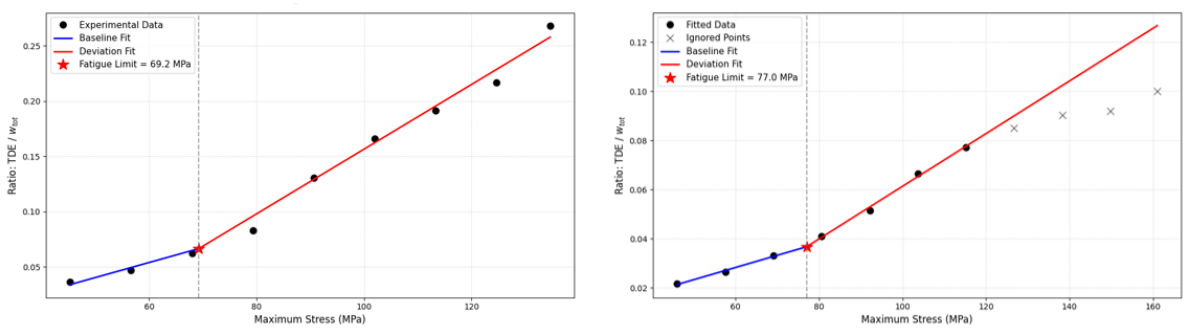
0.845 decades. With Schapery's contribution, the error reduces to 0.316, 0.134 and 0.269 decades. The substantial reduction in RMSE therefore supports the hypothesis that nonlinear viscoelasticity contributes meaningfully to fatigue-life behaviour, and that a saturated Ψ provides a reasonable first-order representation of this effect.

5.2.3. Stress-Sweep TDE-TW Ratio, and Implementation of Miner's Rule

The stress-sweep test results are used to plot the TDE/TW ratio as a function of stress level, before implementation of Miner's rule. The total dissipated energy TDE and TW are calculated as follows,

$$TDE = \sum_{i=1}^{1000} W_{diss_i} \quad \text{and} \quad TW = \sum_{i=1}^{1000} W_{a_i}. \tag{5.9}$$

This ratio plotted against the corresponding stress level is shown in Figure 5.18. Performing bilinear regression yields the damaged stress-levels, stress-levels greater than the transition point between the two linear regimes. These stress-levels are used along with Miner's rule as an alternative prediction method for the slope constituent. These graphs are further utilized in Subsection 5.3.2.



(a) $R = 0.1$ **(b)** $R = 0.3$

Figure 5.18: *Bilinear fits used to identify the fatigue-limit transition for stress ratios of* $R = 0.1$ *and* $R = 0.3$.

5.2.4. Answers to Research Question-03

For ease of reference, the relevant research question is restated below.

To what extent can stress-sweep testing, and the implementation of Miner's rule, be used to determine the S-N curve for $\pm 45^\circ$ *GFRP laminates, and thereby replace the reference* R_1 *fatigue dataset required by Krieg's fatigue-life prediction framework?*

Implementing the protocol described in Subsection 3.2.2, the prediction slopes for R-ratios 0.1 and 0.3, with comparison to the validation fatigue data, are presented in Figure 5.19. Note that the estimated fatigue limits obtained from Figure 5.18 are indicated on this graph for reference. A more detailed discussion of the bottom anchor will be provided in the subsequent sections.

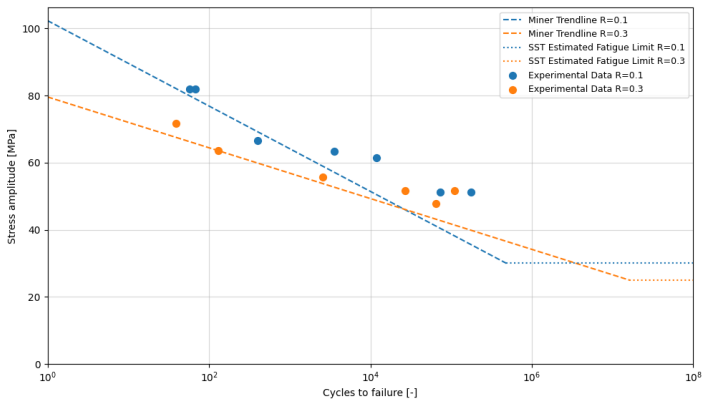


Figure 5.19: *Fatigue Life Predictions for R=0.1 and R=0.3 using Miner's rule on Stress-sweep tests.*

The root-mean-square errors for R-ratios 0.1 and 0.3 are 0.629 and 0.494 decades. Figure 5.19 shows a positive result for R=0.3, although R=0.1 seems less accurate especially for lower stress-levels. Sartorio [41] suggests a defective or damaged specimen may have been used in the stress-sweep test for R=0.1.

The question becomes, even with an error of 0.629 decades, can the Miner's rule applied at R=0.1 be the input data to predict the fatigue life of R-ratios 0.3, 0.5 and 0.7? Figure 5.20 shows this prediction on the S-N curve.

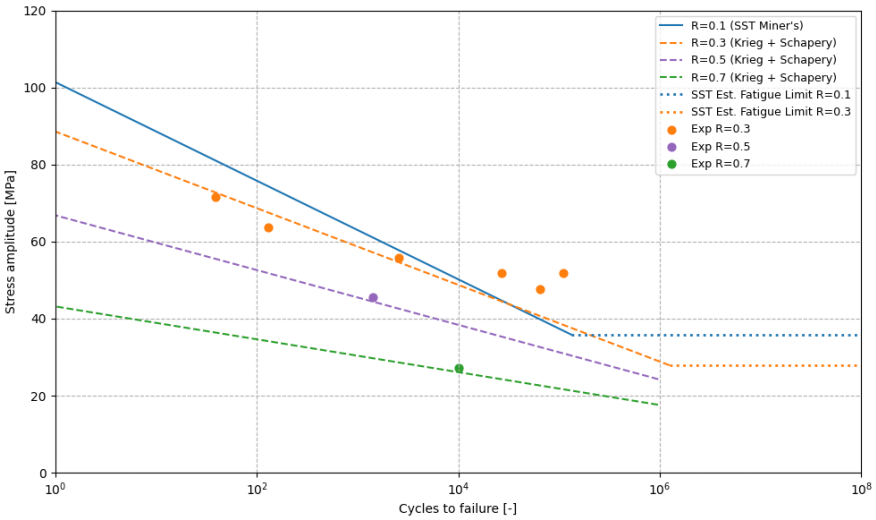


Figure 5.20: *Fatigue Life Predictions for R=0.3, 0.5 and 0.7 using input R=0.1 from SST Miner's rule.*

This give a root-mean-square error of 0.563, 0.148 and 0.284 for R-ratios 0.3, 0.5 and 0.7 respectively. Alternatively, given an input R=0.3 from Miner's rule, can slopes for R=0.1, 0.5 and 0.7 be predicted? Figure 5.21 shows this alternate S-N curve.

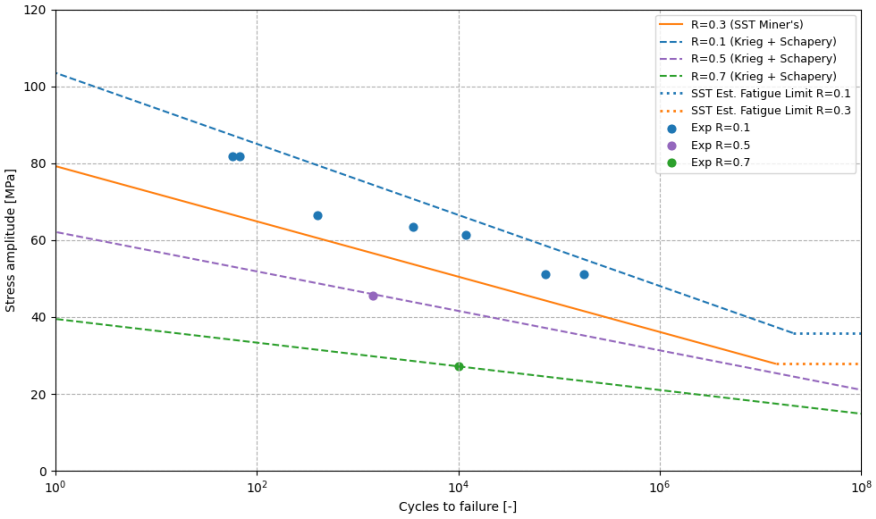


Figure 5.21: *Fatigue Life Predictions for R=0.1, 0.5 and 0.7 using input R=0.3 from SST Miner's Rule.*

This gives root-mean-square errors of 0.710, 0.093 and 0.043 decades for R-ratios 0.1, 0.5 and 0.7. Figure 5.21 shows that the prediction for R=0.1 seems non-conservative and may not be a feasible solution, even though the predictions for R-ratios 0.5 and 0.7 appear to be highly accurate. This, however, requires additional specimens to validate the curve further.

In conclusion, with the exception of the potentially defective R=0.1 SST specimen, the Miner's rule input for R=0.1 and Krieg-Schapery augmentation for higher stress-ratios appears to be a feasible start to a unified

physics-based fatigue life prediction, potentially eliminating the need for further constant amplitude fatigue testing.

5.3. Fatigue Limit Determination using DMA and SST

In this section, the bottom anchor constituent of the S-N curve is explored in relation to the DMA test analysis (Subsection 5.3.1) and stress-sweep testing (Subsection 5.3.2), with the aim of answering Research Questions -04 and -05, in Subsection 5.3.3.

5.3.1. DMA Test Results, and HCFS Determination

The storage modulus and the loss factors resulting from the temperature sweep are presented in Figure 5.22.

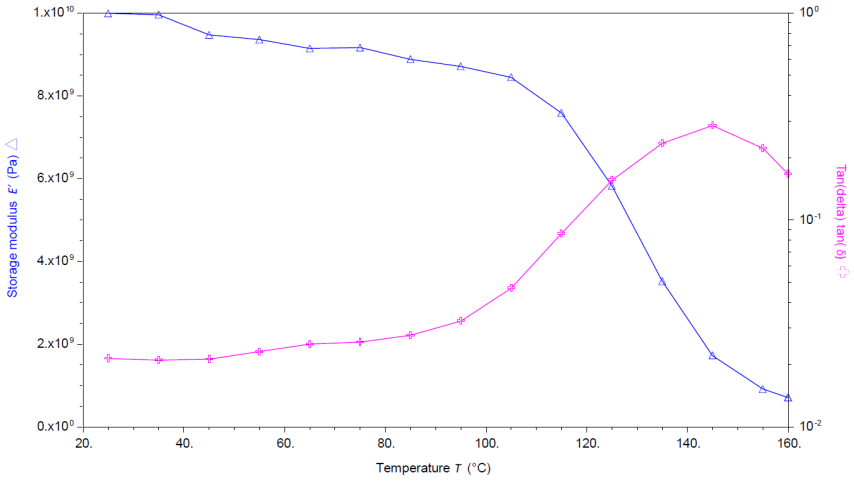


Figure 5.22: *Storage Modulus and Loss Factor vs. Temperature (DMA)*

Figure 5.22 can be used to determine the glass-transition temperature T_g. Following the ASTM E1640-23 and ASTM D7028-07 (2024), this metric is determined from the intersection of the glassy region ($65°C - 105°C$) and the steep gradient transition tangent ($\approx 115°C - 135°C$). This yields a T_g of $112°C$. With central attention on the temperatures below this limit, the loss factor ranges from 0.020 to 0.026 with only subtle temperature dependencies between $25°C - 80°C$. The mean value of 0.022 ± 0.002 was adopted as the pristine DMA loss factor.

In order to proceed with this pristine loss factor value for fatigue limit determination, the effective loss factor values from the fatigue data should be plotted against the corresponding stress levels. This is shown in Figure 5.23. Viscoelastic loss factor is the energy weighted average of the individual cycle loss factors over the fatigue life. The effective loss factor is calculated as follows,

$$\sin(\phi_{\text{eff}}) = \frac{1}{\pi} \frac{TDE}{TW} \left(\frac{1+R}{1-R} \right)^2 \tag{5.10}$$

where the TDE/TW ratio refers to the stable plateau seen in Figure 5.13.

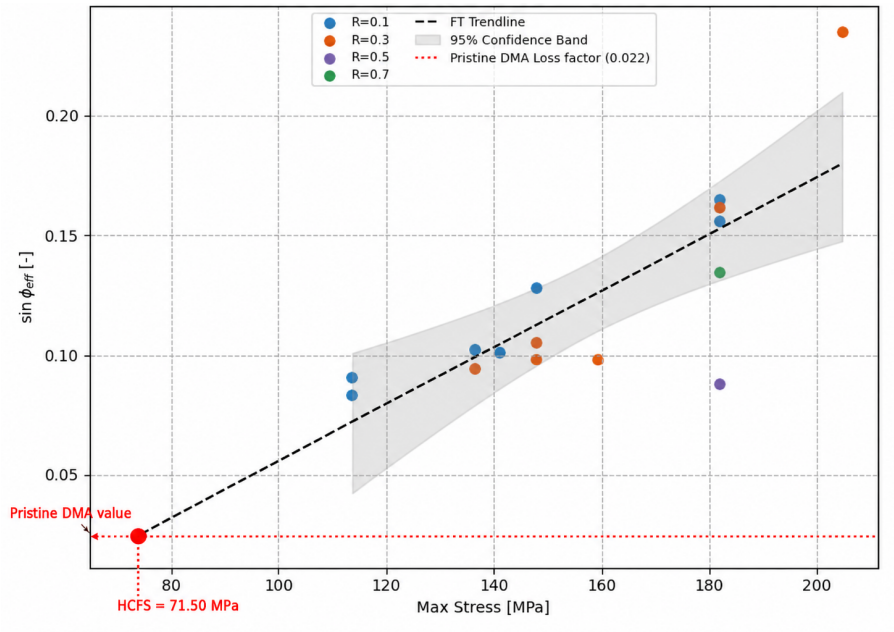


Figure 5.23: *Effective Loss Factors vs, Stress level for the different R-ratios, and HCFS determination using pristine DMA loss factor of 0.022.*

Figure 5.23 shows the best-fit line through the data points, together with its extrapolation. The intersection of this extrapolated line with the pristine DMA value of 0.022 yields an estimated HCFS value of 71.50 MPa.

5.3.2. Bilinear Regression on Stress-Sweep TDE-TW Ratio

The same stress-sweep test data can be used as an alternative method to evaluate the fatigue limit. This was done using bilinear regression on TDE/TW vs. stress level plot (Figure 5.19), where the transition between the two linear regimes yields the predicted fatigue limit. Fatigue limits of 69.2 MPa and 77.0 MPa for R-ratios 0.1 and 0.3 was obtained.

5.3.3. Answers to Research Question-04/05

For ease of reference, the relevant research questions are restated below.

How does the effective loss factor vary with stress level across different stress ratios, and how do its intersections with the pristine DMA loss factor correspond to stress-ratio-dependent HCFS values?

To what extent can the transition between two linear regimes in the TDE-to-total-work ratio during stress-sweep testing be used to identify a reliable lower fatigue-limit estimate for $\pm 45^\circ$ *laminates?*

Figure 5.23 shows that the effective loss factors collapse onto a single line, allowing a single intersection with the pristine DMA loss factor. The pristine DMA loss factor gives an estimated fatigue limit of 71.5 MPa. This is in good agreement with the stress-sweep fatigue limit of 69.2 MPa obtained at $R = 0.1$, particularly considering that the DMA test was not performed at an exact stress ratio of $R = 0.1$. In the DMA test, the axial force was maintained at 10% greater than the oscillatory force amplitude. For a sinusoidal load, the equivalent stress ratio can be expressed as

$$R = \frac{F_{\text{mean}} - F_{\text{amp}}}{F_{\text{mean}} + F_{\text{amp}}}.$$

Therefore, with $F_{\text{mean}} = 1.1F_{\text{amp}}$, the DMA loading condition corresponds to an equivalent sinusoidal force ratio of approximately $R = 0.048$, rather than $R = 0.1$. Although a lower stress ratio would generally be expected to result in a lower fatigue limit, the DMA-based estimate of 71.5 MPa is slightly higher than the 69.2 MPa obtained from the $R = 0.1$ stress-sweep test. This small difference should therefore not be interpreted as a direct stress-ratio effect, particularly since the two values were obtained using different estimation methods and the DMA loading ratio does not correspond directly to a fatigue-test stress ratio. Nevertheless, both

estimates are of comparable magnitude, while the higher fatigue limit of approximately 77 MPa obtained at $R = 0.3$ is consistent with the expected overall increase in fatigue limit with increasing stress ratio. The close agreement between the DMA- and SST-based estimates therefore supports the use of the pristine DMA loss factor as an approximate fatigue-limit criterion.

With regard to literature values, Movahedi-Rad et al. [34], Liang et al. [22] and Colombo et al. [20] present fatigue limits of 43-45 MPa, 45-50 MPa and 30-36 MPa, respectively. These seem relatively low in comparison to the limits yielded from the current DMA and SST tests. However, normalizing by UTS provides a first-order comparison. Their fatigue/UTS ratios appear to be 44%-47%, 44%-49% and 21%-26% UTS. In this case, the results yield a ratio of 34% UTS so it is a more reasonable result. In conclusion, a fatigue-limit determination through both DMA and SST seem feasible, yielding a value in between 69 - 77 MPa for this ±45° prepreg material.

5.4. Rate-Dependent UTS and S-N curve Applicability

In this section, the upper anchor constituent of the S-N curve is explored in relation to the rate-dependent monotonic tensile tests performed in Subsection 4.3.1, addressing Research Question-06 in Subsection 5.4.1.

5.4.1. Answers to Research Question-06

For ease of reference, the relevant research question is restated below.

To what extent can dynamic tests performed at fatigue-equivalent loading rates provide a suitable basis for defining the upper anchor of the S–N curve?

The monotonic tensile test results confirmed the strain-rate sensitivity of the ultimate tensile strength values, with an increase of 4.4% to 18.8% from quasi-static to fatigue-equivalent dynamic rate. The question becomes which of these values is responsible for the upper anchor constituent of the S-N curve at $N_f = 1$. A monotonic tensile test corresponds approximately to an R=0 loading condition, since the stress increases from $\sigma_{min} = 0$ to $\sigma_{max} = UTS$. Figure 5.24 plots the equivalent UTS/2 data-points alongside the fatigue life predictions using Krieg-Schapery augmentation for R=0, 0.3, 0.5 and 0.7 with R=0.1 input data.

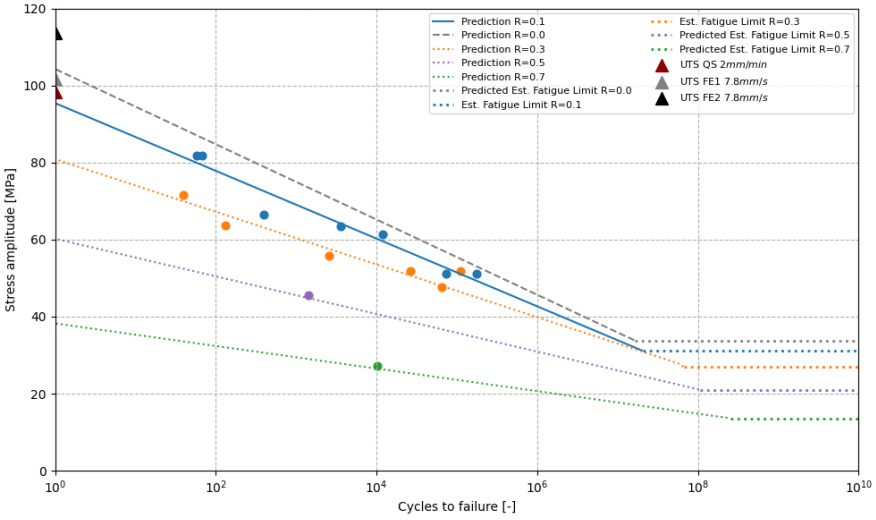


Figure 5.24: *Fatigue Life Predictions for R=0, 0.3, 0.5 and 0.7 using input R=0.1 with Krieg-Schapery augmentation, incorporating UTS values obtained from the monotonic tensile (MT) results*

The results therefore support the use of fatigue-equivalent-rate monotonic tensile strength as the $N_f = 1, R = 0$ upper anchor, although the limited number and scatter of dynamic tensile specimens prevent this conclusion from being considered fully validated. Figure 5.24 also presents predicted fatigue limits for R-ratios of 0, 0.5, and 0.7, obtained by linear extrapolation from the estimated fatigue limits at $R = 0.1$ and $R = 0.3$. Whether this linear relationship can reliably predict the fatigue limit across a wider range of stress ratios remains uncertain. Additional DMA tests conducted at equivalent stress ratios, or further stress-sweep testing,

are therefore required to validate this assumption experimentally. Nevertheless, the current results indicate the extrapolated fatigue limits for different stress ratios, although direct experimental validation of the values is still lacking.

5.5. Towards a Unified Fatigue-Life Prediction Approach

The preceding sections investigated the observed behavior of this ±45° laminate and how it comes together to the three principal constituents of the S-N curve independently; the slope, the bottom anchor and the upper anchor. The present study used the R=0.1 constant-amplitude fatigue dataset as the reference condition R_1 for predictions towards R=0.3, 0.5 and 0.7, consistent with Krieg's selection of $R = 0.1$ as the reference condition [1], which was adopted to maintain comparability with the original framework.

Ideally, the reference S-N curve would be established at R=0. This provides a physically convenient starting condition given that the upper anchor of R=0 is directly associated with the fatigue-equivalent monotonic tensile strength. The remaining constituents of the reference R=0 S-N curve could then, in principle, be obtained without a conventional constant-amplitude fatigue campaign. An R=0 stress-sweep test could be used to estimate the S-N slope through the Miner's rule procedure, while the transition in the stress-sweep TDE/TW response could provide an estimate of the corresponding fatigue limit. The latter could additionally be compared with a pristine DMA loss-factor measurement obtained with the mean axial force equal to the oscillatory force amplitude, corresponding to an equivalent sinusoidal force ratio of $R = 0$. Alternatively, if stress-sweep testing is excluded from the framework, a simpler first-order approach could be to define the S–N curve by interpolating between the fatigue-equivalent UTS as the upper anchor and the DMA-derived fatigue limit as the bottom anchor. In this manner, the upper anchor, slope and bottom anchor of the R=0 reference curve could each be obtained predominantly from shorter-duration material characterisation tests rather than from a complete fatigue dataset.

Once the R=0 reference curve is established, the extended Krieg & Schapery formulation could subsequently be used to transform this reference response to higher stress-ratios R>0. For matrix-dominated laminates, the nonlinear viscoelastic augmentation introduced in this thesis would then account for the additional stress-dependent dissipation when transferring the reference response toward higher R-ratios.

Such an approach should presently be regarded as a proposed pathway rather than a validated predictive framework. In particular, the $R = 0$ stress-sweep slope and fatigue limit have not been experimentally established in the present study, the extrapolation of fatigue-limit behaviour across stress ratios remains unvalidated, and the use of Miner's rule provides an empirical rather than uniquely physical representation of cumulative fatigue damage. Nevertheless, the present results demonstrate that each constituent required to construct such a framework can, to varying degrees, be related to independently measurable material responses. This provides a basis for future work in which a single $R = 0$ reference condition could be characterized using relatively short-duration tests and subsequently transformed to predict fatigue behaviour at higher stress ratios.

5.6. Limitations

The results of this study demonstrate the potential of combining nonlinear viscoelastic characterization, energy-based fatigue metrics, dynamic mechanical analysis, and stress-sweep testing to construct the three principal constituents of the S-N curv. However, the results should be interpreted within the boundaries of the present experimental campaign and practical time constraints. This section summarizes the limitations that restrict the extent to which the proposed methods can currently be generalized, and highlights the areas in which further characterization is required for advancement of the model.

1. **Limited sample size and experimental scatter.**

   Although a variety of experiments were conducted: fatigue tests at multiple stress-ratios, creep tests, stress-sweep tests, etc., some conclusions are based on very few specimens. For example, the fatigue-equivalent UTS values and their applicability as the upper anchor are supported by two specimens which show a relatively large range. In addition, for stress-ratios R=0.5 and R=0.7, the prediction accurate is high yet they are validated by one specimen per stress-ratio.

2. **The Schapery Augmentation Parameter Ψ is identified at stress-levels below the main fatigue stress range.**

This is one of the main critical limitations of the aforementioned conclusions.The creep-recovery tests were conducted at a conservative stress level of 100 MPa to avoid failure, again to preserve the limited specimens. The improved fatigue life predictions, however, appear promising, but the physical validity of a capped Ψ still requires direct experimental confirmation.

3. **The augmentation parameter Ψ does not include viscoplasticity and damage characterization, pertinent to higher stress levels.**

   Building on the previous limitation, the augmentation parameter Ψ should account for viscoplastic and damage effects in order to have a more physically accurate model. Further recommendations to account for this limitation are discussed further in Section 6.3.

4. **Miner's Rule assumes linear-damage phenomena.**

   Miner's rule is more commonly applied to variable amplitude loading fatigue life predictions. Mathematically, it expresses linear cumulative damage accumulation, see item 3.31. This means that load-sequence effects or interaction between damage types at successive stress levels is not addressed. This is especially relevant for the case of matrix-dominated $\pm 45^\circ$ laminate, where fibre rotation, ratcheting and nonlinear viscoelastic effects evolve synergistically during loading.

5. **The R=0.1 stress-sweep result may be affected by specimen-related imperfections.**

   Sartorio [41] speculates that the stress-sweep miner's prediction for R=0.1 may be substantially poorer than the R=0.3 case, seen in Figure 5.19, suggesting the defective specimen supposition. However, again referring to the limited sample size and validation data, with only one test it is inaccurate to conclude with confidence whether the Miner's rule prediction holds for all stress-ratios.

6. **The fatigue limit predictions are accurate estimations at this stage, not directly validated.**

   The bottom anchor fatigue limit estimations from both DMA and stress-sweep responses yield a value of around 69 - 77 MPa which seem reassuring, but they have not been validated with long-duration constant-amplitude tests, especially when the capped maximum total number of cycles was restricted at 10^6 cycles accounting for time constraints. Therefore, the bottom anchor predictions should be currently denoted as estimated fatigue limits, rather than validated endurance values for this $\pm 45^\circ$ prepreg laminate.

7. **Limited DMA tests at different frequencies and load set-ups.**

   Initially, the plan was to conduct multiple DMA tests using both 3-point-bending and double-cantilever-beam loading configurations at several frequencies, in order to maintain consistency with Krieg's methodology and to investigate the sensitivity of the results to temperature and frequency. However, due to machine inoperability, only one set of DMA results was obtained. In hindsight, additional DMA tests using alternative loading conditions could have provided further insight into the influence of stress ratio. For example, increasing the axial force from 10% to approximately 22% above the oscillatory force amplitude would have produced a loading condition close to $R = 0.1$, while larger axial-force offsets could have been used to investigate higher stress ratios. Such tests would have enabled a more direct comparison with the fatigue stress-sweep results and provided a more robust assessment of the DMA-based fatigue-limit estimation method.

8. **Maintaining equivalent strain-rate conditions across stress levels is difficult for $\pm 45^\circ$ laminate.**

   Figure 5.4 shows pronounced early fibre re-orientation and therefore associated stiffness enhancement, meaning that the prescribed strain rate changes almost immediately after loading is imposed. Following the initial re-orientation stage, stiffness evolution trends approach a stable plateau. This indicates that establishing an initial strain rate may be more challenging than controlling its evolution. A physically-supported prediction method should be looked into to characterize the initial re-orientation induced by loading such that its proportionality to the initial stiffness could be used to program the frequency needed to maintain the same target strain rate.

9. **Lack of material defect characterisation through C-scan inspection.**

   No C-scan inspection was performed on the manufactured laminate prior to specimen testing, limiting the ability to relate the observed mechanical response to possible internal manufacturing defects.

This represents a particular limitation given the considerable scatter observed in the fatigue-equivalent UTS measurements, since it cannot be determined whether this variability originated primarily from the loading procedure, specimen-to-specimen material variability, or pre-existing defects within the laminate. More broadly, the absence of defect characterisation also introduces uncertainty when interpreting the remaining experimental results, as undetected imperfections may have influenced local stress concentrations, damage initiation and fatigue life. Future studies should therefore incorporate C-scan inspection and retain the positional traceability of each specimen within the original laminate so that measured defects can be compared directly with the subsequent mechanical response.

10. **The results are specific to $\pm 45^\circ$ E-Glass/Epoxy Prepreg laminates.**

    The current study concerns one $\pm 45^\circ$ prepreg system using a specific Double Euler geometry and testing only at positive R-ratios. The validity of the proposed methods to identify the constituents of the S-N curve requires further attention. Validation would be needed for other lay-ups, resin systems, fibre systems, geometries, strain-rates, temperatures and negative R-ratios.

    Referring back to the manufacturing limitations discussed in the methodology, the restricted number of specimens due to the distinctive surface texture of the laminate should also be considered when interpreting the generalisability of the results. However, the textured surface did not appear to introduce fibre-related defects severe enough to invalidate the observed fatigue trends. The results can therefore still be regarded as a useful proof of concept for the specific material system investigated, provided that the underlying physical interpretation is valid. Nevertheless, broader validation across additional material systems and laminate configurations is beneficial before the proposed approach can be considered generally applicable.

6 Conclusion

This chapter concludes the present study by summarising the main findings in Section 6.1 and evaluating their significance within the broader objective in Section 6.2. Finally, recommendations for future advancements are discussed in Section 6.3.

6.1. Summary

This thesis investigated approaches to expand on Krieg's modified linear viscoelastic framework for fatigue life prediction. The study was structured around the three principal constituents of the S-N curve : the slope, the bottom anchor (fatigue limit) and upper anchor (representative UTS value). The objective was to investigate whether these three constituents could be characterized through nonlinear viscoelastic characterization, stress-sweep testing, dynamic mechanical analysis and fatigue-equivalent monotonic tensile testing.

An experimental campaign was performed on $\pm 45^\circ$ specimens with a Double-Euler geometry. The constant amplitude fatigue tests covered R-ratios 0.1, 0.3, 0.5 and 0.7, and provided the input and validation datasets required to assess the proposed prediction approaches. Analysis of cyclic stress-strain hysteresis loops yielded trends in stiffness evolution, mean-strain progression and energy-dissipation metrics that collectively show a consistent trend through the fatigue life; a pronounced initial transient as a result of fibre re-orientation followed by a more stabilized plateau.

Krieg's fatigue-life prediction equation was tested to see whether the augmentation parameter $\Psi = \frac{g_1 g_2}{a_\sigma}$ could be used to extend his equation to be suitable for matrix-dominated composites. Creep-recovery testing yielded augmentation parameter values from 1.0 to 3.7. Since the experimentally characterized stress range remained below that of the constant-amplitude fatigue tests, direct extrapolation was considered unjustified. Instead, the cut-off point identified from the creep-recovery tests was used as a first-order approximation of the nonlinear viscoelastic contribution. The corresponding maximum augmentation parameter was therefore applied at the higher stress levels. This reduces the RMSE values from 0.656, 0.710, and 0.845 decades to 0.316, 0.134, and 0.269 for predictions at R=0.3, 0.5, and 0.7, respectively. It is beneficial to see a reduction in the RMSE value as a result of incorporating the nonlinear viscoelastic effects but it does not establish that it uniquely represents the exact nonlinear viscoelastic contribution. Rather, it indicates that accounting for nonlinear viscoelastic effects improves the predictive capability of the model for matrix-dominated composites.

A second approach investigated whether stress-sweep testing could be used to implement Miner's rule and predict the slope of the S-N curve. This method showed encouraging predictive capability, obtaining an error of 0.629 and 0.494 decades for R = 0.1 and R =0 .3. This shows that it could act as a surrogate for S-N slope estimations for the input fatigue data R_1.

The bottom anchor was investigated independently using two methods: DMA and stress-sweep testing. The DMA analysis yielded a fatigue limit of 71.5 MPa through the intersection of the effective loss factor trend and the pristine loss factor of 0.022 ± 0.002. The DMA loading condition itself corresponded to an equivalent sinusoidal force ratio of approximately $R = 0.048$. Alternately, bilinear regression on the TDE/TW ratio vs. stress level plot yielded two fatigue limits of 69.2 MPa and 77.0 MPa for R-ratios 0.1 and 0.3, respectively. The agreement between these independent methods supports the possibility of characterising the bottom anchor constituent of the S-N curve . However, experimental data were not obtained to directly validate this fatigue limits so they remain estimates.

Finally, fatigue-equivalent monotonic tensile testing exhibited clear strain-rate sensitivities yielding UTS values that increase 4.4-18.8% from quasi-static to fatigue-equivalent rates. In the context of defining the upper anchor of the $R = 0$ S–N curve, the fatigue-equivalent UTS values may provide a more representative estimate than the quasi-static UTS values, as they are obtained at strain rates closer to those experienced during fatigue loading. However, considerable variability remains among the measured UTS values.

6.2. Concluding Remarks

The overarching main research question that guided the trajectory of the thesis is re-stated as follows:

To what extent do $\pm 45^\circ$ composite laminates conform to Krieg's modified linear viscoelastic fatigue prediction framework, and how can previously overlooked matrix-dominated behaviors be used to justify the framework's deviation, and be leveraged to extend it?

The findings of the present study show that ±45° laminates do conform to the fundamental energy-based principles of Krieg's framework, allowing a reasonable fatigue life prediction with a root-mean-square error of 0.656 decades (for R = 0.3). Nonetheless, characterizing the stress-dependent terms associated with Schapery's nonlinear viscoelastic theory could be used to augment Krieg's framework to account for nonlinear viscoelastic effects, reducing the error to 0.316 decades. It is believed that future research on characterizing the viscoplastic and damage effects would result in a more accurate framework. In addition, stress-sweep testing and using Miner's rule proved to be a plausible starting approach to replace the input fatigue data that is required for Krieg's framework. Further work is required to assess the applicability of Miner's rule in this context. This should include additional validation points and a more rigorous investigation of the physical basis of the approach, particularly given the largely empirical nature of Miner's rule and its limited ability to capture the underlying fatigue-damage mechanisms, especially given the time- and load-sequence-dependent behaviour associated with stress-sweep testing of matrix-dominated composites.

Furthermore, DMA and stress-sweep testing independently produced comparable estimates of the fatigue-limit, while fatigue-equivalent monotonic tensile strength showed potential for defining the upper anchor ($N_f = 1$). The results therefore supports a transition from a purely modified linear viscoelastic framework toward a broader formulation in which the upper anchor, S-N slope and bottom anchor are linked to independently measurable material properties.

All in all, the findings provide a proof-of-concept of extending Krieg's modified linear viscoelastic framework to matrix-dominated ±45° laminates.

6.3. Recommendations

The thesis has shown the possibility of a unified physics-based framework, demonstrating that Krieg's framework can be extended to matrix-dominated composites, such as ±45°, with proposed augmentation methods. However, there is a wide range of opportunities to continue expanding this framework and this field of work, with the aim of making all fatigue testing obsolete. This section presents several fundamental recommendations that may be valuable for future research. A more elaborate procedure for applying and extending the framework in future research is presented in Appendix B.

1. **Coupled Viscoelastic-Viscoplastic and Damage Characterization Models for the Augmentation Parameter Ψ.**

   Future studies can investigate methods to characterize the viscoplastic and damage effects that contribute to predicting fatigue life, outside of the pristine nonlinear response using Schapery. In literature, researchers have already started to identify Schapery's nonlinear viscoelastic theory as insufficient for higher stress levels. Thereafter, several coupled models exist such as Schapery's Work Potential Theory [55] which presents a constitutive equation that describes viscoplastic and damage characteristics. Future research should explore this constitutive equation and corresponding characterization protocols for the relevant model parameters.

   Zhang et al. [56] researches a modified protocol, directly addressing Schapery's missing components, such as permanent creep/damage. They add a viscoplastic strain term, $B\sigma^s t^m$ which represents permanent, irreversible creep deformation. They also characterize the damage, by introducing an effective stress that represents the damaged state, $\bar{\sigma} = \frac{\sigma}{1-D}$.

   In addition, Zhang et al. [56] excludes the g_1 stress-dependent term as they argue it creates unrealistic instantaneous jumps in the viscoelastic strains when the applied stresses change. For sufficient damage characterization, the specimens were tested in their "fresh" state without mechanically conditioning. This requires at least one specimen per stress-level, which was beyond the practical limits imposed by the specimen size used in the current study. An important remark is that the Zhang et al. tested at a maximum stress level of approximately 90 MPa. Therefore, further research should investigate the use of Zhang's protocol, and see whether augmentation parameters can be characterized for higher stress-levels. If not, investigate whether it is physically-accurate to extrapolate to those higher stress levels.

2. **Modeling of Early-Stage Fibre Re-orientation, and therefore strain-rate control.**

   The thesis revealed that there is a non-negligible contribution from fibre re-orientation that shapes the early stages of fatigue life. This causes a sharp transient shift in the effective stiffness which renders the conventional strain-rate controls ineffective. Further research should explore the relationship between

pristine stiffness moduli from monotonic tensile tests, initial fibre angles, and rotation angle models that enable predictions of the stiffness trends, and therefore the strain-rate control as well.

Moreno et al. [54] explored fibre re-orientation of ±45° laminates and monitored their change in angle. This updated fibre angle was fed into Classical Laminate Plate Theory (CLPT) to investigate the resulting stiffness. Subsequently, they investigated how this fibre re-orientation contributes to the pseudiductile nonlinear response. This may not substitute as a basis for a kinematic re-orientation model, but could be a promising starting point for further research.

3. **Strain-Sweep Tests and Continuum Damage Models as alternative Fatigue Prediction Model.**

   The current thesis focused on building on Lennart Krieg's framework on fibre-dominated composite domain requiring adaptation to account for the matrix complexities inherent to ±45° laminates. An alternative perspective is to approach the problem from the opposite direction: taking a pure-matrix damage model for fatigue life prediction and subjecting it to the structural complexities introduced by a fibrous architecture.

   In the asphalt binder and neat polymer industries [57], multiple amplitude tests (MAT), simply strain-sweep tests, are used as a surrogate for fatigue life prediction utilising a Simplified Viscoelastic Continuum Damage (S-VECD) model. Future research could investigate the use of strain-sweep tests for fatigue life prediction, while addressing the complexities that come with the presence of fibres. Strain-sweep tests seem promising for the use of the bottom anchor constituent as well. Low-amplitude blocks of the strain-sweep tests could act as an in-situ tensile DMA, extracting the pristine effective loss factors.

4. **Broadening Frequency and Temperature Spectra in Dynamic Mechanical Analysis (DMA).**

   The thesis demonstrated a promising baseline for the fatigue limit predictions with a single DMA dataset. However, further tests should be conducted to measure temperature and frequency sensitivities, and evaluate whether the predictions remain promising. A greater research direction is utilizing these dynamic mechanical analysis tests to map out comprehensive master curves using Time-Temperature Superposition (TTS) principles across varied loading configurations. In addition, a tensile configuration on the DMA could yield a more accurate representation. A tensile-tensile configuration is intended for thin films, strips and individual fibers and fiber bundles so if the specimen is manufactured sufficiently thin, the tensile DMA response could be analyzed.

5. **Extension to other Laminate Configurations, Thermoplastic Matrix and negative R-ratios.**

   The methodologies adopted in this thesis were limited to tension-tension fatigue (R>0) on a specific ±45° E-glass/epoxy prepreg layup using a Double-Euler geometry. The applicability of this model for other matrix-dominated composites of different angles can be investigated.

   Schapery et al. [26] investigate multiple off-axis fibre re-orientations, $0°, 30°, 45°, 60°$ and 90° where he argues that if the polymer matrix properties remain the same between the different fibre orientations, then it should not matter at what angle the fibres are positioned at. Under the same load, the different orientations experience different responses which Schapery wanted to normalize the angle-dependent information with an effective parameter τ_σ, which he coins as the "normalized octahedral shear stress". Under his assumption that two fibre angles with the same octahedral shear stress τ_σ should have similar nonlinear behaviours. Future research could investigate the applicability of this octahedral shear stress quantity to characterize and normalize angle-ply laminate configurations.

   The applicability of this model to thermoplastic matrix should also be investigated where it showed even greater time-, temperature- and strain-rate dependencies. In addition, the whole damage mechanisms alter as the focus drifts to compression-compression fatigue so future research could explore whether viscoelastic theories can be applied in the context of compression.

Overall, these research directions are recommended to further expand this field of fatigue life prediction and hopefully make all fatigue testing obsolete.

References

[1] Krieg, L. L., "A Viscoelastic Analysis Approach to the Energy Dissipation in Fatigue of Fibre Reinforced Polymer Composites," Master's thesis, Delft University of Technology, Delft, The Netherlands, 2025.

[2] Vassilopoulos, A. P., "The History of Fiber-Reinforced Polymer Composite Laminate Fatigue Research and Current State of the Art," *Composites Part A: Applied Science and Manufacturing*, vol. 139, p. 106 101, 2020. DOI: 10.1016/j.compositesa.2020.106101.

[3] CAE Assistant (MyPhysicsCafe). "Composite fatigue: Analysis and importance in material engineering," Accessed: Jan. 11, 2026. [Online]. Available: https://www.myphysicscafe.com/post/composite-fatigue-analysis-and-importance-in-material-engineering.

[4] Schijve, J., "Fatigue of Structures and Materials in the 20th Century and Beyond," *International Journal of Fatigue*, vol. 25, pp. 679–702, 2003. DOI: 10.1016/S0142-1123(03)00051-3.

[5] Kaminski, M., Laurin, F., Maire, J.-F., Rakotoarisoa, C., and Hémon, E., "Fatigue Damage Modeling of Composite Structures: The ONERA Viewpoint," *AerospaceLab*, pp. 1–12, Issue 9 2015. DOI: 10.12762/2015.AL09-06.

[6] Bogdanov, A. A., Panin, S. V., and Kosmachew, P. V., "Fatigue Damage Assessment and Lifetime Prediction of Short Fiber Reinforced Polymer Composites—A Review," *Journal of Composite Science*, vol. 7, no. 12, p. 484, 2023. DOI: 10.3390/jcs7120484.

[7] Movahedi-Rad, A. V., Keller, T., and Vassilopoulos, A. P., "Interrupted Tension-Tension Fatigue Behavior of Angle-Ply GFRP Composite Laminates," *International Journal of Fatigue*, vol. 113, pp. 377–388, 2018. DOI: 10.1016/j.ijfatigue.2018.05.001.

[8] Movahedi-Rad, A. V., Keller, T., and Vassilopoulos, A. P., "Modeling of fatigue behavior based on interaction between time- and cyclic-dependent mechanical properties," *Composites Part A: Applied Science and Manufacturing*, vol. 124, p. 105 469, 2019. DOI: 10.1016/j.compositesa.2019.05.037.

[9] Panin, S. V., Bogdanov, A. A., Eremin, A. V., Buslovich, D. G., and Alexenko, V. O., "Estimating Low- and High-Cyclic Fatigue of Polyimide-CF-PTFE Composite through Variation of Mechanical Hysteresis Loops," *Materials*, vol. 15, no. 13, p. 4656, 2022. DOI: 10.3390/ma15134656.

[10] Movahedi-Rad, A. V., Liu, L., and Keller, T., "A Novel Fatigue Life Prediction Methodology Based on Energy Dissipation in Viscoelastic Materials, Synergistic Effects of Stress Level, Stress Ratio, and Temperature," *International Journal of Fatigue*, vol. 184, p. 108 296, Jul. 2024. DOI: 10.1016/j.ijfatigue.2024.108296.

[11] Movahedi-Rad, A. V., Eslami, G., and Keller, T., "A Novel Fatigue Life Prediction Methodology Based on Energy Dissipation in Viscoelastic Materials," *International Journal of Fatigue*, vol. 152, p. 106 457, Nov. 2021. DOI: 10.1016/j.ijfatigue.2021.106457.

[12] El Kadi, H. and Ellyin, F., "Effect of Stress Ratio on The Fatigue of Unidirectional Glass Fibre/Epoxy Composite Laminates," *Composites*, vol. 25, no. 10, pp. 917–924, Nov. 1994. DOI: 10.1016/0010-4361(94)90107-4.

[13] Ellyin, F. and El-Kadi, H., "A Fatigue Failure Criterion for Fiber Reinforced Composite Laminates," *Composite Structures*, vol. 15, no. 1, pp. 61–74, Jan. 1990. DOI: 10.1016/0263-8223(90)90081-0.

[14] Ellyin, F. and Golos, K., "Multiaxial Fatigue Damage Criterion," *Journal of Engineering Materials and Technology*, vol. 110, no. 1, pp. 63–69, 1988. DOI: 10.1115/1.3226375.

[15] Mandegarian, S. and Taheri-Behrooz, F., "A General Energy Based Fatigue Failure Criterion for the Carbon Epoxy Composites," *Composite Structures*, vol. 235, p. 111 804, 2020. DOI: 10.1016/j.compstruct.2019.111804.

[16] Krieg, L. L., Personal communication, 2025.

[17] La Rosa, G. and Risitano, A., "Thermographic Methodology for Rapid Determination of The Fatigue Limit of Materials and Mechanical Components," *International Journal of Fatigue*, vol. 22, no. 1, pp. 65–73, 2000. DOI: 10.1016/S0142-1123(99)00088-2.

[18] Montesano, J., Fawaz, Z., and Bougherara, H., "Use of Infrared Thermography to Investigate the Fatigue Behavior of a Carbon Fiber Reinforced Polymer Composite," *Composite Structures*, vol. 97, pp. 76–83, Mar. 2013. DOI: 10.1016/j.compstruct.2012.09.046.

[19] Premanand, A., Renkes, M., and Balle, F., "Accelerated Estimation of the Very High Cycle Fatigue Strength and Life of Polymer Composites Under Ultrasonic Cyclic Three-Point Bending," *Materials & Design*, vol. 240, p. 112 872, 2024. DOI: 10.1016/j.matdes.2024.112872.

[20] Colombo, C. et al., "Fatigue Behavior of a GFRP Laminate by Thermography Measurements," *Procedia Engineering*, vol. 10, pp. 3518–3527, 2011. DOI: 10.1016/j.proeng.2011.04.579.

[21] Broughton, W. R. and Lodeiro, M. J., "Fatigue Testing of Composite Laminates," National Physical Laboratory, Teddington, UK, Tech. Rep. CMMT(A)252, Oct. 2000.

[22] Liang, S., Gning, P., and Guillaumat, L., "A Comparative Study of Fatigue Behaviour of Flax/Epoxy and Glass/Epoxy Composites," *Composites Science and Technology*, vol. 72, no. 5, pp. 535–543, Mar. 2012. DOI: 10.1016/j.compscitech.2012.01.011.

[23] Jamshidi, M. and Shokrieh, M. M., "On the Schapery Nonlinear Viscoelastic model: A Review," *European Journal of Mechanics - A/Solids*, vol. 108, p. 105 403, 2024. DOI: 10.1016/j.euromechsol.2024.105403.

[24] Majda, P. and Skrodzewicz, J., "A Modified Creep Model of Epoxy Adhesive at Ambient Temperature," *International Journal of Adhesion & Adhesives*, vol. 29, pp. 396–404, 2009. DOI: 10.1016/j.ijadhadh.2008.07.010.

[25] Ellyin, F. and Kujawski, D., "Tensile and fatigue behaviour of glassfibre/epoxy laminates," *Construction and Building Materials*, vol. 9, no. 6, pp. 425–430, 1995. DOI: 10.1016/0950-0618(95)00073-9.

[26] Lou, Y. C. and Schapery, R. A., "Viscoelastic Characterization of a Nonlinear Fiber-Reinforced Plastic," *Journal of Composite Materials*, vol. 5, no. 2, pp. 208–234, Apr. 1971.

[27] Jia, Y., Jiang, Z. M., Gong, X. L., and Zhang, Z., "Creep of Thermoplastic Polyurethane Reinforced with Ozone Functionalized Carbon Nanotubes," *Express Polymer Letters*, vol. 6, no. 9, pp. 750–758, 2012. DOI: 10.3144/expresspolymlett.2012.80.

[28] Reifsnider, K. L., "Fatigue Behavior of Composite Materials," *International Journal of Fracture*, vol. 16, no. 6, pp. 563–583, Dec. 1980. DOI: 10.1007/BF02265218.

[29] Vassilopoulos, A. P., "Creep/Fatigue/Relaxation of Angle-Ply GFRP Composite Laminates," in *Fatigue Life Prediction of Composites and Composite Structures*, A. P. Vassilopoulos, Ed., Cambridge, UK: Woodhead Publishing, 2010, pp. 95–131.

[30] Anton Paar. "Basics of dynamic mechanical analysis (DMA)," Accessed: Jan. 20, 2026. [Online]. Available: https://wiki.anton-paar.com/nl-en/basics-of-dynamic-mechanical-analysis-dma/.

[31] Karvanis, K. et al., "Preparation and Dynamic Mechanical Analysis of Glass or Carbon Fiber/Polymer Composites," in *IOP Conference Series: Materials Science and Engineering*, vol. 362, 2018, p. 012 005. DOI: 10.1088/1757-899X/362/1/012005.

[32] Esse, D., Scheuring, B., Henning, F., and Liebig, W. V., "Evaluation of the Time-Temperature Superposition by Comparing Neat and Glass-Fibre-Reinforced Epoxy Using Dynamic Mechanical Thermal Analysis," *Polymer Testing*, vol. 146, p. 108 747, 2025. DOI: 10.1016/j.polymertesting.2025.108747.

[33] Miyano, Y., Nakada, M., and Nishigaki, K., "Prediction of Long-Term Fatigue Life of Quasi-Isotropic CFRP Laminates for Aircraft Use," *International Journal of Fatigue*, vol. 28, no. 10, pp. 1217–1225, 2006. DOI: 10.1016/j.ijfatigue.2006.02.007.

[34] Movahedi-Rad, A. V., Keller, T., and Vassilopoulos, A. P., "Fatigue Damage in Angle-Ply GFRP Laminates under Tension-Tension Fatigue," *International Journal of Fatigue*, vol. 109, pp. 60–69, 2018. DOI: 10.1016/j.ijfatigue.2017.12.015.

[35] Movahedi-Rad, A. V., Keller, T., and Vassilopoulos, A. P., "Creep effects on tension-tension fatigue behavior of angle-ply gfrp composite laminates," *International Journal of Fatigue*, vol. 123, pp. 144–156, 2019. DOI: 10.1016/j.ijfatigue.2019.02.010.

[36] Xu, B., Hurk, B. van den, Lugger, S. J. D., Blok, R., and Teuffel, P., "Creep Analysis of the Flax Fiber-Reinforced Polymer Composites Based on the Time-Temperature Superposition Principle," *Science and Engineering of Composite Materials*, vol. 30, no. 1, p. 20 220 218, 2023. DOI: 10.1515/secm-2022-0218.

[37] Tayyebati, M., "Self-Heating and Loading Frequency in the High-Cycle Fatigue of Angle-Ply Glass/Epoxy Laminates: A Temperature-Controlled Comparison," *European Journal of Mechanics - A/Solids*, vol. 105, p. 105 423, 2026. DOI: 10.1016/j.euromechsol.2026.105423.

[38] Movahedi-Rad, A. V., Keller, T., and Vassilopoulos, A. P., "Stress Ratio Effect on Tension-Tension Fatigue Behavior of Angle-Ply GFRP Composite Laminates," *International Journal of Fatigue*, vol. 134, p. 105 475, 2020. DOI: 10.1016/j.ijfatigue.2020.105475.

[39] Movahedi-Rad, A. V., Keller, T., and Vassilopoulos, A. P., "Creep-Fatigue Interaction in Composite Materials," *Composites Part A: Applied Science and Manufacturing*, vol. 141, p. 106 206, 2021. DOI: 10.1016/j.compositesa.2020.106206.

[40] Manjunatha, C. M., "The Fatigue Behaviour of a Glass Fibre-Epoxy Composite with Hybrid-Toughened Matrix," Ph.D. dissertation, Imperial College London, South Kensington Campus, London, UK, 2010.

[41] Sartorio, S., Personal communication, 2026.

[42] Truesdell, C. and Noll, W., "The Non-Linear Field Theories of Mechanics," in *Handbuch der Physik*, S. Flügge, Ed., vol. III/3, Berlin, Heidelberg, New York: Springer-Verlag, 1965, pp. 1–579. DOI: 10.1007/978-3-642-46015-9_1.

[43] Grasse Zur Ingenieurgesellschaft mbH. "Fatigue test according to ASTM D3479," Accessed: Aug. 14, 2026. [Online]. Available: https://grassezur.de/en/material-testing/service-strength/fatigue-test-astm-d3479.

[44] Hermansen, S. M. and Lund, E., "Multi-Material and Thickness Optimization of Laminated Composite Structures Subject to High-Cycle Fatigue," *Structural and Multidisciplinary Optimization*, vol. 66, no. 259, 2023. DOI: 10.1007/s00158-023-03708-4.

[45] *Standard Test Method for In-Plane Shear Response of Polymer Matrix Composite Materials by Tensile Test of a* ±45° *Laminate*, ASTM International, 2013.

[46] Paris, F., Wisnom, M. R., and Swolfs, Y. "How do we measure shear strength of composites and the factors affecting it?" KU Leuven, Accessed: Aug. 15, 2026. [Online]. Available: https://www.mtm.kuleuven.be/english/pdf/paper-shear-strength.

[47] Sartorio, S. and Carvalho, J., Personal communication regarding the applicability of Double Euler specimen geometry, 2026.

[48] Feng, Z., Ma, Q., Ma, H., An, Z., and Bai, Z., "A Common Model for Stiffness Degradation of Composites at Material and Product Levels," *Journal of Failure Analysis and Prevention*, vol. 23, pp. 1550–1557, 2023. DOI: 10.1007/s11668-023-01692-x.

[49] Perreux, D. and Joseph, E., "The Effect of Frequency on the Fatigue Performance of Filament-Wound Pipes Under Biaxial Loading: Experimental Results and Damage Model," *Composites Science and Technology*, vol. 57, no. 3, pp. 353–364, Jan. 1997. DOI: 10.1016/S0266-3538(96)00155-8.

[50] Hülsbusch, D., Kohl, A., Striemann, P., Niedermeier, M., Strauch, J., and Walther, F., "Development of an Energy-Based Approach for Optimized Frequency Selection for Fatigue Testing on Polymers: Exemplified on Polyamide 6," *Polymer Testing*, vol. 81, p. 106 260, 2020. DOI: 10.1016/j.polymertesting.2019.106260.

[51] ScienceDirect Topics. "Mechanical fatigue test," Accessed: Feb. 6, 2026. [Online]. Available: https://www.sciencedirect.com/topics/engineering/mechanical-fatigue-test.

[52] Diën, C. van, *Manual for Fatigue Testing with MTS Machines*, Delft Aerospace Structures and Materials Laboratory, Mar. 2021.

[53] Jerina, K. L., Schapery, R. A., Tung, R. W., and Sanders, B. A., "Viscoelastic Characterization of a Random Fiber Composite Material Employing Micromechanics," in *Short Fiber Reinforced Composite Materials*, ser. ASTM Special Technical Publication, B. A. Sanders, Ed., vol. 772, Philadelphia, PA: ASTM, 1982, pp. 225–250.

[54] Serna Moreno, M. C. and Horta Muñoz, S., "Pseudo-Ductile Effects in ±45° Angle-Ply CFRP Laminates Under Uniaxial Loading: Compression and Cyclic Tensile Test," *Composites Part B: Engineering*, vol. 233, p. 109 631, 2022. DOI: 10.1016/j.compositesb.2022.109631.

[55] Schapery, R. A., "Nonlinear Viscoelastic and Viscoplastic Constitutive Equations with Growing Damage," *International Journal of Fracture*, vol. 97, pp. 33–66, 1999.

[56] Zhang, S. Y. and Xiang, X. Y., "Creep Characterization of a Fiber Reinforced Plastic Material," *Journal of Reinforced Plastics and Composites*, vol. 11, pp. 1187–1194, 1992.

[57] Nouali, M., Dony, A., and Carter, A., "Evaluation of Fatigue Life of Asphalt Binders Using the Time Sweep and Linear Amplitude Sweep Tests: A Literature Review," *Journal of Traffic and Transportation Engineering (English Edition)*, vol. 11, no. 6, pp. 1210–1242, 2024.

A MTS MPT Programming Sequences

This appendix presents the MTS Multi-Purpose Testware (MPT) frequency programmes used during selected constant-amplitude fatigue tests. The programmed frequencies were obtained from the predicted evolution of the dynamic modulus and the corresponding frequency required to maintain the prescribed target strain rate. For each test condition, the implemented MPT programme is presented alongside its corresponding predicted modulus and frequency profile.

A.1. Programming Sequences for $R = 0.1$

A.1.1. 50% UTS, $R = 0.1$

Table A.1: *MTS MPT programming sequence for 50% UTS at* $R = 0.1$.

Block	Cycles	f (Hz)	Cum.
1	100	1.809	100
2	200	1.741	300
3	300	1.725	600
4	500	1.745	1100
5	1000	1.763	2100
6	2000	1.731	4100
7	5000	1.681	9100
8	5000	1.650	14100
9	50000	1.627	64100
10	10000	1.630	74100
11	50000	1.628	124100
12	51464	1.580	175564

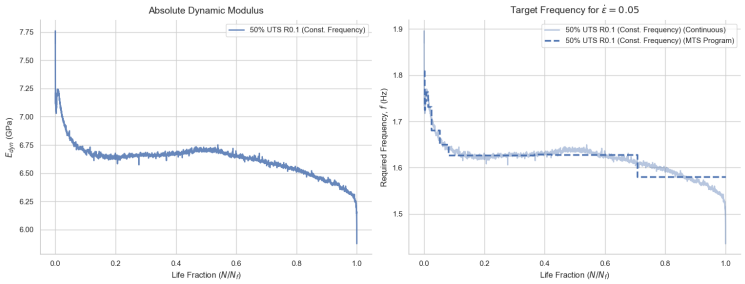


Figure A.1: *Dynamic modulus evolution and corresponding continuous and MPT-programmed target frequency for 50% UTS at* $R = 0.1$.

A.1.2. 60% UTS, $R = 0.1$

Table A.2: *MTS MPT programming sequence for 60% UTS at* $R = 0.1$.

Block	Cycles	f (Hz)	Cum.
1	100	1.216	100
2	200	1.222	300
3	300	1.196	600
4	500	1.181	1100
5	500	1.169	1600
6	620	1.142	2220

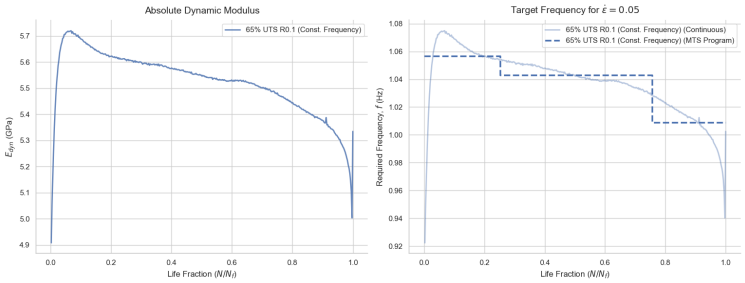


Figure A.2: *Predicted dynamic modulus evolution and corresponding continuous and MPT-programmed target frequency for 60% UTS at* $R = 0.1$.

A.1.3. 62% UTS, $R = 0.1$

Table A.3: *MTS MPT programming sequence for 62% UTS at* $R = 0.1$.

Block	Cycles	f (Hz)	Cum.
1	100	1.157	100
2	200	1.152	300
3	300	1.142	600
4	500	1.127	1100
5	213	1.091	1313

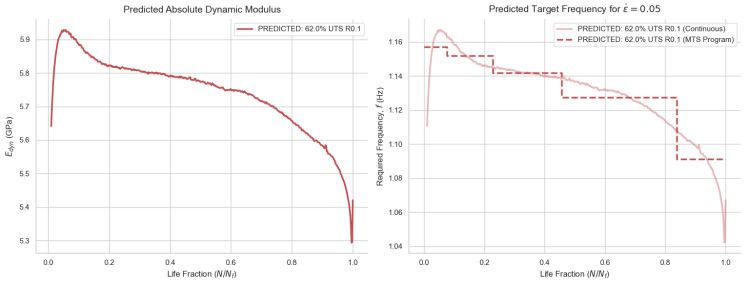


Figure A.3: *Predicted dynamic modulus evolution and corresponding continuous and MPT-programmed target frequency for 62% UTS at* $R = 0.1$.

A.1.4. 65% UTS, $R = 0.1$

Table A.4: *MTS MPT programming sequence for 65% UTS at $R = 0.1$.*

Block	Cycles	f (Hz)	Cum.
1	100	1.057	100
2	200	1.043	300
3	97	1.009	397

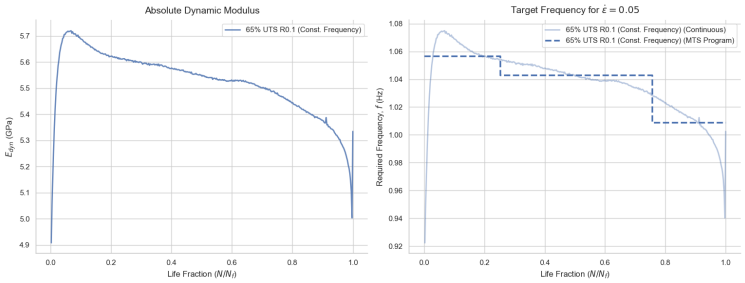


Figure A.4: *Dynamic modulus evolution and corresponding continuous and MPT-programmed target frequency for 65% UTS at $R = 0.1$.*

A.2. Programming Sequences for $R = 0.3$

A.2.1. 60% UTS, $R = 0.3$

Table A.5: *MTS MPT programming sequence for 60% UTS at $R = 0.3$.*

Block	Cycles	f (Hz)	Cum.
1	100	1.848	100
2	200	1.848	300
3	300	1.878	600
4	500	1.940	1100
5	500	1.992	1600
6	1000	2.032	2600
7	5000	2.083	7600
8	5000	2.100	12600
9	5000	2.104	17600
10	5000	2.096	22600
11	4135	2.071	26735

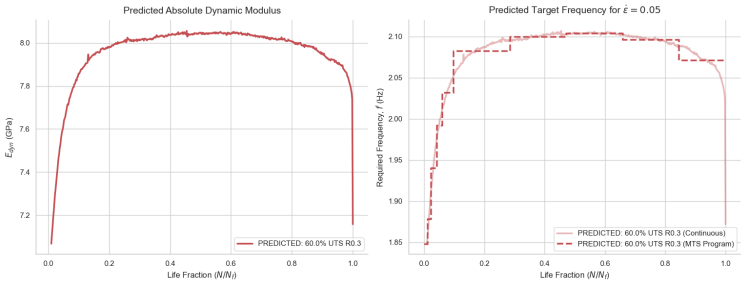


Figure A.5: *Predicted dynamic modulus evolution and corresponding continuous and MPT-programmed target frequency for 60% UTS at $R = 0.3$.*

A.2.2. 65% UTS, $R = 0.3$

Table A.6: *MTS MPT programming sequence for 65% UTS at $R = 0.3$.*

Block	Cycles	f (Hz)	Cum.
1	100	1.590	100
2	200	1.677	300
3	300	1.727	600
4	500	1.783	1100
5	1000	1.843	2100
6	2000	1.891	4100
7	5000	1.919	9100
8	5000	1.929	14100
9	5000	1.929	19100
10	5000	1.919	24100
11	2635	1.893	26735

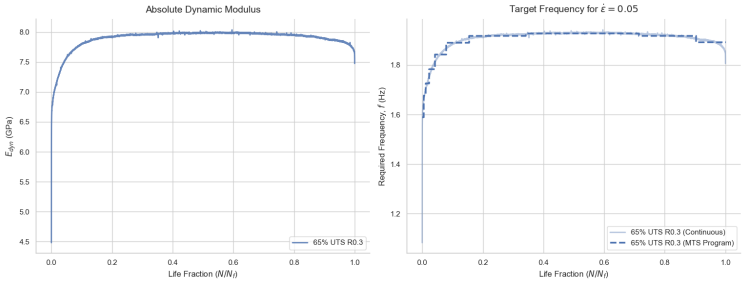


Figure A.6: *Dynamic modulus evolution and corresponding continuous and MPT-programmed target frequency for 65% UTS at $R = 0.3$.*

A.2.3. 70% UTS, $R = 0.3$

Table A.7: *MTS MPT programming sequence for 70% UTS at* $R = 0.3$.

Block	Cycles	f (Hz)	Cum.
1	100	1.364	100
2	200	1.512	300
3	300	1.624	600
4	500	1.677	1100
5	1000	1.705	2100
6	2000	1.717	4100
7	342	1.695	4442

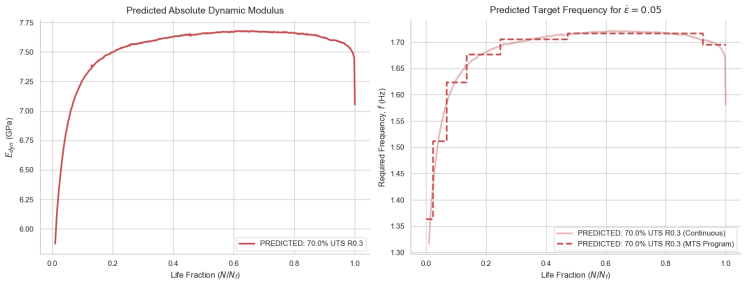


Figure A.7: *Predicted dynamic modulus evolution and corresponding continuous and MPT-programmed target frequency for 70% UTS at* $R = 0.3$.

B Recommended Procedure for Applying and Extending the Proposed Framework

Further research on the proposed fatigue-life prediction framework should initially focus on validation rather than immediate reformulation. The framework developed in this thesis has been assessed using a limited experimental dataset and therefore its applicability to other material systems, laminate configurations and loading conditions remains to be established. Nevertheless, it is hypothesised that the overall structure of the framework may remain applicable to a broad range of composite configurations, potentially even without the nonlinear augmentation introduced in this work where the material response is sufficiently close to the assumptions underlying Krieg's original formulation.

For a new material configuration, the first objective should therefore be to determine whether the existing framework can reproduce the observed behaviour with only re-identified material parameters. Where this is unsuccessful, the discrepancy should be used to identify which component of the framework requires modification. This may range from redefining the augmentation parameter for a particular material system, fibre orientation or stress state, to revisiting more fundamental assumptions within Krieg's framework. Identifying the material and loading configurations that lead to substantial violations of the framework's underlying assumptions is itself an important research gap.

The stress-sweep testing methodology should be treated similarly. In particular, the application of Miner's rule provides a practical means of deriving an approximate S-N slope from an accelerated test, but its physical validity within this context requires further investigation. It is therefore recommended that the SST-based procedure is initially regarded as a practical engineering approximation, analogous to the conventional use of Miner's rule, rather than as a fundamental description of fatigue damage accumulation. Future studies should consequently place particular emphasis on validating the resulting S-N slope across different stress ratios and material systems.

The following procedure is proposed as guidance for researchers wishing to apply and/or extend the fatigue-life prediction framework developed in this thesis.

Define New Case

The first step is to define the material configuration and loading conditions of interest. Relevant variables may include the matrix type, reinforcement material, fibre orientation, laminate architecture, stress ratio, temperature, environmental condition and intended loading regime. For example, a new study may consider a thermoplastic matrix, carbon-fibre reinforcement, a different fibre orientation or negative stress ratios. An initial judgement should then be made as to whether the resulting response is expected to remain predominantly matrix-dominated or fibre-dominated. This provides an indication of whether the nonlinear viscoelastic extension introduced in this thesis is likely to remain relevant.

As a general starting point, it is recommended that the same framework developed in this thesis is first applied with the appropriate material parameters re-identified. This allows departures from the current assumptions to be identified systematically rather than introducing additional model complexity a priori. Where a particular limitation can already be anticipated from the physics of the new case, however, a corresponding modification may be introduced before testing.

One notable example concerns negative stress ratios. The present work-done correction was developed for the investigated positive R-ratio conditions. For $R < 0$, the definition of the applied-to-reference work ratio, $\frac{W_a}{W_{\text{ref}}}$, should first be revisited so that the contribution of the compressive portion of the hysteresis loop is appropriately represented. Once this definition has been established, the remainder of the framework can be applied unchanged as an initial working hypothesis, after which any discrepancies with the experimental response can be used to identify which aspects of the framework require further modification.

Step 1: Specimen Design and Finite Element Verification

The specimen geometry should first be selected based on the manufacturing and testing capabilities. Regardless of whether the specimen geometry developed in this thesis is retained, an FE analysis should be performed using the mechanical properties and fibre architecture of the new material configuration. The principal objective is to confirm that failure is expected to occur within the gauge section and that the corresponding stress distribution is sufficiently uniform and representative of the intended loading condition.

Changes in fibre stiffness, laminate orientation or matrix properties may substantially alter the stress redistribution compared with the present E-glass/epoxy configuration.

Step 2: Selection of the Target Strain Rate

A target strain rate should then be selected and, where possible, maintained consistently across the relevant experimental campaigns. The strain rate should be selected by considering the trade-off between three principal constraints; creep effects, self-heating and machine operability. Particular attention should also be given to how the loading parameter is controlled. For a material with a substantially different initial stiffness, the imposed displacement rate required to achieve a desired initial strain rate will change. Conversely, if maintaining a constant strain rate during stiffness degradation is considered more important than matching the initial strain rate, an alternative control strategy may be required. The researcher should therefore explicitly determine whether the priority is to control the initial strain rate, its evolution throughout fatigue life, or both.

Step 3: Specimen Manufacturing and C-scanning.

Following specimen design, the material should be manufactured and inspected using an appropriate non-destructive technique such as C-scan. The location and extent of manufacturing imperfections should be documented for each specimen where possible.

This is particularly important for the monotonic tests performed at fatigue-equivalent loading rates, for which considerable scatter in UTS was observed in the present study. Comparing the resulting strength with the corresponding C-scan may provide useful information regarding whether this variability originates from manufacturing defects rather than from the loading procedure itself. Where the C-scan is performed on the complete laminate prior to specimen extraction, the position of each final specimen should therefore be traceable to its original location.

A suggested minimum experimental programme is summarised below.

Table B.1: *Suggested minimum number of specimens for the proposed experimental programme.*

Test	Suggested minimum
Monotonic tensile — quasi-static	At least 2 specimens
Monotonic tensile — fatigue-equivalent rate	At least 3 specimens
Conventional creep/recovery [26]	At least 2 specimens
Modified creep/recovery [56]	At least 1 fresh specimen per stress level
DMA frequency dependence	At least 1 frequency-sweep specimen
DMA equivalent R-ratio investigation	Approximately 1 specimen per equivalent R-ratio
SST	At least 1 specimen per R-ratio
Fatigue — input R_1	Approximately 7 or more stress levels/data points
Fatigue — validation R_2	At least 2 stress levels per R-ratio

For conventional creep/recovery characterisation based on Schapery's original conditioning procedure, at least two specimens are recommended so that repeatability can be assessed and the experimental campaign is not dependent on a single successful specimen. If the modified Schapery procedure is adopted [56], where fresh specimens are used at individual stress levels without the preceding mechanical conditioning sequence, at least one specimen should be tested for each stress level of interest. This approach may be particularly relevant where viscoplastic deformation or irreversible damage is to be incorporated explicitly into the nonlinear augmentation.

DMA specimens are comparatively small relative to the fatigue specimens. It is recommended that a preliminary frequency sweep is first performed to identify an appropriate test frequency, and also judge its frequency sensitivity. Once selected, additional specimens may be tested at representative equivalent R-ratios while maintaining this constant frequency. This would allow the dependence of the pristine loss factor on the loading condition to be investigated more systematically.

For fatigue testing, the required number of specimens depends strongly on the research objective. If the principal objective is to validate the transfer of the augmentation parameter between stress ratios, a relatively well-populated S-N curve should first be established at the reference stress ratio R_1, with approximately seven or more stress levels/data points. Predictions at additional R_2 values may then initially be assessed using at least two stress levels, preferably representing relatively high- and low-life regions. If the principal objective is instead to validate the SST-derived slope, a larger number of fatigue data points at each R-ratio is preferable, since two validation points may be insufficient to independently establish the experimental S-N slope.

Step 4: Recommended Experimental Sequence

The experiments should preferably be performed in an order that allows the results of earlier tests to inform the design of later experimental campaigns.The monotonic tensile tests should therefore be performed first. These provide the UTS and allow the initially assumed operating stress range used during strain-rate selection to be checked. If the measured UTS differs substantially from the preliminary estimate, the target loading rate and feasible stress range should be reassessed before continuing. The UTS can then be used to define the stress levels for the stress-sweep, creep/recovery and constant-amplitude fatigue programmes.

It is recommended that the SST is subsequently performed at an early stage. Application of the bilinear regression procedure provides an initial estimate of the fatigue-limit region. Together with the UTS, this produces a preliminary description of the S-N curve and provides an approximate range of expected fatigue lives. This information can then be used to plan the subsequent constant-amplitude fatigue validation campaign more efficiently.

A practical sequence is therefore MT → SST → DMA/CT → FT. The precise ordering of the final three activities need not be rigid. DMA and creep/recovery testing may, for example, be carried out in parallel with the fatigue programme. Furthermore, the relevance of individual characterisation methods should depend on the physical response of the material. For a strongly fibre-dominated configuration exhibiting negligible time-dependent deformation, an extensive creep/recovery campaign may provide limited additional information.

Step 5: Framework Assembly and Validation

Following completion of the experimental programme, the relevant S-N constituents should be determined using the same procedure proposed in this thesis. This includes the upper and lower anchors, S-N slope, stress-ratio correction and, where applicable, the nonlinear augmentation parameters.

Predicted fatigue lives should then be compared against an independent subset of the constant-amplitude fatigue data. The agreement should be assessed both visually and quantitatively. An error measure such as the RMSE may be used alongside the observed experimental scatter.

Recommended Routes for Framework Revision

Where validation of the original framework is unsuccessful, the required modification should be guided by the physical origin of the discrepancy rather than by the material category alone.

- **Thermoplastic or strongly viscoplastic matrices**

  If substantial permanent strain remains following recovery, the assumption that the nonlinear response can be represented entirely through recoverable viscoelasticity should be reconsidered. Two possible routes may then be followed. The first is to retain the overall structure of Krieg's framework and modify only the nonlinear augmentation. A modified Schapery formulation [56] may be used to incorporate viscoplasticity and damage into the stress-dependent augmentation parameter. Since this approach relies on characterising irreversible deformation at different stress levels, fresh specimens would be required for each stress level of interest. This route would preserve most of the existing fatigue-life framework while extending the constitutive description to account for non-recoverable deformation.

  A more fundamental alternative is to revisit the closed-loop assumption used in the derivation of the dissipated energy. In the present framework, creep-induced loop translation is neglected such that the hysteresis loop is treated as closed. For a viscoplastic material, however, progressive ratcheting may introduce an additional dissipative contribution. Conceptually, the total dissipated energy could

therefore be written as

$$TDE_{tot} = \Psi TDE_{ve} + TDE_{vp} \tag{B.1}$$

where TDE_{vp} represents the additional work associated with permanent viscoplastic deformation. A first approximation could relate this term to the mean stress and the permanent loop shift, $\varepsilon_{\mathrm{vp}}$.

If the assumption that total dissipated energy is independent of stress ratio is retained, this additional term would enter explicitly into the life-prediction equation. Unlike the purely multiplicative augmentation used in the present formulation, the viscoplastic contribution would not necessarily cancel when taking ratios between two stress ratios. Consequently, absolute viscoplastic deformation quantities would be required for each loading condition, making the resulting formulation increasingly dependent on empirical characterisation.

This would represent a shift away from the predominantly physics-based nature of the present framework toward a more phenomenological formulation. If maintaining a physics-based description is considered important, a more fundamental treatment of viscoplasticity, potentially through a micromechanical or constitutive modelling approach, would therefore be preferable. It should also be noted that the preceding argument relies on the assumption that the total dissipated energy remains approximately invariant across different stress ratios. If this assumption does not hold, an alternative route may be to represent the viscoplastic contribution in a multiplicative form, analogous to the augmentation parameter introduced in the present framework, such that stress-ratio effects remain embedded within a transferable scaling relation. If neither an additive nor multiplicative augmentation is sufficient, the formulation may need to be reconsidered at a more fundamental constitutive level. In that case, interrupted fatigue testing could be used to identify the evolution of material stiffness and viscous response with damage, for example through evolving Maxwell- or Kelvin–Voigt-type parameters. This would allow the moduli and viscosities to be re-identified at different stages of fatigue life, rather than treating the viscoelastic response as fixed throughout the test.However, the practical feasibility of such an approach, as well as the additional scientific value it would provide relative to its experimental complexity, remains uncertain.

- **Carbon-fibre composites**

  Changing from glass to carbon fibre does not necessarily require a fundamental modification of the framework. If the investigated laminate remains matrix-dominated, the underlying viscoelastic response is still governed predominantly by the polymer matrix, and the same general formulation may remain applicable. Therefore, the primary concern is instead experimental. The greater stiffness of carbon fibres may reduce the magnitude of the cyclic strain response and produce considerably narrower hysteresis loops. This can make the determination of dissipated-energy quantities increasingly challenging. It is therefore recommended that the existing framework first be applied without modification. Particular attention should then be given to whether the hysteresis quantities can be measured with sufficient accuracy. If the loops become too narrow for reliable energy determination, alternative measurement techniques, signal-processing procedures or different damage metrics may need to be considered before modifying the underlying material model.

- **Different fibre orientations**

  For a different fibre orientation, the first step should be to determine whether the laminate response remains matrix-dominated or becomes increasingly fibre-dominated. This judgement determines whether the nonlinear augmentation parameter remains physically relevant. Where the governing damage mechanism is unclear, preliminary monotonic testing combined with post-failure microscopy may provide a practical indication of whether failure is governed predominantly by matrix cracking, fibre/matrix interaction or fibre failure. This can then guide whether nonlinear viscoelastic characterisation is necessary.

  For matrix-dominated angle-ply laminates, a useful extension would be to investigate whether the augmentation parameter can be expressed using an orientation-independent effective stress measure. Schapery's octahedral stress [26] concept provides one possible route, since it attempts to relate the nonlinear matrix response to an equivalent stress state rather than directly to the externally applied laminate stress. This raises the possibility that an augmentation parameter identified for one matrix-dominated orientation, for example $\pm 45°$, could be transformed and applied to another orientation,

such as ±30°, without requiring a complete creep/recovery characterisation for every laminate angle. The underlying hypothesis would be that, if the nonlinear response originates primarily from the matrix, the augmentation law should depend more strongly on the effective matrix stress than on the nominal fibre orientation itself. Such transferability should nevertheless be treated as a hypothesis and validated using a limited number of creep/recovery or fatigue tests at the new orientation.

- **Different stress ratios, particularly R<0**

  Extension to negative stress ratios requires greater caution because the loading condition may introduce damage mechanisms that are absent under tension–tension fatigue. Under tension–compression or compression–compression loading, phenomena such as fibre kinking, local buckling, crack closure and contact between previously formed damage surfaces may contribute to the measured hysteresis response. In such cases, the enclosed loop area no longer necessarily represents only intrinsic material damping or viscoelastic dissipation, but may also contain a significant contribution from evolving damage.

  The first step should therefore be to examine the physical damage mechanisms associated with the selected negative stress ratio. Microscopy, surface observations or complementary damage-monitoring techniques may be useful in determining whether the measured hysteresis response is dominated by recoverable matrix behaviour or by damage-related mechanisms. If permanent deformation and damage become significant, a modified Schapery-type formulation incorporating viscoplasticity and damage [56] may again be relevant. The validity of the assumption that creep and fatigue contributions can be treated independently should also be reassessed.

  The broader recommendation is that negative-R cases should not initially be treated as a simple extension of the existing stress-ratio correction. Instead, the physical origin of the measured dissipation should first be established, after which the appropriate component of the framework can be modified.

Overall, the recommended procedure for applying, validating and, where necessary, revising the proposed framework for new material systems and loading conditions is summarised schematically in Figure B.1.

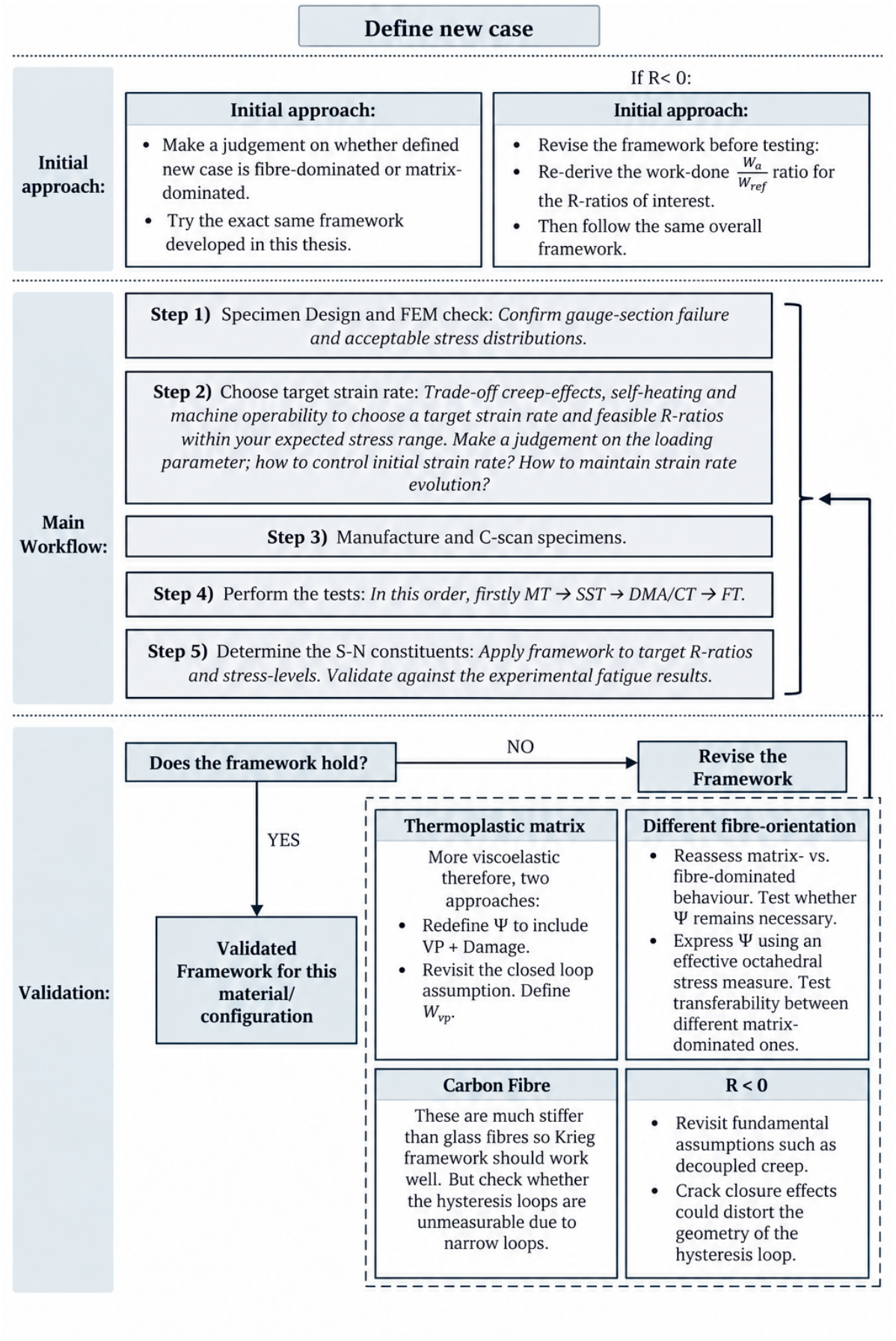


Figure B.1: *Proposed workflow for applying, validating and adapting the fatigue-life prediction framework to new material systems, fibre orientations, stress ratios and loading conditions.*